ABSTRACT

Title of Dissertation:	RESONANT AND SECULAR ORBITAL INTERACTIONS
	Ke Zhang, Doctor of Philosophy, 2007
Dissertation directed by:	Professor Douglas P. Hamilton Department of Astronomy

In stable solar systems, planets remain in nearly elliptical orbits around their stars. Over longer timescales, however, their orbital shapes and sizes change due to mutual gravitational perturbations. Orbits of satellites around a planet vary for the same reason. Because of their interactions, the orbits of planets and satellites today are different from what they were earlier. In order to determine their original orbits, which are critical constraints on formation theories, it is crucial to understand how orbits evolve over the age of the Solar System. Depending on their timescale, we classify orbital interactions as either short-term (orbital resonances) or long-term (secular evolution). My work involves examples of both interaction types.

Resonant history of the small Neptunian satellites In satellite systems, tidal migration brings satellite orbits in and out of resonances. During a resonance passage, satellite orbits change dramatically in a very short period of time. We investigate the resonant history of the six small Neptunian moons. In this unique system, the exotic orbit of the large captured Triton (with a circular, retrograde, and highly

tilted orbit) influences the resonances among the small satellites very strongly. We derive an analytical framework which can be applied to Neptune's satellites and to similar systems. Our numerical simulations explain the current orbital tilts of the small satellites as well as constrain key physical parameters of both Neptune and its moons.

Secular orbital interactions during eccentricity damping Long-term periodic changes of orbital shape and orientation occur when two or more planets orbit the same star. The variations of orbital elements are superpositions of the same number of fundamental modes as the number of planets in the system. We investigate how this effect interacts with other perturbations imposed by external disturbances, such as the tides and relativistic effects. Through analytical studies of a system consisting of two planets, we find that an external perturbation exerted on one planet affects the other indirectly. We formulate a general theory for how both orbits evolve in response to an arbitrary externally-imposed slow change in eccentricity.

RESONANT AND SECULAR ORBITAL INTERACTIONS

by

Ke Zhang

Dissertation submitted to the Faculty of the Graduate School of the
University of Maryland, College Park in partial fulfillment
of the requirements for the degree of
Doctor of Philosphy
2007

Advisory Committee:

Professor Douglas P. Hamilton, Chair
Professor Michael A'Hearn
Professor Joseph A. Burns
Professor M. Coleman Miller
Professor James A. Yorke

Napoleon: *They tell me that you have written this huge book on the system of the universe without once mentioning its Creator.*

Laplace: *I have no need for that hypothesis.*

Preface

I had hoped that I could have arranged each chapter more carefully. I had hoped that I could write a better story-telling introduction about the history of celestial dynamics. I had hoped to do many other things in this dissertation until I was at the point of running out of time. But here it is - the work I have spent seven years on.

This dissertation is organized in four parts:

Part I is an introduction. The history of the development of celestial dynamics and orbital dynamics is covered in Chapter 1. In Chapter 2, I review the basics of perturbation theory, which is the foundation of my dissertation.

Part II is on the resonant interaction and evolution of the small Neptunian satellites, in which I focus on the small inclinations of the blue planet's six small satellites and try to build a resonant history of the system based on their current orbits. Chapter 3 provides background information about the moons, as well as theoretical preparation necessary for this project. In Chapter 4, two new orbital elements are defined for resonant analysis in this system. Individual resonance passages are deciphered in Chapter 5. Finally, several physical parameters of the system are constrained based on dynamical evidence in Chapter 6.

Part III is on the secular evolution. A linear secular theory is derived to handle slow eccentricity-damping. In Chapter 7, I discuss the motivation of the project and present the standard secular theory. Eccentricity-damping is then added in Chapter 8, and secular theory is adjusted accordingly. Lastly, the theory is applied to extrasolar planetary systems in Chapter 9.

Part IV is the conclusion, which also includes possible future research directions as extensions of the two projects.

Part II and Part III are only loosely related, thus the order of reading is not important. The theoretical background in Part I, however, is helpful for the later chapters.

<div style="text-align: right">

Ke Zhang
August 1, 2007

</div>

To my parents

谨以此书献给我的父母亲

Acknowledgment

First of all, I thank my adviser, Professor Douglas P. Hamilton. Without his direction in my research, I would never have done what I did, and without his advice on life in the United States, I may not have been able to adapt to this totally different world. I also thank the whole Astronomy Department here in Maryland for their support.

I am deeply grateful to Professor Joseph A. Burns of Cornell University and Professor Richard Greenberg of the University of Arizona for valuable discussions.

I highly appreciate the careful reading of this manuscript by my thesis committee members and their helpful suggestions.

I especially thank my parents and my sister's family, who have continuously supported me all the time.

I am thankful to all my friends, who have accompanied me during the seven years of study and research, shared my happiness and sorrow, and given me immediate emotional support during my difficulties.

Finally, I thank the University of Maryland and NASA for their financial support.

Table of Contents

List of Tables

List of Figures

Part I

Introduction

Chapter 1

Celestial Mechanics and Orbital Dynamics
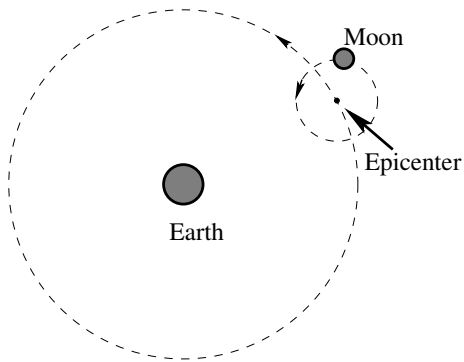
Figure 1.1: The concept of epicycles: the Moon orbits in a circle around an epicenter, which itself moves in a circle around the Earth. For complicated orbits, several epicycles may be required and the epicenters may shift.

Celestial mechanics has its origins in the curiosity that human beings display towards the mysterious motion of objects in the sky, as well as a practical need for accurately recording the passage of time and predicting the seasons. It is among the oldest fields of modern physics and astronomy, and has been substantially developed even since Sir Issac Newton (1643 - 1727) published his famous *Principia* in 1687. Before that, ancient theories about the Sun, Earth, Moon, and planets trace back to the Greek astronomers Aristarchus (310 - 230 BC), Hipparchus (190 - 120 BC), and Ptolemy (90 - 168 AD) some two millennia ago. Aristarchus was the first to propose a heliocentric model based on his estimation of a much heavier Sun than Earth. His view of the universe was opposed by most of his contemporaries and astronomers after him because the lack of parallax of the Sun, and the absence of any perceived motion of the Earth. Hipparchus, with data from hundreds of years of Babylonian observations, measured the precession of the vernal equinox at a value of $46''$ per year, close to

Most material about the early history prior to Newton is based on the 1968 version of *Encyclopaedia Britannica*.

the modern value of $50.26''$ per year. He also made an accurate measurement of the length of a year to within 7 minutes, and the distance of the Moon to within 10% error. He tried to create a model of the Moon's motion with epicycles (Fig. 1.1), but discrepancies with observations existed until the model was refined by Ptolemy. In his book, *Almagest* ($\sim$ 150 AD), Ptolemy detailed the mathematical theory about the motions of the Sun, Moon, and planets around the Earth. Although Ptolemy attributed much of his book to Hipparchus, including the original idea of epicycles, he was the first to work out the big picture of a geocentric model of the universe. As more observational data accumulated with better accuracy, more epicycles were required for the geocentric model to match observation. By Copernicus' time some 1400 years later (1473 - 1543), each planet could have as many as $40 - 60$ epicycles in order to match observations, which drove Copernicus to reconsider the heliocentric model of the universe (*De Revolutionibus Orbium Coelestium*, 1543). The heliocentric model did not gain popularity until 50 years after Copernicus' death, not only because it challenged the authority of the Church, but also because it used almost as many epicycles as Ptolemy's model did in order to precisely agree with observations. In 1609, Johannes Kepler published his famous laws on planetary orbits, which claimed that planets, including the Earth, orbit in ellipses instead of circles, with the Sun at one focus. Although requiring a single extra parameter for each orbit (eccentricity), Kepler's theory agreed with observations perfectly without the need for epicycles.

These ancient works, although accurate enough to predict the location of the known celestial bodies, utilize mathematics no more complicated than simple alge-

bra and geometry. The underlying physics responsible for celestial motions was not understood even after Kepler published his laws, which were simply empirical rules based on extremely detailed observations by Tycho Brahe and Kepler himself. Nevertheless, it was these empirical works that enabled Newton to understand the universal law of gravity and to found modern physics. Newton's contribution was a huge triumph for astronomy, physics and mathematics. His universal law of gravity is still used today to guide spacecraft flying to the outer Solar System and to model the motion of the planets to exquisite accuracy. The orbital precession of Mercury, which requires a small correction from general relativity, is the only serious shortcoming of the theory. His invention of calculus (or co-invention with Leibniz) opened the door of mathematical analysis and made modern science possible.

After Newton, theory on celestial mechanics was rapidly developed and reached its zenith with the works of two 18th century mathematicians: Joseph Louis Lagrange (1736 - 1813) and Pierre-Simon Laplace (1749 - 1827). Besides his foundational work in classical mechanics and his creation of the variational calculus, Lagrange found the "Lagrange" points (potential maxima or saddles, see Murray and Dermott, 1999) while attempting to solve the three-body problem, worked out a method to determine a comet's orbit with only three observations, and did additional important work on orbital precession and stability. Laplace, through a series of memoirs to the Academy of Science in Paris, addressed the stability of the Solar System by showing that the changes of the orbital mean motions of Jupiter and Saturn were periodic and due to their near-resonance orbits (sometimes referred as the *great inequality*). He also

spent a significant amount of time in the study of lunar motion perturbed by a non-spherical Earth, and of the oceanic tides induced by the Sun and the Moon. His most significant contribution, however, was the compilation of the five volume *Celestial Dynamics* (1799 - 1825), which "offer a complete solution of the great mechanical problem presented by the Solar System, and bring theory to coincide so closely with observation that empirical equations should no longer find a place in astronomical tables." In these books, Laplace included most of his work on planetary orbits and perturbations, as well as problems solved by earlier astronomers. Research on celestial dynamics achieved a real predictive triumph when the British astronomer Adams (1846) and the French astronomer Le Verrier (1846) independently "discovered" Neptune by analytical calculation of its perturbation on the orbit of Uranus. Galle (1846) later found the planet only 1° off Le Verrier's prediction.

The next hundred years of advances in the field were mathematical in nature, and many new studies on different kinds of perturbations to the motion of planets and satellites were conducted. Most of the analytical works during this period were focused on three-body problems (e. g., expansion of the disturbing function by Boquet, 1889), or low-order approximations for systems with a few more objects and additional perturbations (e.g., secular frequencies in the Solar System by Brouwer et al., 1950). Darwin (1879, 1880) also began to pioneer the analysis of the lower-order effects of tides and tidal friction. The use of computers for numerical integration opened a new window on the subject in the 1960s, and made it possible to handle more complicated systems for a long period of time and to study the formation and evolution of the

whole Solar System. One key numerical integration of the outer Solar System for 120,000 years was undertaken by Cohen and Hubbard (1965).

The development of numerical techniques in celestial dynamics (within the Solar System, to be specific) was recently reviewed by Morbidelli (2002), who divided the numerical study of Solar System dynamics into four major periods. During the classical period, when slow but accurate integration algorithms (Runge-Kutta and Bulirsch-Stoer methods) were used, Cohen and Hubbard (1965) verified the analytical theory about secular interactions by Brouwer et al. (1950). Sussman and Wisdom (1988) found the chaotic nature of Pluto's orbit through a 845-million-year integration on a specifically constructed parallel computer called the *Digital Orrery*. A great effort had also been given to understand resonance structure (Wisdom, 1983; Murray, 1986; Wisdom, 1987) and the distribution and stability of asteroids (Milani et al., 1989; Nesvorný and Ferraz-Mello, 1997). The symplectic period in numerical Solar System studies started with the efficient Hamiltonian-preserving algorithm proposed by Wisdom and Holman (1991). A symplectic scheme for the solution of the equations of motion for a Hamiltonian system is able to bound the energy error with a large timestep, typically 10-20 samplings per orbital period, thus enabling faster and longer integrations. With this new algorithm, research was carried out to understand the evolution and stability of the whole Solar System (Sussman and Wisdom, 1992; Murray and Holman, 1999), as well as small-body dynamics (Holman and Wisdom, 1993; Duncan et al., 1995). The most important discovery during this period is the phenomenon characterized as chaotic diffusion. In this regime, particles are stable

for billions of years, but are eventually able to escape due to long-term weak perturbations (Morbidelli, 1997; Nesvorný and Roig, 2001), overturning earlier beliefs that particles in the Solar System are either unstable in a short period of time or stable forever.

The Wisdom and Holman (1991) symplectic scheme reaches its limit when close encounters are involved, because the perturbing Hamiltonian dominates over the Keplerian potential during a close encounter, which violates one of the algorithm's fundamental assumptions. This problem was first overcome for zero-weight particles by Levison and Duncan (1994), opening the "statistics period" when systematic studies of comets and near-Earth asteroids (NEAs) was made possible. Based on statistics of the lifetime of the Jupiter-family comets and the Neptune-encounter rate of Kuiper belt objects, Levison and Duncan (1994, 1997) concluded that the Kuiper belt contains 6.7×10^9 comet-sized bodies. Duncan and Levison (1997) showed further that the Kuiper belt's scattered disk was 100 times more populated at the beginning of the Solar System. With similar techniques, Morbidelli and Gladman (1998) and Michel et al. (2000) studied the distribution of NEAs from different sources, the results of which were later used by Bottke et al. (2000, 2002) to construct a model for orbital and magnitude distribution of NEAs.

Finally, integrations of planetary accretion involving encounters and collisions among massive planetary bodies and planetesimals was enabled with the design of two algorithms: Symba (Duncan et al., 1998) and Mercury (Chambers, 1999). For the first time, the formation and evolution of the Solar System could be studied over its

entire 4.5 billion years history. For the inner Solar System, Chambers and Wetherill (1998, 2001) and Agnor et al. (1999) studied the formation of terrestrial planets from lunar-mass "planetary embryos", and found that Earth-sized planets can be formed between $0.5 - 2.0$ AU in several hundred million years, but that original embryos in the asteroid belt are mostly scattered into unstable orbits and only 1% of the population is left behind in the main belt (Petit et al., 2001). Progress was also made on the formation and evolution of the giant planets. It was known (Fernandez and Ip, 1984) that interactions with planetesimals cause giant planet to migrate: Jupiter goes inwards, while all the other three giant planets move outwards. This procedure produces certain observed structures in the Kuiper belt (Malhotra, 1993, 1995) and is responsible for Pluto's strange orbit. Recent development of the "Nice model" suggested that the four giant planets may have formed in a much tighter group: between 5.5 and 14 AU. This model was the first one to simultaneously reproduce the current orbits of the giant planet (Tsiganis et al., 2005), the Trojan population of Jupiter (Morbidelli et al., 2005) and Neptune (Sheppard and Trujillo, 2006), the source for the Late Heavy Bombardment of the terrestrial planets (Gomes et al., 2005), and the structure of the Kuiper belt (Morbidelli et al., 2007).

Our analytical understanding of the physics of orbital interactions and evolution also saw many advances during the computer era, with symbolic algebra and semi-numerical techniques in many cases. Mean-motion resonances (Section 2.3) are by far the most popular subject. Early reviews on satellite orbital resonances were given by Greenberg (1977) and Peale (1986), who also analyzed resonant encounters dur-

ing tidal migration. Two basic types of behavior of the orbital elements during an encounter were identified: kicks and trapping. Henrard (1982) and Borderies and Goldreich (1984) computed the capture probabilities during a resonant encounter. More recently, Hamilton (1994) revisited the resonant encounter problem, comparing mean-motion resonances arising from gravitational and electromagnetic perturbations. The analysis of the more subtle secondary resonances was first done by Malhotra (1990), and the effect may be responsible for breaking resonant trapping in many cases. Tidal effects in the Solar System were also investigated in great detail by Goldreich (1963) and Goldreich and Soter (1966). A review by Burns (1986) covers most development on how tides affect orbits. For non-resonant, or secular, evolution (long-term orbital interactions), once the secular frequencies of the Solar System were found (see, e.g., Brouwer et al., 1950), research has focused on the effects of secular resonances (Ward et al., 1976) on asteroids (Froeschle and Scholl, 1987; Scholl and Froeschle, 1990), on Kuiper belt objects (Nagasawa and Ida, 2000), and on other minor bodies in the Solar System including Trojan asteroids (Marzari and Scholl, 2000).

The study of planetary rings makes another important branch of the Solar System dynamics. It has a long history that dates back to 1610 when Galileo first pointed his telescope toward Saturn. His discovery was later interpreted by the Dutch astronomer Christiaan Huygens as "a thin, flat ring, nowhere touching, and inclined to the ecliptic". In many regards, Saturn's ring is the most splendid phenomenon in the Solar System, and remained the only known ring system until the 1970s and 1980s when a flurry of ground-based observations and space missions found new ring sys-

tems around Uranus (Elliot et al., 1977), Jupiter (Owen et al., 1979), and Neptune (Smith et al., 1989). Rings around Mars were first suggested by Soter (1971) and their properties were predicted by Hamilton (1996) and others. Ring dynamics experienced renewed interest with the discovery of a wide variety of rings around the giant planets. Saturn's F-ring and the Uranian rings are narrow with sharp edges, unlike the broad main rings of Saturn. Jupiter's entire ring system is composed of micronsized dust, and there are additional examples of dusty rings belonging to each of the other giant planets. A review by Cuzzi et al. (1984) showed that various features in the broad main ring of Saturn result from gravitational interactions between ring particles and embedded moonlets and among the ring particles themselves. Burns et al. (1984) reviewed the effects of electromagnetic perturbations with a focus on the vertical structure of the Jovian rings. A follow-up by Hamilton (1994) provided more details on how planetary magnetic fields interact with micron-sized ring particles. Showalter and Burns (1982) showed numerically that sharp ring edges could be confined and wakes and spokes inside the narrow rings might be excited by nearby shepherd moons. Since 2004, the *Cassini* spacecraft has sent back the most detailed data on the Saturnian rings, which confirms some earlier theories about ring-moon interactions, and also shows a number of interesting new features. This has led to active and ongoing numerical and analytical exploration of ring dynamics. Several recent books (*Planetary Rings* by Esposito (2006), *Planetary Ring Systems* by Miner et al. (2007)) and articles (e.g. Porco and Hamilton, 2007), cover both observational and theoretical developments in planetary ring systems.

Research on orbital dynamics is not limited to the Solar System. With the discoveries of dusty disks (Aumann, 1985) and extrasolar planets (Wolszczan and Frail, 1992; Mayor and Queloz, 1995), a lot of effort has been spent in understanding the different orbital statistics of planets (the Extrasolar Planet Encyclopaedia, *http://exoplanet.eu/*) and planet-disk interactions (Ward, 1988). The most significant difference between the orbits of extrasolar planets and planets in the Solar System is that the former usually have much larger eccentricities. Several mechanisms were proposed to produce these eccentric orbits, including Kozai resonances (Holman et al., 1997), planet-planet scattering (Ford et al., 2001), planet-disk interaction (Goldreich and Sari, 2003), and stellar encounters (Zakamska and Tremaine, 2004). In Part III of this dissertation, we will study how very close giant planets ("hot-Jupiters") may retain their eccentricities against tidal circularization. Studies in planet-disk interactions are usually orientated towards understanding the features seen in the spatially-resolved disks (Holland et al., 1998; Wilner et al., 2002; Greaves et al., 2005), and towards predicting possible planetary masses and orbits based on these disk patterns (Kuchner and Holman, 2003).

Chapter 2

Perturbation Theory

Gravity from a massive central body usually determines planetary and satellite systems, resulting in elliptical orbits with the dominate mass at one focus, as stated by Kepler's first law. The largest planet in the Solar System, Jupiter, is a thousand times less massive than the Sun, and the most extreme satellite-planet mass ratio, excluding Pluto-Charon, is about 1% for the Moon-Earth pair. Thus, any effects from forces other than central gravity can be treated as small perturbations to the otherwise Keplerian orbits. In this chapter, we summarize the basics of perturbation theory, with emphasis on results relevant to the later chapters.

2.1   Definition of Orbits

In a system of two perfect spherical bodies (ideal planets, stars, satellites, etc.), the orbit of each object is an ellipse with their common center of mass at one focus, as is determined by the Keplerian potential. In the case of a hierarchical star-planet or planet-satellite system, the orbit of the secondary body is usually measured in a body-centric frame with the dominant mass at the center, and is also a closed ellipse. We will call the dominant mass a planet (m_p) and the secondary mass a satellite (m_s) throughout this chapter.
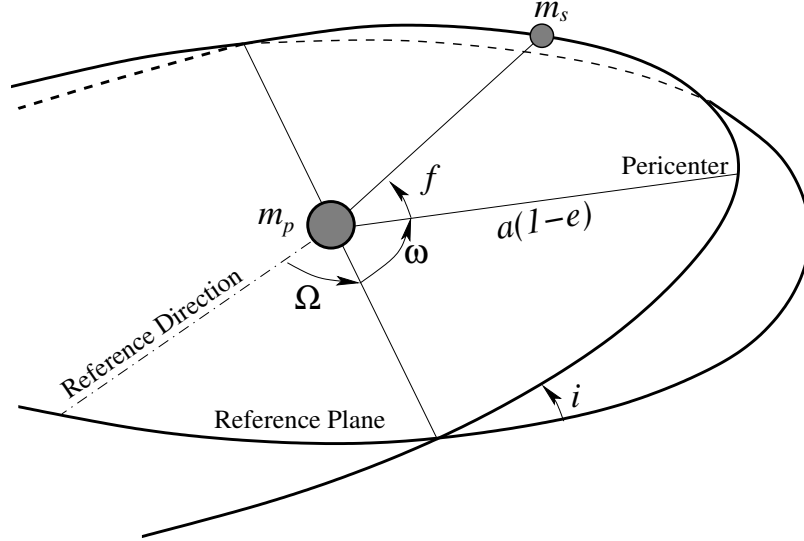
Figure 2.1: Definition of orbital elements. A Keplerian orbit is a closed ellipse with the dominate mass at one focus. The location of the secondary in space can be determined by 6 orbital elements: the semi-major axis a, eccentricity e, inclination i, longitude of ascending node Ω, argument of pericenter ω, and true longitude f. The longitude of pericenter $\varpi = \Omega + \omega$ is a bent angle measured in two different planes.

The elliptical orbit of a satellite is well-defined geometrically by five constant Keplerian orbital elements (Fig. 2.1): the semi-major axis a, the eccentricity e, the inclination i, the longitude of ascending node Ω, and the argument of pericenter ω. The last one is often replaced by the longitude of pericenter $\varpi = \Omega + \omega$, which is a bent angle measured partly in the reference plane and partly in the orbital plane. The semi-major axis a is sometimes replaced by orbital mean motion n, which is the average angular velocity of the satellite:

$$n = \sqrt{\frac{G(m_p + m_s)}{a^3}},$$

where G is the gravitational constant. To determine the location of the satellite in space, a sixth element is required to describe its position along the orbit. This element takes many forms; for example, the true anomaly f is the angle between the

13

directions from the central star to the planet and its orbital pericenter (Fig. 2.1). A more commonly used angle, although without a simple geometric representation, is the mean longitude λ, which is a longitude measured in two planes from the reference direction, much like ϖ. It has the important property of increasing linearly in time. In contrast to the other five elements, the true anomaly or mean longitude changes periodically over time to represent a dynamical system instead of a static one.

With two or more satellites in the system, or if the shapes of the objects deviate from perfect spheres, satellite orbits are not closed eclipses any longer. In the most common cases, the additional forces are much weaker than the Keplerian potential and the orbits differ only slightly from perfect eclipses. For each instant in time, an imaginary orbit for each satellite can still be defined by the so-called osculating elements transformed from its location and velocity vectors, assuming a Keplerian orbit (Murray and Dermott, 1999, §2.9). As a result of the extra perturbations, the first five osculating elements (a, e, I, Ω, and ϖ) vary only slowly with time, while the true anomaly f (and similarly the mean longitude λ) still change quickly. In some aspects of our work, we will average the orbits over f to study the long-term evolution of the orbital size, shape, and orientation.

2.2   Disturbing Function

If a system contains more than one satellite (Fig. 2.2), the orbits can behave in a rather complicated manner because of mutual perturbations between the two objects, as we pointed out in last section. It is not difficult to write down the equations of

motion of the satellites based only on Newton's laws:

$$\ddot{\mathbf{r}}_1 = -G(m_p + m_1)\frac{\mathbf{r}_1}{r_1^3} - Gm_2\left(\frac{\mathbf{r}_1 - \mathbf{r}_2}{|\mathbf{r}_1 - \mathbf{r}_2|^3} + \frac{\mathbf{r}_2}{r_2^3}\right) = \nabla_{\mathbf{r}_1}\mathcal{K}_1 + \nabla_{\mathbf{r}_1}\mathcal{R}_1, \qquad (2.1)$$

$$\ddot{\mathbf{r}}_2 = -G(m_p + m_2)\frac{\mathbf{r}_2}{r_2^3} - Gm_1\left(\frac{\mathbf{r}_2 - \mathbf{r}_1}{|\mathbf{r}_1 - \mathbf{r}_2|^3} + \frac{\mathbf{r}_1}{r_1^3}\right) = \nabla_{\mathbf{r}_2}\mathcal{K}_2 + \nabla_{\mathbf{r}_2}\mathcal{R}_2. \qquad (2.2)$$

Here $\mathbf{r}_1$ and $\mathbf{r}_2$ are the position vectors of the inner satellite m_1 and the outer satellite m_2, respectively, and $\mathcal{K}_1$ and $\mathcal{K}_2$ are the Keplerian potentials due to the central planet, which alone would cause each satellite to orbit in an ellipse. The two additional potentials, $\mathcal{R}_1$ and $\mathcal{R}_2$, are the disturbing functions arising from the satellites' perturbation on each other; they can be written explicitly as

$$\mathcal{R}_1 = Gm_2\left(\frac{1}{|\mathbf{r}_1 - \mathbf{r}_2|} - \frac{\mathbf{r_1} \cdot \mathbf{r_2}}{r_2^3}\right), \qquad (2.3)$$

$$\mathcal{R}_2 = Gm_1\left(\frac{1}{|\mathbf{r}_1 - \mathbf{r}_2|} - \frac{\mathbf{r_1} \cdot \mathbf{r_2}}{r_1^3}\right). \qquad (2.4)$$
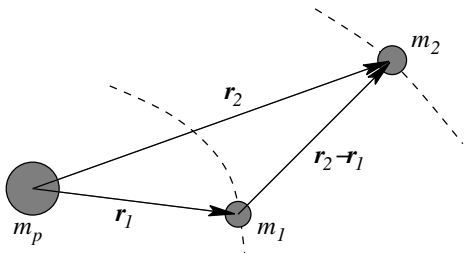
Figure 2.2: A two-satellite system. Position vectors are measured in the planet-centric frame. By convention, the inner satellite has subscript "1", and the outer one has subscript "2".

Despite the concise look of Eqs. (2.1-2.4), it is conceptually simpler to consider the evolution of orbits in terms of orbital elements rather than the more rapidly-varying position and velocity vectors. A significant effort has been devoted toward this end, starting with Peirce (1849) who derived a series expansion of Eqs. (2.3) and (2.4) to sixth order in the eccentricities and mutual inclination. Le Verrier (1855) published the most commonly-used expansion to seventh-order, which was later expanded to eighth order by Boquet (1889). All these expansions are carried out in terms of the mutual inclination and ascending node, which

15

simplifies the calculation and is useful for many situations. When strong perturbations from rotational deformation of the planet (Section 2.4) or from a massive foreign object exist, however, inclinations measured from the planet's equatorial plane or the Laplace plane (Chapter 4) are more useful. Thus an expansion in individual orbital inclinations is necessary. Such an expansion to fourth order can be found in the appendix of Murray and Dermott (1999), and Murray and Harper (1993) have performed an error-free eighth-order expansion relying extensively on two independent computer algebra codes.

Once we have written a disturbing function in terms of orbital elements, we can determine the effect of the corresponding perturbation on the orbit by solving Lagrange's planetary equations:

$$\frac{d\epsilon}{dt} = -\frac{2}{na}\frac{\partial\mathcal{R}}{\partial a} + \frac{\sqrt{1-e^2}(1-\sqrt{1-e^2})}{na^2 e}\frac{\partial\mathcal{R}}{\partial e} + \frac{\tan(i/2)}{na^2\sqrt{1-e^2}}\frac{\partial\mathcal{R}}{\partial i}, \qquad (2.5)$$

$$\frac{da}{dt} = \frac{2}{na}\frac{\partial\mathcal{R}}{\partial\epsilon}, \qquad (2.6)$$

$$\frac{de}{dt} = -\frac{\sqrt{1-e^2}}{na^2 e}\left[(1-\sqrt{1-e^2})\frac{\partial\mathcal{R}}{\partial\epsilon} + \frac{\partial\mathcal{R}}{\partial\varpi}\right], \qquad (2.7)$$

$$\frac{di}{dt} = -\frac{\tan(i/2)}{na^2\sqrt{1-e^2}}\left[\frac{\partial\mathcal{R}}{\partial\epsilon} + \frac{\partial\mathcal{R}}{\partial\varpi}\right] - \frac{1}{na^2\sqrt{1-e^2}\sin i}\frac{\partial\mathcal{R}}{\partial\Omega}. \qquad (2.8)$$

$$\frac{d\varpi}{dt} = \frac{\sqrt{1-e^2}}{na^2 e}\frac{\partial\mathcal{R}}{\partial e} + \frac{\tan(i/2)}{na^2\sqrt{1-e^2}}\frac{\partial\mathcal{R}}{\partial i}, \qquad (2.9)$$

$$\frac{d\Omega}{dt} = \frac{1}{na^2\sqrt{1-e^2}\sin i}\frac{\partial\mathcal{R}}{\partial i}. \qquad (2.10)$$

The angle $\epsilon = \lambda - nt$ is defined as the mean longitude at epoch. Brouwer and Clemence (1961) and Danby (1988) both give detailed derivations of these equations.

Disturbing functions are not limited to two-satellite systems. For a system with many satellites, each satellite raises perturbation potentials, in the form of Eqs. (2.3)

or (2.4), on all other satellites, and the disturbing function of a satellite can be calculated by summing perturbation potentials from all other satellites. In addition, any other potentials leading to additional disturbing forces can be treated in this way, as we shall see in Section 2.4.

2.3 Secular and Resonant Perturbations

After expansion in terms of small quantities e and i, a disturbing function can be written as a sum of a series of cosine harmonics:

$$\mathcal{R} = \sum_{(j_k)} R_{(j_k)} \cos(j_1 \lambda_1 + j_2 \lambda_2 + j_3 \varpi_1 + j_4 \varpi_2 + j_5 \Omega_1 + j_6 \Omega_2) \tag{2.11}$$

with the strength of each harmonic given to lowest order by

$$R_{(j_k)} = \beta(a_1, a_2) \, e_1^{|j_3|} \, e_2^{|j_4|} \, (\sin i_1)^{|j_5|} \, (\sin i_2)^{|j_6|}. \tag{2.12}$$

Here $j_1, \cdots, j_6$ are integers subject to the d'Alembert relations:

$$j_1 + j_2 + j_3 + j_4 + j_5 + j_6 = 0, \tag{2.13}$$

$$j_5 + j_6 = \text{even number}. \tag{2.14}$$

Hamilton (1994) provides an intuitive derivation of these rules based on spatial symmetry. Finally, $\beta(a_1, a_2)$ is the part of strength that is independent of orbital eccentricities and inclinations. It, however, depends on the six integers j_k in addition to the two semi-major axes. Ellis and Murray (2000) devised a method to find the strength factor for a certain argument

$$\phi = j_1 \lambda_1 + j_2 \lambda_2 + j_3 \varpi_1 + j_4 \varpi_2 + j_5 \Omega_1 + j_6 \Omega_2. \tag{2.15}$$

For orbital evolution studies, the fast changes of λ_1 and λ_2, which specify the locations of the satellites, are less important than the change in orbital size (a), shape (e), and orientation $(i, \Omega,$ and $\varpi)$. Hence, we average the disturbing function over the two orbital periods. Consequently, most terms in Eq. (2.11) average to zero with the following two exceptions:

i) Secular terms: $j_1 = j_2 = 0$; or

ii) Resonant terms: $j_1 \neq 0$ or $j_2 \neq 0$, but

$$j_1 \lambda_1 + j_2 \lambda_2 = \text{constant}. \tag{2.16}$$

Terms that meet condition (i) cause secular perturbations, which exist for any two interacting orbits. Since the strength of a perturbation term is proportional to powers of e and $\sin i$ (Eq. 2.12), for orbits with small eccentricities and inclinations, terms with large $|j_3|$, $|j_4|$, $|j_5|$, or $|j_6|$ only have weak effects. For the lowest-order terms with $(j_3 = 1, j_4 = -1)$ or $(j_5 = 1, j_6 = -1)$, the Lagrange equations can be linearized and an analytical solution can be found, leading to the first-order secular theory. Secular perturbations between planets cause periodic changes of orbital eccentricities and inclinations, as well as precessions of the ascending nodes and pericenters (Chapter 7.2). Stockwell (1873) was the first to calculate the secular variations for all eight major planets, which was later improved by Brouwer et al. (1950). Their method is similar to what we will use in Part III of this dissertation, where we study how external eccentricity damping affects secular interactions.

Terms satisfying condition (ii) lead to mean-motion resonances; taking the time

derivative of Eq. (2.16), we find

$$j_1 n_1 + j_2 n_2 = 0. \tag{2.17}$$

This condition can only be met when the two mean motions have a ratio of integers $(n_2/n_1 = -j_1/j_2)$, hence the name "mean-motion resonance". In general, a resonance happens when a dynamical system is driven at one of its natural frequencies. Here when a "commensurability" exists among the orbits (Eq. 2.17), the same orbital configuration repeats and small perturbations between the satellites can accumulate in phase. Following Greenberg (1977), we examine the resonance mechanism and stability for a simple case in which two planar orbits are in 2:1 mean-motion resonance $(j_1 = 1$ and $j_2 = -2)$. Similar analyses can also be found in Peale (1976, 1986) and Murray and Dermott (1999).

The system is shown in Fig. 2.3: for simplicity we assume that i)the inner orbit is circular, ii) the outer one is eccentric, and iii) $m_1 \gg m_2$ so that the inner orbit is not affected. The perturbation from m_1 results in a net tangential force $\mathbf{f}$ on m_2. During the period when the two move from conjunction to opposition, $\mathbf{f}$ is in the direction of motion and accelerates m_2. During the period from opposition to next conjunction, $\mathbf{f}$ is in the opposite direction of motion and decelerates m_2. If the conjunction occurs exactly at pericenter or apocenter of the outer orbit, the tangential force averages to zero, and there is no energy or angular momentum exchange. As a result, the orbital configuration does not change and the two satellites always line up at pericenter or apocenter.

Conjunctions at any other location destroy this symmetry and result in a non-zero

averaged force that adjusts the conjunction location. Fig. 2.3 shows the case in which the two satellites line up just past m_2's pericenter. When the two satellites move from conjunction to opposition, the average distance between them is larger than when they move from opposition to next conjunction since m_2 passes its apocenter in the former case. As a result, the tangential force on m_2 during the accelerating phase is weaker than during the decelerating phase. Furthermore, the system spends less time moving from conjunction to opposition (slightly less than one period of m_1) than from opposition to next conjunction (slightly longer than one period of m_1). Hence, during a full period between two successive conjunctions, the weaker accelerating force is applied for a shorter time than the stronger decelerating force, resulting in a net loss of energy and angular momentum for the outer orbit. The outer satellite falls inward and its mean motion, n_2, increases. The inner satellite then has more difficulty catching up with the outer one, so subsequent conjunctions must move towards the apocenter. Similarly, conjunctions occurring during the second half of the outer orbit, when m_2 moves from its apocenter to pericenter, also shift towards m_2's apocenter. Thus, the outer orbit's apocenter is a stable conjunction point, while its pericenter is an unstable one. It can also be shown that conjunctions at the inner orbit's pericenter are stable, while those at its apocenter are unstable. Thus, during a resonance, extreme close encounters (e.g. conjunction at the pericenter of the outer orbit and the apocenter of the inner orbit) are avoided and the orbits are stabilized, as the case of the 3:2 resonances between the Plutinos and Neptune. The repetition of the same orbital configuration, however, allow the orbital elements to be

systematically perturbed, leading to changes of orbital elements on short timescales.

Since mean-motion resonances are associated with an expansion term of the disturbing function, the angular parameter ϕ for that term, commonly called the resonant angle or resonant argument, can be used to characterize a resonance. We rewrite Eq. (2.15) in the form usually used for mean-motion resonances:

Figure 2.3: Stability of mean motion resonances. During a resonance, the conjunction point always moves towards the apocenter of the outer orbit and towards the pericenter of the inner orbit.

$$\phi = (p+q)\,\lambda_2 - p\,\lambda_1 + j_3\,\varpi_1 + j_4\,\varpi_2 + j_5\,\Omega_1 + j_6\,\Omega_2. \qquad (2.18)$$

The new coefficients $p = -j_1$, $q = j_1 + j_2$, and all integers are still subject to the d'Alembert conditions (Eqs. 2.13 and 2.14). The sum $|j_3| + |j_4| + |j_5| + j_6|$, which is usually equal to $|q|$, is the order of the resonance since it represents how many small quantities (e_1, e_2, $\sin i_1$, $\sin i_2$) appear in the resonant strength Eq. (2.12).

There are two possible behaviors for the resonant angle ϕ: circulation through a full 360° when the two orbits are distant from the corresponding resonance, or libration through a restricted range of values when the resonance is nearby. The libration amplitude of ϕ decreases to zero as the resonance is approached, and at

21

exact resonance, the resonant argument satisfies

$$\dot{\phi} = 0. \tag{2.19}$$

If the orbits do not precess, i.e., $\dot{\Omega}_1 = \dot{\Omega}_2 = \dot{\varpi}_1 = \dot{\varpi}_2 = 0$, this equation leads to the resonant condition Eq. (2.17): resonances occur when the two orbital mean-motions are an exact ratio of integers. In reality, however, both the oblateness of the planet (Section 2.4) and secular and resonant perturbations from other satellites cause orbits to precess, leading to resonance splitting qualitatively similar to the Zeeman effect in which the energy levels of an atom separate when a magnetic field is applied. Since the nodal and apsidal precession rates in Eq. (2.18) are much slower than orbital mean motions, these resonances are still packed into a small region around the location determined by the ratio of the satellite mean motions (Eq. 2.17). In Part II of this dissertation, we will investigate the resonant history of the inner Neptunian system and study how the orbits of these moons have been affected over time.

2.4 Rotational Deformation

The spin of a planet induces a bulge to appear along the planet's equator – for example, Earth's equatorial radius is about 22 km bigger than its polar radius – and this deviation from a spherical shape causes perturbations to the Keplerian orbit of a satellite. Roy (2005) used the disturbing function and Lagrange's planetary equations to derive the low-order effects for small eccentricities and inclinations, which is usually sufficient for satellite dynamics. We follow his approach here. In the ideal situation,

the rotational deformation is axisymmetric, and the perturbation potential, or the disturbing function, is given by

$$\mathcal{R}^{rot} = \frac{Gm_p}{r} \sum_{k=2}^{\infty} J_k \left(\frac{R_p}{r}\right)^k P_k(\sin\alpha), \qquad (2.20)$$

where R_p is the planetary radius, r is the distance from the center of the planet, α is the latitude measured from the equatorial plane, $P_k(\sin\alpha)$ is the Legendre polynomial of degree k, and the dimensionless coefficients J_k are determined by the planet's shape. An arbitrary axisymmetric potential can be represented by a judicious choice of the dimensionless coefficients J_k, which represent the magnitudes of the different harmonics. If a planet is symmetric about its equator plane, we have $J_3 = J_5 = J_7 = \cdots = 0$. To an excellent approximation, this is the case for all gaseous planets. More general expansions are needed for terrestrial planets (Hamilton, 1994) whose mass distributions are usually non-axisymmetric.

Assuming that the orbit differs only slightly from a Keplerian ellipse, r and $\sin\alpha$ can be converted to orbital elements by

$$r = \frac{a(1-e^2)}{1+e\cos f},$$

$$\sin\alpha = \sin i \sin(f+\omega).$$

Substituting these expressions into Eq. (2.20), dropping terms of J_6 and higher, and averaging over an orbital period, we get, to second-order in e and $\sin i$,

$$\langle \mathcal{R}^{rot} \rangle = \frac{1}{2}n^2a^2 \left[\frac{3}{2}J_2 \left(\frac{R_p}{r}\right)^2 - \frac{9}{8}J_2^2 \left(\frac{R_p}{r}\right)^4 - \frac{15}{4}J_4 \left(\frac{R_p}{r}\right)^4\right] e^2$$

$$- \frac{1}{2}n^2a^2 \left[\frac{3}{2}J_2 \left(\frac{R_p}{r}\right)^2 - \frac{27}{8}J_2^2 \left(\frac{R_p}{r}\right)^4 - \frac{15}{4}J_4 \left(\frac{R_p}{r}\right)^4\right] \sin^2 i. \qquad (2.21)$$

23

Table 2.1: Gravitational properties of major planets

Planet	R (km)	$J_2(10^{-5})$	$J_4(10^{-5})$	k_2	Q
Mercury	2,440	6	-	-	≤ 190
Venus	6,052	0.4	0.2	0.25	≤ 17
Earth	6,378	108.3	-0.2	0.299	12
Mars	3,394	196	-1.9	0.14	86
Jupiter	71,398	1473.6	-58.7	0.58	$(0.6 - 20) \times 10^5$
Saturn	60,330	1629.8	-91.5	0.40	$\geq 16,000$
Uranus	26,200	334.3	-2.9	0.36	11,000 - 39,000
Neptune	25,225	341.1	-3.5	0.41	9,000 - 36,000

References: The Love numbers k_2 for the giant planets are from Burša (1992); their tidal Q's are from Table 6.2 of this dissertation; Q's of Mercury and Venus are from Goldreich and Soter (1966); all other data are from Murray and Dermott (1999).

Since neither Ω nor ϖ appears in $\langle \mathcal{R}^{rot} \rangle$, planetary oblateness does not affect e and i (see Eqs. 2.7 and 2.8). Nevertheless, it causes precessions of both the ascending node and the pericenter. The precession rates come from combining Lagrange's equations (Eqs. 2.9 and 2.10) with Eq. (2.21):

$$\dot{\varpi} = + n \left[\frac{3}{2} J_2 \left(\frac{R_p}{r} \right)^2 - \frac{9}{8} J_2^2 \left(\frac{R_p}{r} \right)^4 - \frac{15}{4} J_4 \left(\frac{R_p}{r} \right)^4 \right], \qquad (2.22)$$

$$\dot{\Omega} = - n \left[\frac{3}{2} J_2 \left(\frac{R_p}{r} \right)^2 - \frac{27}{8} J_2^2 \left(\frac{R_p}{r} \right)^4 - \frac{15}{4} J_4 \left(\frac{R_p}{r} \right)^4 \right]. \qquad (2.23)$$

The signs of the two expressions indicate that, for a prograde satellite, the pericenter precesses, while the ascending node regresses. For a retrograde satellite, however, the opposite is true, as we shall see in Section 4 for Neptune's large satellite Triton. Table 2.1 lists the J_2 and J_4 parameters for the major planets. Giant planets have much larger J_2 and J_4 values due to their faster rotation rates.

2.5 Tides
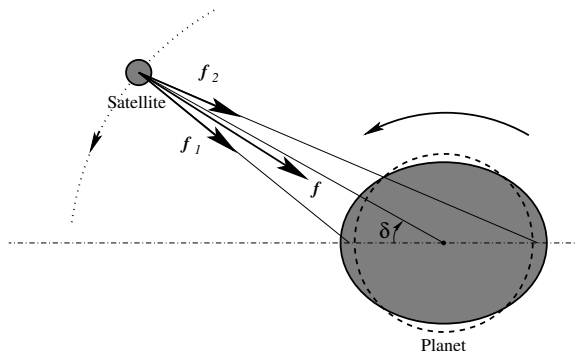
Figure 2.4: Tidal torque. Because the near tidal bulge pulls the satellite more strongly than the far one does, the net force **f** does not point exactly toward the center of the planet, resulting in a tangential component of the total force along the direction of the satellite's velocity.

Planets and satellites are not rigid bodies. Because the gravitational pull from a satellite differs at different locations around the planet, the shape of the planet is changed: it elongates along the planet-satellite line and forms two tidal bulges (Fig. 2.4). In exactly the same way, a planet also raises tides on its satellites. Tidal deformation perturbs orbits of satellites just as planetary oblateness does; the effect was first discussed by Darwin (1879, 1880), and later expanded and systematized by Kaula (1964) and MacDonald (1964). Following Goldreich and Soter (1966) and Burns (1977), we show how tides affect orbits physically. An excellent summary of tides and tidal interactions is also given by Murray and Dermott (1999).

If a satellite moves along a circle at the same angular rate as the spin of its planet, the tidal bulge on the planet always aligns with the planet-satellite line. As a result, the total gravitational torque on the satellite is zero and the satellite's orbit is not affected. When this happens, the satellite is synchronized. Given a planet's spin rate Ω_p, its synchronous radius for satellites can be easily calculated:

$$r^{syn} = \left(\frac{Gm_p}{\Omega_p^2} \right)^{1/3}.$$

When a prograde satellite is away from the synchronous orbit, however, the planetary tidal bulge can apply a net torque on the satellite as illustrated in Fig. 2.4. This figure shows the case when a satellite is outside of the synchronous orbit, where it orbits more slowly than the planet spins. Because of internal friction, tides take some time to develop and the planet's fast spin carries along the tidal bulge ahead of the satellite. Subsequently, because of the difference between the gravitational pulls from different side of the planet (Fig. 2.4), a tangential component of the gravitational force is applied in the direction of the satellite's motion and accelerates it. As energy is pumped into the satellite's orbit, the orbit expands away from the planet and its mean motion decreases. On the other hand, since energy is drained from the planet, lost both to the satellite and to internal frictions, the planet's spin slows down. The opposite is true if a satellite is inside the synchronous orbit: the tidal bulge lags behind the satellite and energy is transferred from the satellite's orbit to the planet's spin and to tidal dissipation. The satellite migrates towards the planet, its orbital velocity speeds up, and the planetary rotation rate increases. Finally, if a satellite is in a retrograde orbit in which it revolves in the opposite direction of the planet's spin, like Neptune's Triton, the tidal bulge always lags behind the satellite, and the satellite's orbit always decays inward.

The tidal migration rate of the satellite and the despin rate of the planet have been calculated by many authors. Here we adapt the equations given by Murray and

26

Dermott (1999):

$$\dot{n} = \text{sign}(\Omega_p - n) \frac{9}{2} \frac{k_{2p}}{Q_p} \left(\frac{R_p}{a}\right)^5 \mu_s \, n^s, \tag{2.24}$$

$$\dot{\Omega}_p = -\text{sign}(\Omega_p - n) \frac{15}{4} \frac{k_{2p}}{Q_p} \left(\frac{R_p}{a}\right)^3 \mu_s^2 \, n^2. \tag{2.25}$$

Here $\mu_s = m_s/m_p \ll 1$ is the satellite-to-planet mass ratio, and k_{2p} is the Love number of the planet (Table 2.1), which is a dimensionless parameter characterizing a planet's tides-raising ability and determined only by the planet's internal structure. It is usually less dependent on planetary composition than Q_p is and can be estimated based on planetary models (see Gavrilov and Zharkov, 1977; Burša, 1992). The tidal dissipation factor Q_p quantifies the ability of the planet to dissipate energy; a smaller Q_p means stronger tidal friction and higher energy loss rate. Q_p generally depends on the amplitude and frequency of tides (Goldreich and Soter, 1966), but this dependence is thought to be very weak for the low-frequency tides with small amplitudes, expected on most planets and satellites. There is a simple relation between Q_p and the tidal lag angle δ (Fig. 2.4):

$$\sin 2\delta = 1/Q_p.$$

Note that Eqs. (2.24) and (2.25) change sign at the synchronous orbit as described earlier. The dissipation factor Q_p is usually estimated through dynamical constraints (see Goldreich and Soter, 1966; Yoder and Peale, 1981; Peale et al., 1980; Tittemore and Wisdom, 1989; Banfield and Murray, 1992). In Chapter 6 we use new dynamical arguments to constrain Neptune's Q.

Effects from satellite tides are similar:

$$\dot{n} = \text{sign}(\Omega_s - n) \frac{9}{2} \frac{k_{2s}}{Q_s} \left(\frac{R_s}{a}\right)^5 \frac{1}{\mu_s} n^2 \qquad (2.26)$$

$$\dot{\Omega}_s = -\text{sign}(\Omega_s - n) \frac{15}{4} \frac{k_{2s}}{Q_s} \left(\frac{R_s}{a}\right)^3 \frac{1}{\mu_s^2} n^2, \qquad (2.27)$$

where R_s is the satellite radius, and k_{2s} and Q_s are the Love number and tidal dissipation factor of the satellite, respectively. Among the four rates Eqs. (2.24 - 2.27), $\dot{\Omega}_s$ is by far the largest (Table 2.2). Thus, satellites usually despin to a synchronous state so that one face is locked toward the planet as is the case for our Moon. All regular satellites in the Solar System are currently spin-synchronized. As a result, satellite tides are not important for circular orbits, and satellite migrations are mostly determined by planetary tides. Table 2.2 shows the tidal migration timescale of satellites. Satellites of all giant planets have probably migrated by less than a few planet radii over the age of the Solar System. Because of small Q_p values for terrestrial planets, both the Moon and Phobos have migrated substantially. During tidal migration, the planet continues to transfer angular momentum and energy to the satellite's orbit until the planetary spin is also synchronized fully to the satellite mean motion and the system reaches double synchronization, as is the case for the Pluto-Charon system.

Satellite tides, however, can circularize an eccentric orbit very effectively even when the satellite has reached near-synchronization. This is because tides on the satellite are stronger when it is near pericenter and weaker when it is near apocenter, so tides rise and fall with the orbital period. Because the tidal force is nearly radial, the orbital angular momentum is conserved, but the orbital energy decreases. Thus

Table 2.2: Tidal timescales for natural satellites

Satellite	$\Omega_s/\dot{\Omega}_s$ (yr)	$-e/\dot{e}$ (yr)	$R_p/\dot{a}$ (yr)	$i/\dot{i}$ (yr)
Moon	2×10^7	2×10^{10}	2×10^8	-2×10^{11}
Phobos	3×10^5	5×10^9	-1×10^8	1×10^9
Io	2×10^3	6×10^6	1×10^{10}	-2×10^{11}
Europa	4×10^4	3×10^8	2×10^{11}	-1×10^{13}
Mimas	1×10^3	3×10^8	5×10^{10}	-5×10^{10}
Titan	3×10^4	2×10^9	5×10^{11}	-3×10^{13}
Miranda	8×10^3	3×10^8	2×10^{10}	-4×10^{11}
Ariel	1×10^4	6×10^7	1×10^{10}	-2×10^{11}
Triton	4×10^4	9×10^7	-1×10^{10}	7×10^{11}
Proteus	1×10^3	9×10^7	1×10^{10}	-2×10^{11}
Larissa	2×10^2	9×10^7	-2×10^{10}	1×10^{11}

These timescales are rough estimates: we use k_{2p} and Q_p from Table 2.1; k_{2s} and $\tilde{\mu}_s$ are estimated by Eq. 2.29 and $\tilde{\mu}_s \approx (10^4 \text{ km}/R_s)^2$ given in Murray and Dermott (1999); Q_s are all assumed to be 100 except for the Moon, for which Yoder (1995) estimates $Q_M = 27$.

a satellite's eccentricity is forced to decrease at a rate given by Goldreich (1963):

$$\frac{\dot{e}}{e} = -\frac{63}{4} \frac{1}{\tilde{\mu}_s Q_s \mu_s} \left(\frac{R_s}{a}\right)^5 n, \tag{2.28}$$

where $\tilde{\mu}_s$ is the ratio between elastic and gravitational forces, another measure of the internal strength. For a homogeneous solid body, k_{2s} and $\tilde{\mu}_s$ are related by

$$k_{2s} = \frac{3/2}{1 + \tilde{\mu}_s}. \tag{2.29}$$

Tidal circularization timescales for satellites are listed in Table 2.2. The eccentricities of most satellites have damped away over the age of the Solar System, except, again, for those of the Moon and Phobos. The former is too far away for Earth to raise strong tides while the latter is simply too small for tides to be effective.

Jeffreys (1961) found that, in addition to causing outward satellite migration, planetary tides also act to increase the orbital eccentricity. The effect can be under-

stood by considering the tidal force to be applied as an impulse at pericenter – if a rises, e must rise as well. Goldreich (1963) showed that, however, this effect is usually much weaker than eccentricity damping by satellite tides. Orbital inclination can also be affected by tides because the rotation of the planet shifts the tidal bulge off the satellite's orbital plane. Kaula (1964) found that, for small orbital tilts, inclinations change at nearly the migration rate:

$$\frac{1}{i}\frac{di}{dt} = -\frac{1}{4a}\frac{da}{dt}.$$

(2.30)

Since satellite inclinations are usually very small, this effect can be ignored in most cases, as the long timescales in Table 2.2 indicate. For most satellites, the changes of inclination are less than a tenth of their current tilts over the history of the Solar System. In Part II, we use this evidence to argue that all past inclination excitations of the small Neptunian satellites are retained until today.

Part II

Orbital Resonances in the Neptunian System

Chapter 3

Background

The investigation of the resonant history among the small inner Neptunian satellites is motivated by the study of the resonant excitation of the inclinations of Amalthea and Thebe by Hamilton and Proctor (unpublished). In this chapter, we provide some background information about the Neptunian satellites and their tidal migration history, as well as about the numerical tools and techniques we will use to carry out our simulations. In Chapter 4, we define two proper orbital elements that are necessary to analyze resonances in the system. Then, in Chapter 5, we detail various Proteus resonance passages and discuss their immediate implications. Finally, in Chapter 6, we give constraints on several physical parameters for the system. Part of this research is published as Zhang and Hamilton (2007); the remainder has also been submitted to *Icarus* for publication.

3.1   The Neptunian Satellites

Prior to the *Voyager 2* encounter, large icy Triton and distant irregular Nereid were Neptune's only known satellites. Triton is located where one usually finds regular satellites (close moons in circular equatorial orbits, which are believed to have formed together with their parent planets). The moon follows a circular path, but

its orbit is retrograde and significantly tilted, which is common only among irregular satellites (small distant moons following highly inclined and elongated paths, thought to be captured objects). Triton's unique properties imply a capture origin followed by orbital evolution featuring tidal damping and circularization. Although different capture mechanisms have been proposed (McKinnon, 1984; Goldreich et al., 1989; Agnor and Hamilton, 2006), in all scenarios Triton's post-captured orbit is expected to be remote and extremely eccentric ($e > 0.9$). During its subsequent orbital circularization, Triton forced Neptune's original regular satellites to collide with one another, resulting in a circum-Neptunian debris disk. Most of the debris was probably swept up by Triton (Ćuk and Gladman, 2005), while some material close to Neptune survived to form a new generation of satellites with an accretion timescale of tens of years (Banfield and Murray, 1992). Among the survivors of this cataclysm are the six small moonlets discovered by *Voyager 2* in 1989 (Smith et al., 1989, see Fig. 3.1).

Voyager 2 also found several narrow rings interspersed amongst the satellites within a few Neptune radii, and found the ring arcs hinted at by stellar occultation years earlier. Karkoschka (2003) reexamined the Voyager images later, and derived more accurate sizes and shapes of the new satellites. Proteus, the largest one, is only about 400 kilometers in diameter, tinier than even the smallest classical satellite of Uranus, Miranda. Owen et al. (1991) used Voyager data to calculate the orbital elements of these small satellites, which were later refined by Jacobson and Owen (2004) with the inclusion of recent data from the *Hubble Space Telescope* and ground-based observations. Both analyses show that all the small moons are in direct near-circular

Table 3.1: Inner Neptunian satellites and Triton

Name	R (km)	a (km)	e $(\times 10^{-3})$	i^{Lap} $(°)$	i^{fr} $(°)$
Naiad	33 ± 3	48,227	0.4 ± 0.3	0.5118	4.75 ± 0.03
Thalassa	41 ± 3	50,075	0.2 ± 0.2	0.5130	0.21 ± 0.02
Despina	75 ± 3	52,526	0.2 ± 0.2	0.5149	0.06 ± 0.01
Galatea	88 ± 4	61,953	0.04 ± 0.090	0.5262	0.06 ± 0.01
Larissa	97 ± 3	73,548	1.39 ± 0.08	0.5545	0.205 ± 0.009
Proteus	210 ± 7	117,647	0.53 ± 0.09	1.0546	0.026 ± 0.007
Triton	1353	354,759	0.0157	-	156.83

Average radii of the small satellites ($\bar{R}$) are from Karkoschka (2003); their orbital elements (semi-major axis a, eccentricity e, inclination of local Laplace plane i^{Lap}, and free inclination i^{fr}) are from Jacobson and Owen (2004). Neptune's equator plane is tilted by $\epsilon = 0.5064°$ from the invariable plane (see Fig. 4.1); these small satellites lie nearly in the equator plane. Orbital data of Triton are from Jacobson et al. (1991).

orbits with small, but non-zero, inclinations. Their parameters are listed in Table 3.1.
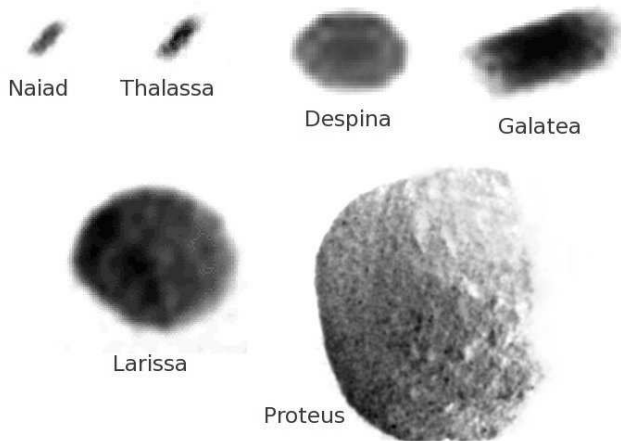
Figure 3.1: *Voyager 2* images of the six small inner Neptunian satellites. Their sizes are roughly to scale. Images courtesy of NASA.

Smith et al. (1989) estimated the cometary bombardment rate near Neptune and pointed out that, of the six small satellites, only Proteus was likely to survive disruptive collisions over the age of the Solar System. The innermost and smallest satellite, Naiad, might not last much longer than 2 to 2.5 billion years, while the intermediate objects might have been destroyed during an early period of heavy bombardment. In any case, all six small satellites probably formed only after Triton's orbital migration and circularization was nearly

complete and the large moon was close to its current circular tilted retrograde orbit (Hamilton et al., 2005). Triton's large orbital tilt induces a strong forced component in the inclination of each satellite's orbit (see Chapter 4). These forced inclinations define the location of the warped Laplace plane, about whose normal the satellite's orbital plane precesses. Measured from their local Laplace planes, the current free orbital inclinations (i^{fr}) of the small satellites are only a few hundredths to tenths of a degree, with one exception (4.75° for tiny Naiad). It is the contention of this work that these free tilts, despite being very small, arose from dynamical excitations during orbital evolution. Physically, the debris disk from which the satellites formed should have damped rapidly into a very thin layer lying in the warped Laplace plane. Satellites formed from this slim disk should initially have free inclinations $i^{fr} \ll 0.001°$, perhaps similar to the thickness of Saturn's ring. A reasonable explanation for the current non-zero tilts of the satellites thus requires an examination of their orbital evolution history.

3.2   Tidal Evolution and Mean-Motion Resonance Passage

Tidal friction between a satellite and its parent planet determines the satellite's orbital evolution over a long time span (Darwin, 1880; Burns, 1977). The physical effects of tides have been discussed in Section 2.5. Satellite orbits migrate due to planetary tides according to

$$\frac{\dot{a}}{a} = \pm \frac{3k_{2N}}{Q_N} \mu_s \left(\frac{R_N}{a}\right)^5 n,$$

(3.1)

where we have rewritten Eq. (2.24) in terms of $\dot{a}$, and the sign in Eq. (3.1) depends on the satellite's location relative to the synchronous orbit. For the Neptunian system, the synchronous orbit lies between the orbits of Proteus and Larissa, which means that Proteus' orbit has expanded over time while the orbits of the other satellites have shrunk. The large gap between the orbits of Proteus and Larissa may be evidence for this divergence (Fig. 3.2).
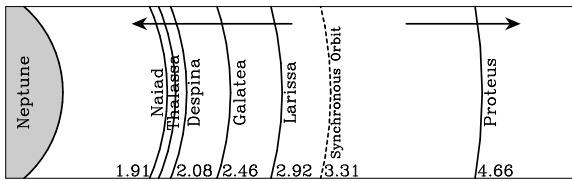
Figure 3.2: Semi-major axes of the small inner Neptunian satellites in planetary radii. The two arrows indicate the direction of tidal migration.

The tidal migration timescale is rather difficult to estimate. Although $k_{2N} = 0.41$ is theoretically determined by Burša (1992), the uncertainty in Q_N prevents a precise calculation (Goldreich and Soter, 1966). Banfield and Murray (1992) estimated $12,000 < Q_N < 330,000$, leading to timescales uncertain by more than an order of magnitude. Here we note that the distances between the two satellites and the synchronous orbit are $1.3\,R_N$ for Proteus and $0.4\,R_N$ for Larissa, implying that they have migrated by no more than $\sim R_N$ over the age of the Solar System. Triton, due to its retrograde orbit, spirals slowly inward with a typical timescale $\sim 10^{10}$ years (Table 2.2); this inward drift can be safely ignored in resonant studies.

Due to tidal migration, orbital periods of the small satellites change over time, causing satellites to pass through mean-motion resonances (Section 2.3). The behavior of the orbital elements during resonance passage depends on whether the two orbits are converging or diverging. For first- and second-order resonances $(|j_3| + |j_4| +$

$|j_5| + |j_6| = 1$ or 2 in Eq. 2.18), if the two orbits diverge from each other (as Proteus and Larissa) and pass through a resonance, the orbital eccentricities and inclinations are subject to sharp changes or kicks (Hamilton and Burns, 1993), which can be either positive or negative. The signs and magnitudes of these kicks depend not only on the resonant strength, but also on the exact phase (value of ϕ) when the resonance is encountered (Peale, 1986). However, kick amplitudes are predictable if the two satellites diverge so slowly that the variation of orbital elements is in the adiabatic limit both before and after a resonance encounter. In this case, the kicks to eccentricities and inclinations are always positive, and the kick magnitudes can be obtained analytically by a Hamiltonian analysis (Peale, 1976; Murray and Dermott, 1999). In contrast, when two converging orbits pass through a resonance, they can be captured into a resonant state and may remain locked therein unless perturbations from other objects or nearby resonances force them out (Greenberg et al., 1972; Malhotra and Dermott, 1990). If tides continue to act on objects trapped in a resonance, the affected eccentricities and/or inclinations keep growing on the tidal migration timescale (Hamilton, 1994).

In addition to tidal migration of a, tides affect other orbital elements as well (Eqs. 2.28 and 2.30). Based on reasonable assumptions for Q_T and $\tilde{\mu}_T$, Goldreich and Soter (1966) estimated that the circularization timescale for Triton is of order 10^8 years. Triton, therefore, has followed a nearly circular path for most of Solar System history. The eccentricity-damping timescales for the small satellites are longer because of their small sizes, but are still significantly shorter than a billion years (Table 2.2),

which is consistent with the zero eccentricities of Naiad, Thalassa, Despina, and Galatea (Table 3.1). The eccentricities of Proteus and Larissa, however, stand out as significantly larger than zero. We will explain in Section 5.1.1 that excitations from the recent 2:1 Proteus-Larissa mean-motion resonance passage are responsible.

For a satellite with a small tilt, the tidal effect on the inclinations is very weak (Eq. 2.30). The inclinations of the inner Neptunian satellites should change by less than a tenth of their current values over the age of the Solar System (Eq. 2.30). As a result, any inclinations acquired by other means, e.g., resonant excitations, are preserved throughout tidal evolution. This leads directly to the main idea of this work: the small satellites' current orbital tilts contain clues to dynamical events of the past. We begin our investigation by an overview of possible resonances that may have once been active among the Neptunian satellites.

3.3   Resonant History of the Neptunian System

As we mention earlier, Proteus migrates away from Neptune, while all other satellites spiral inwards. A satellite's migration rate is proportional to its mass, and has a steep inverse dependence on its orbital semi-major axis (Eq. 3.1). Since Larissa, Galatea, and Despina have comparable masses (within a factor of 2), the innermost of these migrates most rapidly, and, hence, their orbits all diverge from one another. Diverging orbits usually lead to resonant kicks during which satellite orbital elements change sharply (Hamilton and Burns, 1993). Due to the much smaller masses of the innermost satellties, Naiad and Thalassa, their orbits evolve more slowly and are

approached by those of the next three satellites. Converging orbits typically lead to resonant trapping, as has been suggested as the explanation for the large inclination of Naiad by Banfield and Murray (1992).

Over the history of the Solar System, the inner Neptunian satellites migrated slowly enough that most of the first- and second-order mean-motion resonances were traversed in the adiabatic limit. Magnitudes of resonant kicks on satellite inclinations are then predictable both analytically (Peale, 1976) and numerically. Higher-order resonances are often not transversed adiabatically, but their kicks are smaller by about an order of magnitude, and thus add negligibly to the total inclination growth.

Because satellite mean motions are much larger than orbital precession rates, resonances cluster in discrete narrow zones near where the ratio of satellite orbital periods is a rational number ($(p + q)/p$ in Eq. 2.18). We integrate Eq. (3.1) for each satellite and locate all the first- and second-order resonant zones ($q = 1$ and $q = 2$), as shown in Fig. 3.3. We stop the integration when Larissa is fairly close to the synchronous orbit and the unphysical discontinuity in $\dot{a}/a$ becomes problematic. Because of this over-simplification for satellites near synchronous orbit, the left-hand-side of the plot is less accurate than the right, especially for Larissa. As the time axis indicates, the integration is much longer than the age of the Solar System, but the evolutionary timescale depends on Neptune's Q and the satellite masses, all of which are poorly constrained. Here we have used $Q_N = 20,000$ and a common satellite mean density $\bar{\rho} = 0.6\,g/cm^3$ based on estimates for the giant planets and icy satellites. Under these assumptions, Proteus was $0.28\,R_N$ closer to Neptune 4 billion years ago
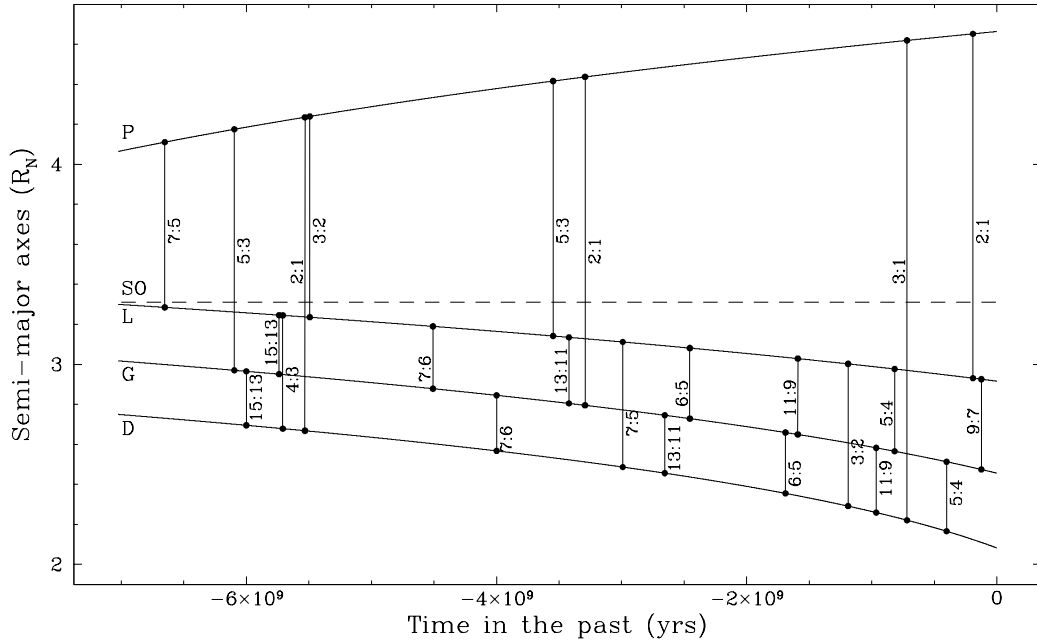
Figure 3.3: Possible past first- and second-order mean-motion resonances among Proteus (P), Larissa (L), Galatea (G), and Despina (D). We integrate Eq. (3.1) backward until Larissa is fairly close to the synchronous orbit (SO), assuming $Q_N = 20,000$ and a uniform satellite mean density of $\bar{\rho} = 0.6\,g/cm^3$. Black solid curves show the migration tracks of the four satellites, and the dashed horizontal line denotes the synchronous orbit. The vertical lines represent strong resonant zones for different pairs of satellites. The time scale along the bottom axis depends on Q_N and $\bar{\rho}$. For different values of these parameters, multiply all times by a factor of $\frac{Q_N/20,000}{\bar{\rho}/(0.6\,g/cm^3)}$.

($\sim$ age of the small satellites) than it is today and Larissa, Galatea, and Despina have migrated towards the planet by $0.24\,R_N$, $0.39\,R_N$, and $0.49\,R_N$, respectively. A larger Q_N or a lower satellite density would result in a slower evolution, as described in the caption of Fig. 3.3. Thus the origin of the system could occur anywhere along the horizontal axis of Fig. 3.3, depending on the actual values of Q_N and $\bar{\rho}$.

With our assumptions of $Q_N = 20,000$ and $\bar{\rho} = 0.6\,g/cm^3$, the satellites go through approximately 16 resonant zones involving first- and second-order mean-motion resonances (Fig. 3.3) since the small satellites formed ~ 4 billion years ago.

For different Q_N and $\bar{\rho}$, a different number of past resonances may have occurred. Our strategy here is to work backwards in time from the present to find out which of these resonances actually occurred and determine what their effects were. We focus on orbital inclinations which are particularly unaffected by tides and hence accumulate over time, leaving a "fossil record" visible in today's orbits.

3.4   Computing Techniques

Our simulations were carried out with the *HNDrag* module in the *HNBody* package (Rauch and Hamilton, 2002). *HNBody* is a general purpose, hierarchical N-body integrator, which implements both the symplectic mapping algorithms (Wisdom and Holman, 1991) and the classical Bulirsch-Stoer and Runge-Kutta algorithms. *HNDrag* expands the functionality of the original *HNBody* code by allowing additional drag forces to act on the satellites, which can simulate a wide range of gravitational and non-gravitational perturbations. Since our interest lies in long-term orbital evolution, we use the symplectic integrator for better performance. The integration stepsize is chosen so that there are at least 20 steps during each orbital period. We have performed convergence tests for several of our simulations with the number of sampling points per orbit ranging from 1 to 100. The results are consistent for all tests with greater than five steps per orbit. In the results presented here, we use a cautious 20 steps per orbit to guarantee convergence. We also confirmed the stability of the code by performing a series of simulations with slightly different initial conditions. We conducted the test with a system consisting of a planet and two satellites, with

an artificial drag force pulling the satellites through several mean-motion resonances. These tests are similar to the physical problem that we are exploring, and they lead to consistent results after 10^8 years.

The output of *HNDrag* can be set to either osculating orbital elements or Cartesian positions and velocities. The osculating elements are a set of projected Keplerian orbital elements for each instant, calculated with the assumption of no extra perturbations. However, perturbations from both Neptune's oblateness and Triton cause the osculating elements to vary artificially over a single orbital period. We minimize this effect by using geometric elements, which define the actual shape of the orbit. Following Greenberg (1981), we take the position and velocity output from *HNDrag* and convert it to geometric orbital elements, correcting for first-order J_2 perturbations with our conversion program *cj2*. This procedure greatly reduces unphysical oscillations in the orbital elements.

To determine the evolutionary history of the two Neptunian satellites, it would be best to follow their orbits for 4 billion years. As this is not practical with current computing technology, we take advantage of the fact that mean-motion resonance passages take place only at discrete locations. During most of the evolution when the moons are not in resonance, we apply the tidal evolution equations (Eqs. 3.1 and 2.28) to damp eccentricities and move satellites away from the synchronous orbit. Typical resonance passage times, with the slowest migration rate that we use, are on the order of 10 million years; we only simulate these 10-million-year segments, which greatly reduces the computational burden.

The simulated system consists of Neptune (with an equatorial bulge), Proteus, and Larissa, with Triton included (for our inclination study) or excluded (for our eccentricity study). We ignore the Sun in our simulations because its perturbation on the small satellites is much smaller than Triton's. For simplicity, we fix the semi-major axis of Larissa, and apply a simple drag force on Proteus to move it slowly outward across the resonant zone. In reality, both satellites are moving at time-dependent rates. But since most of the strong resonances are traversed slowly (in the adiabatic limit), the kicks to the orbital eccentricities and inclinations are independent of whether one satellite or both are migrating, the rate of migration, and even the nature of the drag force.

Most of our simulations are performed on the *Borg* Beowulf cluster of 85 processors in the Astronomy Department at the University of Maryland. *HNDrag* is a single-thread program, and different simulations are dispatched to different nodes of the cluster through the *Condor* job control system. With these resources, typical simulation times range from 2 days to 2 weeks.

Chapter 4

Perturbations from Neptune's Oblateness and Triton

The orbital configuration of the Neptune system is different from other satellite systems in that a massive moon, Triton, orbits far from the equator plane, and its perturbation on the inner orbits is not negligible. Hence, a mathematical preparation for this special system is necessary before we proceed to analyze the resonances.

If Neptune were perfectly spherical, the rotational angular momentum of Neptune ($\mathbf{L}_N$) and the orbital angular momentum of Triton ($\mathbf{L}_T$) would both be constant with fixed directions in space. In reality, however, the oblateness of Neptune resulting from spin deformation causes Triton's orbital plane to precess slowly (Section 2.4). For a circularly-orbiting Triton, the nodal precession rate is (Danby, 1988, §11.15)

$$\dot{\Omega}_T = -\frac{3}{2} J_2 n_T \left(\frac{R_N}{a_T} \right)^2 \cos i_T \equiv g_T^{obl}. \tag{4.1}$$

Compared to Eq. (2.22), we only include the second-order J_2 term, and the additional $\cos i_T$ is necessary because Triton's large inclination and retrograde orbit. Neptune's $J_2 = 0.003411$. Triton's ascending node precess rather than the more common regression given in Eq. (2.22) because $i_T > 90°$. The precession period $\frac{2\pi}{\Omega_T}$ is about 600 years, significantly longer than Triton's 5.88-day orbital period.

Although $\mathbf{L}_T$ is no longer a constant vector due to the precession of Triton's orbital plane, the system still conserves its total angular momentum $\mathbf{L}_{tot} = \mathbf{L}_N + \mathbf{L}_T$ and, as
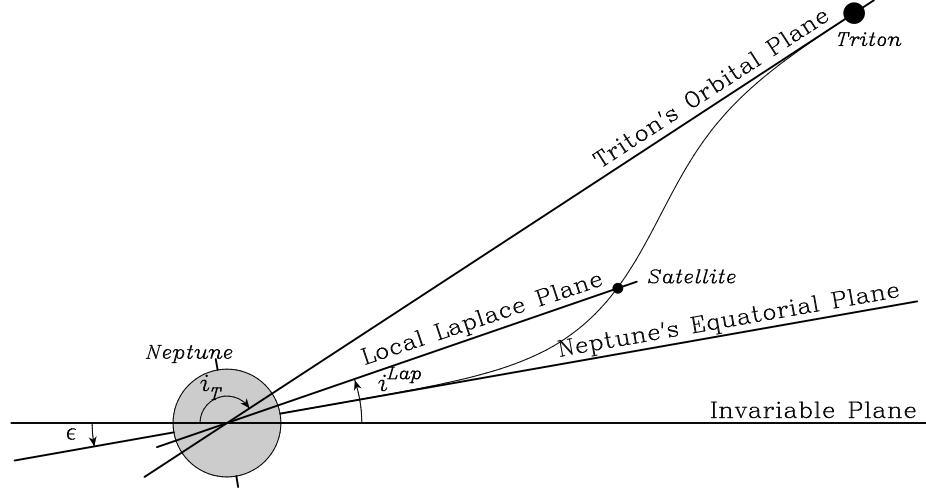
Figure 4.1: Laplace plane of the Neptune-Triton system. The plot shows a side view of the invariable plane, Neptune's equatorial plane, Triton's orbital plane, and the local Laplace plane of a small satellite. Here, i_T and ϵ are the inclinations of Triton's orbit and Neptune's equator, respectively. Note that they are measured from different sides of the invariable plane due to Triton's retrograde orbit. The inclination of the small satellite's local Laplace plane is given by i^{Lap}. The thin curve defines the shape of the warped Laplace plane for satellites at different distances, or for a debris disk inside Triton's orbit. The whole Laplace plane precesses together with Triton's orbit and Neptune's equator.

a result, the plane perpendicular to $\mathbf{L}_{tot}$ is fixed in space, which makes it a natural reference plane for the measurement of orbital elements. This plane is usually referred to as the invariable plane. In the Neptune-Triton system, it is tilted by $\epsilon = 0.5064°$ from Neptune's equatorial plane (Jacobson and Owen, 2004). Neptune's equatorial plane is always locked with Triton's orbital plane and the two precess together. We ignore the spin angular momentum of Triton and the orbital angular momenta of the other satellites since they are much smaller than $|\mathbf{L}_N|$ and $|\mathbf{L}_T|$.

Small inner Neptunian satellites ($m_s \ll m_T \ll m_N$) experience secular perturbations both from Neptune's oblateness and from Triton. The overall effects of these two perturbing components force the orbit of a small moon to precess about the moon's

local Laplace plane, which is distinct from both the invariable plane and Triton's orbital plane. Fig. 4.1 shows the warped Laplace plane in the Neptunian system. Near Neptune, the Laplace plane is close to the planet's equatorial plane, near Triton it is close to the large moon's orbital plane, and in between the plane is tilted at different angles. The nodes of Laplace planes at different distances, however, all lie along a line and move slowly with Triton's secular precession rate. Thus the whole warped disk precesses as a rigid body along with Triton's orbit and Neptune's equator. The location of the local Laplace plane at different distances from the central planet can be determined by analyzing the two competing perturbations. We undertake this analysis here, as it will lead to the identification of the new resonances that we will encounter in Chapter 5.

Neptune's oblateness causes the orbit of a small satellite to precess with a rate g^{obl} given by an expression similar to Eq. (4.1). Triton, as an external perturber, also causes both the satellite's pericenter and node to precess through secular interactions. We will study the eccentricity secular perturbations in great detail in Part III. In the Neptune-Triton system, however, the eccentricity effects are trivial due to Triton's nearly-circular orbit, but the inclination effects are important. Following similar calculations laid out in Section 7.2, we can obtain the corresponding nodal precession rate:

$$g^{sec} = -\frac{1}{4}\mu_T n\alpha^2 b_{3/2}^{(1)}(\alpha).$$

Here μ_T is the Triton-Neptune mass ratio, $\alpha = a/a_T$ is the semi-major axis ratio of the satellite and Triton, and $b_{3/2}^{(1)}(\alpha)$ is one of the Laplace coefficients, which depend

46

only on α (Murray and Dermott, 1999, §6.4).

Combining both the perturbations from Neptune's oblateness and the secular effects of Triton, we obtain the disturbing function for a small satellite:

$$\mathcal{R} = na^2 \left\{ \frac{1}{2}(g^{sec} + g^{obl})i^2 - g^{sec}(\pi - i_T)i\cos(\Omega - \Omega_T - \pi) \right\},$$

where the extra π symbols are due to Triton's retrograde orbit. The solution to the corresponding Lagrange's planetary equations for inclination (Eq. 2.8) and ascending node (Eq. 2.10) with the above disturbing function is

$$i\sin\Omega = i^{fr}\sin\Omega^{fr} + i^{Lap}\sin\Omega^{Lap}, \tag{4.2}$$

$$i\cos\Omega = i^{fr}\cos\Omega^{fr} + i^{Lap}\cos\Omega^{Lap}, \tag{4.3}$$

where

$$\Omega^{fr} = (g^{sec} + g^{obl})t + \Omega_0^{fr}.$$

The free inclination i^{fr} and the free node at the epoch Ω_0^{fr} are constants determined by the initial state. The angles i^{Lap} and Ω^{Lap} define the local Laplace plane of the satellite, as illustrated in Fig. 4.2a. The inclination of the local Laplace plane, also called the forced inclination, is

$$i^{Lap} = \frac{g^{sec}}{g^{sec} + g^{obl}}(\pi - i_T), \tag{4.4}$$

and the node of the local Laplace plane, or the forced node, is

$$\Omega^{Lap} = \Omega_T + \pi, \tag{4.5}$$

both of which are independent of the initial inclination and node of the satellite. Once the satellite's semi-major axis is given for a nearly-circular orbit, the satellite's local

47
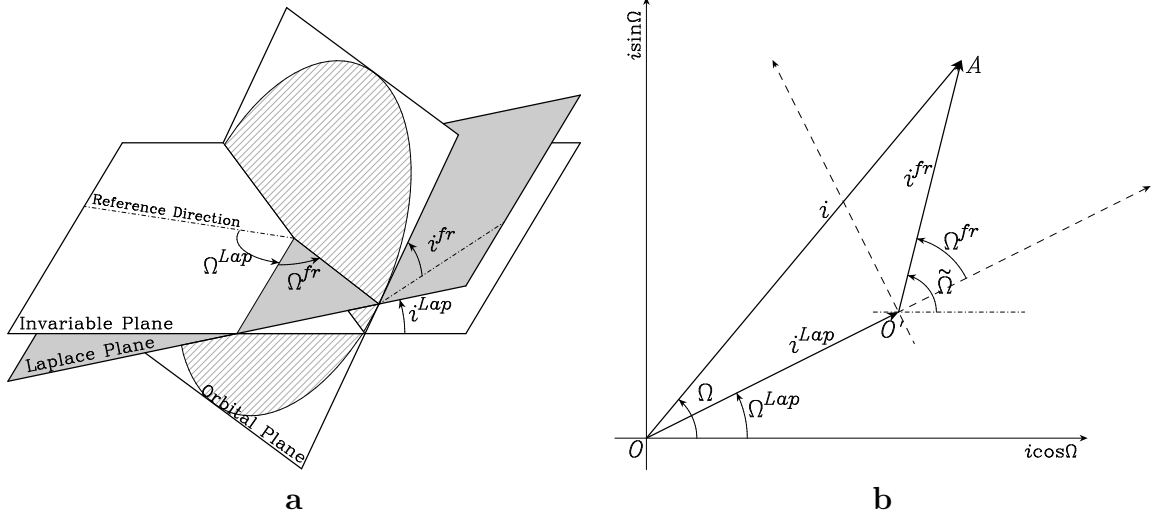
Figure 4.2: Definition of key orbital elements. i^{Lap}, Ω^{Lap}: inclination and longitude of ascending node of the local Laplace plane; i^{fr}, Ω^{fr}: free inclination and node of the satellite's orbit measured relative to its local Laplace plane; i, Ω: inclination and node of the satellite's orbit measured relative the invariable plane. The longitude of ascending node of the orbit is defined as the bent angle $\tilde{\Omega} = \Omega^{Lap} + \Omega^{fr}$ measured in two separate planes. **a**: the physical representation of the planes and orbital elements. **b**: the phase diagram showing the solutions Eqs. (4.2-4.3).

Laplace plane is determined. This plane precesses together with Triton's orbit and Neptune's equator. Our solution for the Laplace plane, Eqs. (4.4-4.5), is consistent with that derived by Dobrovolskis (1993) in the case of a solar perturbation on satellite orbits. However, his solution is simplified based on the fact that the external perturber is much further away from the planet than the perturbed satellite, which is not the case in the Neptune-Triton system.

Fig. 4.2b illustrates the solutions Eqs. (4.2 - 4.3) in a phase diagram of $i \sin \Omega$ versus $i \cos \Omega$. Perturbations on Triton by Neptune's rotational bulge cause $\overrightarrow{OO'}$ to precess (rotate counterclockwise) about the origin at rate $|g_T^{obl}|$, and perturbations on the small satellite by both Neptune's oblateness and Triton cause $\overrightarrow{O'A}$ to regress (rotate clockwise) around O' at the rate $|g^{sec} + g^{obl}|$. The vector sum of $\overrightarrow{OO'}$ and

$\overrightarrow{O'A}$ represents the inclination i and the longitude of the ascending node Ω of the small satellite relative to the invariable plane and an arbitrary reference direction. Measuring the direction of $\overrightarrow{O'A}$ from the reference direction, we find the angle

$$\tilde{\Omega} = \Omega^{Lap} + \Omega^{fr}, \tag{4.6}$$

which we redefine as the longitude of the satellite's ascending node. Fig. 4.2a shows its physical meaning: a bent angle partially in the invariable plane and partially in the Laplace plane, much like the longitude of pericenter ϖ. The free inclination is the tilt of the satellite's orbit with respect to its local Laplace plane, and the free node is measured from the node of the Laplace plane on the invariable plane.

Fig. 4.3 illustrates how the histories of (i, Ω) and (i^{fr}, Ω^{fr}) differ. We simulate the orbital evolution of a satellite at $8R_N$ (the satellite illustrated in Fig. 4.1) in the Neptune-Triton system. Measured relative to the Laplace plane, $i^{fr} \sim 3.5°$ is a constant over time and Ω^{fr} regresses at a constant rate. However, measured relative to the invariable plane, i oscillates around $i^{Lap} \sim 8.5°$, and Ω is forced to precess at nearly the same rate as the Laplace plane. If a small satellite is initially in its local Laplace plane ($i^{fr} = 0°$), it always stays in the plane and its inclination remains constant relative to the invariable plane. However, if it starts out of its local Laplace plane, it precesses about this plane and its inclination measured from the invariable plane oscillates. Hamilton (1996) noticed similar behavior when studying the orbit of a dust grain around Mars subject to strong solar perturbations (his Fig. 7).

The concept of the bent angle $\tilde{\Omega}$ can be more intuitively understood through a direct comparison to $\varpi = \Omega + \omega$. For an inclined orbit, ω is measured in the orbital
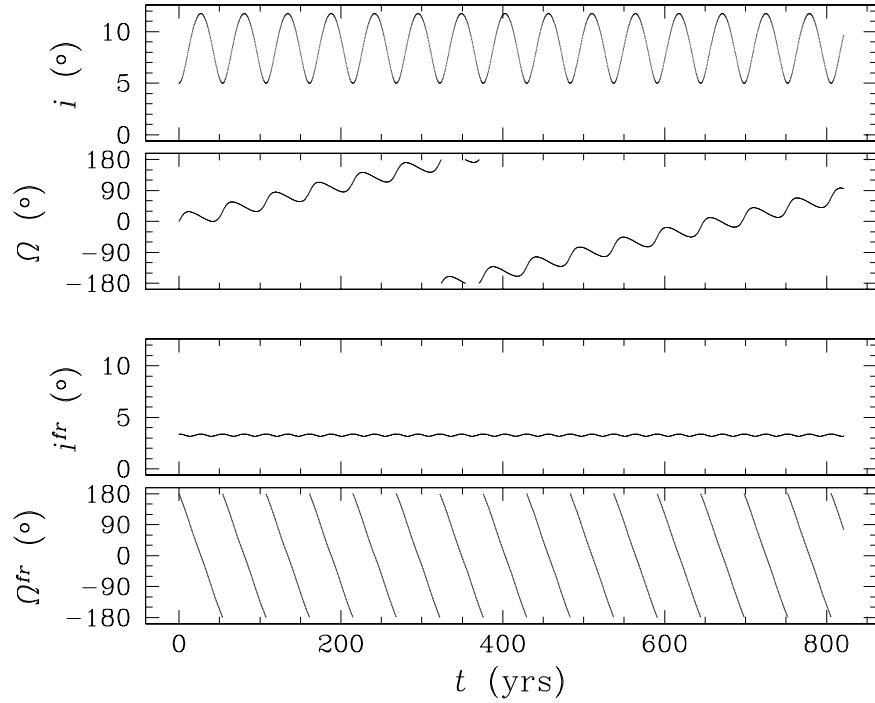
Figure 4.3: Inclination and node of a satellite at $a = 8R_N$ measured relative to the invariable plane (i, Ω) and the satellite's local Laplace plane (i^{fr}, Ω^{fr}). Measured from the Laplace plane, the free inclination, i^{fr}, is nearly constant, and the free node, Ω^{fr}, regresses uniformly with a ~ 50 year period. Orbital elements measured from the invariable plane display a more complicated evolution: here both i and Ω oscillate due to the satellite's orbital regression, while Ω is also dragged along with Triton's 600-year orbital precession.

plane, while Ω is measured in a reference plane (here the invariable plane). With the addition of Triton, however, there are two dynamically important planes in addition to the orbital plane – the invariable plane about which Triton's orbit precesses, and the local Laplace plane about which the small satellite's orbit regresses (Fig. 4.2). Because the local Laplace plane determines the dynamics, Ω^{fr} is measured in that plane, and we require an additional angle Ω^{Lap} to specify the location of the Laplace plane. As with ϖ, we are led to a bent angle definition (Eq. 4.6). Although not necessary for

this work, the definition of ϖ must also be updated in the Neptune-Triton system to: $\tilde{\varpi} = \tilde{\Omega} + \omega$, a perverse bent angle measured in three planes (represented with an equally perverse symbol). Here ω is measured from the ascending node of the orbital plane on the Laplace plane rather than on any other reference plane. For the orbits of Proteus and Larissa, the differences between $\tilde{\varpi}$ and ϖ are tiny because their free inclinations are so small. It is safe to replace $\tilde{\varpi}$ with ϖ in most cases.

With the new definition of the longitude of the ascending node $\tilde{\Omega}$ (Eq. 4.6) replacing Ω, as well as the new longitude of pericenter $\tilde{\varpi}$ replacing ϖ, resonant arguments defined in Eq. (2.18) hold the same form for resonances among the small satellites in the Neptune-Triton system as we shall see in Chapter 5. The resonance strengths (Eq. 2.12), however, depend on i_j^{fr} rather than i_j.

Chapter 5

Proteus Resonances

The magnitudes of resonant kicks on orbital inclinations depended strongly on the mass of the perturber. Since Proteus is by far the largest satellite, resonances between it and the other satellites are much stronger than those among the three smaller satellites. As a first approximation, therefore, we examine only the Proteus resonances, neglect the weaker ones, and see if we can form a consistent story from this subset of Fig. 3.3. We will return to consider resonances between Larissa, Galatea, and Despina in Section 6.1. In addition to the very recent 2:1 resonant zone between Proteus and Larissa, Proteus might have gone through seven other resonant zones that we list backwards from the present: *PD 3:1*, *PG 2:1*, *PL 5:3*, *PL 3:2*, *PD 2:1*, *PG 5:3*, and *PL 7:5*. In this chapter, we detail these resonance passages, determine the inclination excitation provided by each resonance, and analyze new features found in our simulations.

5.1 The Recent 2:1 Proteus-Larissa Resonance Passage

The 2:1 mean-motion resonance between Proteus and Larissa (*PL 2:1*) is located only about 900 km inside Proteus' current orbit or 600 km outside Larissa's, implying that the satellites passed through the resonance in the recent past (a few hundred million

years ago). The proximity of this resonance suggests a resonant origin for the larger-than-average eccentricities of these two satellites (Table 3.1). In Fig. 5.1, we simulate the passage of Proteus and Larissa through this resonance at roughly the correct tidal migration rate. As our first step in the investigation, Triton has been excluded from the system so that a typical two-body resonance passage can be observed. We plot the orbital semi-major axes, eccentricities, and inclinations of Proteus and Larissa as the satellites diverge slowly through the resonant zone. The orbital elements of the two moons jump at several locations where different individual resonances occur. We name the resonances after the orbital elements they affect with a capital R to signify the appropriate term in the disturbing function (Murray and Dermott, 1999, §6.9), and mark all of the 1st- and 2nd-order ones in Fig. 5.1. Depending on which orbital elements are most strongly affected, the resonances can be classified as eccentricity-type, inclination-type, or mixed-type.

5.1.1 Eccentricity Evolution during and after the *PL 2:1* Passage

The eccentricities of the two satellites are shown in the middle panels of Fig. 5.1. The two first-order eccentricity-type resonances, R_{e_L} and R_{e_P}, dominate the satellites' eccentricity growth. Second-order resonances $R_{e_L^2}$ and $R_{e_P^2}$ occur at exactly the same locations, respectively, while $R_{e_L e_P}$ falls between the two. Larissa's semi-major axis drops while that of Proteus grows with each eccentricity kick to conserve the energy and angular momentum of the system. If a_L is not significantly altered by the resonances, then $R_{e_L e_P}$ would be midway between $R_{e_L^2}$ and $R_{e_P^2}$; we derive a similar
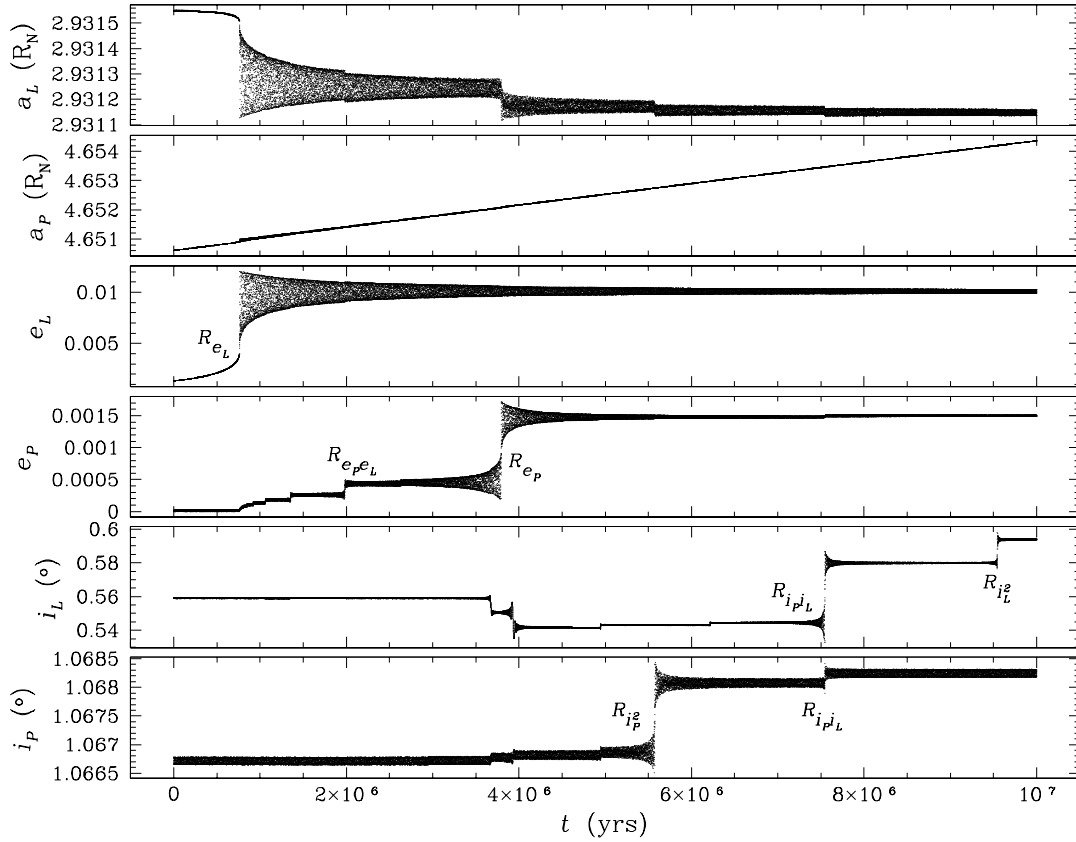
Figure 5.1: Proteus and Larissa diverge through *PL 2:1*. Triton is excluded from this system. Plots show the semi-major axes, eccentricities, and inclinations of the two small satellites. Larissa has a fixed semi-major axis at $a_L = 2.93 R_N$, and Proteus migrates outward with a rate of $3.6 \times 10^{-10} R_N/yr$. As only the relative divergence rate is important in most cases, it is an excellent approximation to move Proteus alone. We assume satellite densities $\bar{\rho} = 0.8 \, g/cm^3$. Both satellites begin on circular orbits with inclinations of $0.5590°$ and $1.0667°$ measured relative to the invariable plane, respectively. These inclinations are the same as would be forced by Triton were it included in the system. Orbital element kicks due to first- and second-order resonances are marked in the plots. The unmarked small kicks are due to higher-order resonances.
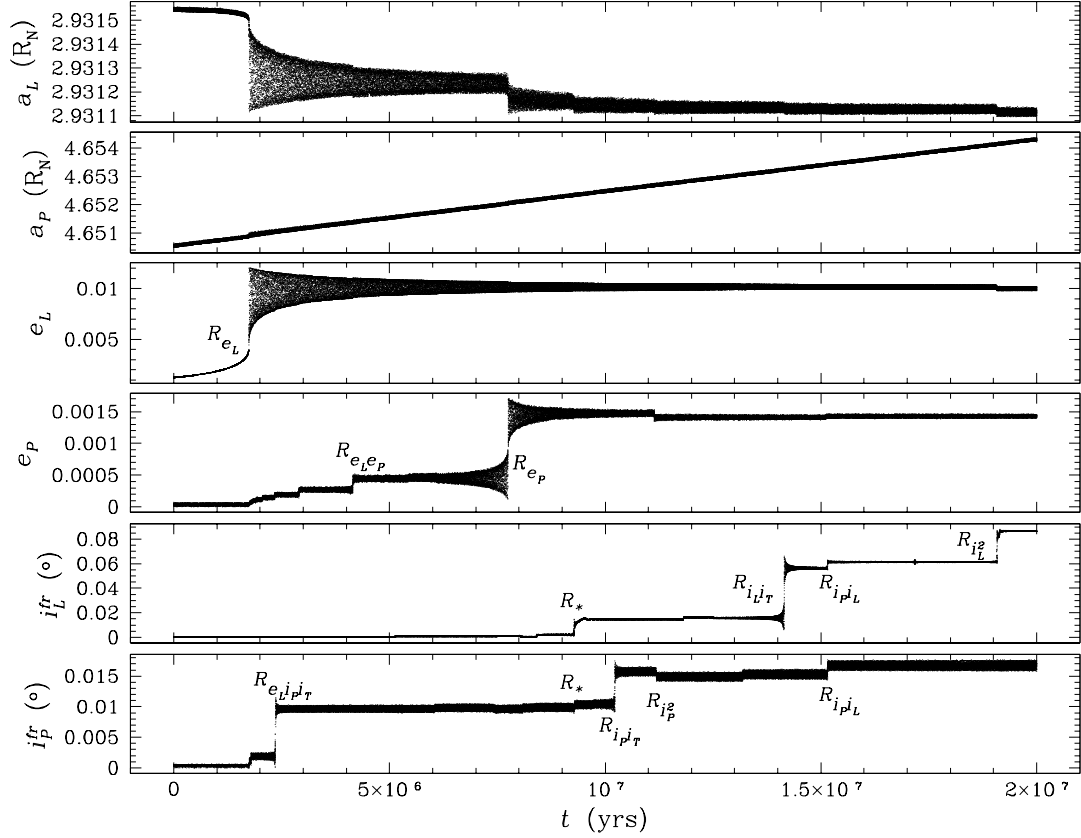
Figure 5.2: Proteus and Larissa diverge through *PL 2:1*. The system consists of Neptune, Triton, and the two small satellites. Plots show the semi-major axes, eccentricities, and free inclinations (measured relative to the Laplace plane) of Proteus and Larissa. Larissa's semi-major axis a_L is fixed at $2.93\,R_N$, while Proteus migrates outward with $\dot{a}_P = 1.8 \times 10^{-10}\,R_N/yr$. The density of the satellites is $\bar{\rho} = 0.8\,g/cm^3$. The first- and second-order resonances are identified, including a few strong three-body resonances ($R_{e_L i_P i_T}$, R_*, $R_{i_P i_T}$, and $R_{i_L i_T}$); smaller kicks are due to higher-order resonances.

result in Section 5.1.2 for the inclination-type resonances.

The amplitudes of resonant kicks depend on the strengths of the resonant perturbations, which are functions of satellite masses and the instantaneous values of the orbital elements. Since the mass of Proteus is about 10 times Larissa's, a given resonance (e.g., $R_{e_P e_L}$) gives a stronger kick to Larissa than to Proteus. The strength of the second-order resonance $R_{e_L e_P}$ depends on two small eccentricities, so it is much weaker than the first-order resonances and contributes only about 1/6 of the growth of e_P. The tiny kicks to e_P before $R_{e_P e_L}$ in Fig. 5.1 are due to higher-order resonances.

Our additional simulations with different tidal migration rates suggest that the tidal migration rate is slow enough that the first- and second-order resonances are traversed in the adiabatic limit. Higher-order resonances are not traversed adiabatically, so their eccentricity and inclination kicks depend on the drag rate and are difficult to predict. For the 2:1 passage, though, higher-order resonances are weaker by about an order of magnitude and their contributions are minimal (Fig. 5.1). We do not include Triton in our eccentricity studies since its orbit is nearly circular and its perturbation to the small satellites' eccentricities is minimal. We verify this assertion with a direct comparison between simulations with and without the large moon (Figs. 5.1 and 5.2).

The masses of Proteus and Larissa are not well-constrained observationally. The higher the masses, the stronger the resonances, and in turn, the larger the eccentricity excitation. Since the small satellites formed from the same circum-Neptunian debris disk, we might expect that they should have similar compositions and densities. We make the simple assumption that both satellites have the same density, and calculate

their masses based on their observed sizes. In the simulation shown in Fig. 5.1, we use a mean density of $\bar{\rho} = 0.8\,g/cm^3$. The satellites might have a higher or lower density, depending on their composition and porosity. The current eccentricities of the two satellites, 0.00053 for Proteus and 0.00139 for Larissa, place a lower limit on the resonant excitation, which then limits the minimum density of the two satellites. We simulate the resonance passage with a number of different assumed mean densities for Proteus and Larissa. These simulations show $\bar{\rho} > 0.05\,g/cm^3$ in order for Proteus to acquire an eccentricity $e_P > 0.00053$. With this density, Larissa's eccentricity is excited to a value significantly higher than its current 0.00139. A density of $\bar{\rho} > 0.05\,g/cm^3$ for satellites is not particularly a good constraint, but we will derive much better limits after later inclination studies.

After the resonance, the satellite orbits must migrate outward while simultaneously circularizing. If we know the eccentricities of the satellites immediately after the resonance, this provides a constraint on the satellite Q's, which we now explore. Since tidal migration is determined by planetary tides (Eq. 3.1) and eccentricity damping is mostly accounted for by satellite tides (Eq. 2.28), the ratio between a satellite's Q_s and Neptune's Q_N can be estimated based on the satellite's migration distance and the change of its eccentricity subsequent to the resonant passage:

$$\frac{Q_s}{Q_N} = \frac{21}{4} \frac{1}{k_{2N}\tilde{\mu}_s} \left(\frac{\rho_N}{\rho_s}\right)^2 \left(\frac{R_N}{R_s}\right) \left|\frac{\ln(a_f/a_i)}{\ln(e_f/e_i)}\right|, \tag{5.1}$$

where ρ_N and ρ_s are the densities of Neptune and the small satellite; the subscripts "i" and "f" indicate initial and final values of the semi-major axis and eccentricity, respectively. We defer the estimation of Q_s to Section 6.3 after we have obtained

better constraints on Q_N.

5.1.2 Inclination Resonances in the *PL 2:1* Resonant Zone

In addition to the eccentricities of the Proteus and Larissa, Fig. 5.1 also shows the change of the satellite inclinations in the bottom two panels. First-order inclination-type resonances do not exist due to the constraints on resonant arguments (Eqs. 2.13 and 2.14, Hamilton, 1994). The three second-order inclination resonances, $R_{i_P^2}$, $R_{i_P i_L}$, and $R_{i_L^2}$, are equally-spaced in time, which can be explained by considering the corresponding resonant arguments:

$$\phi'_{i_P^2} = 4\lambda_{P1} - 2\lambda_L - 2\Omega_{P1}, \tag{5.2}$$

$$\phi'_{i_P i_L} = 4\lambda_{P2} - 2\lambda_L - \Omega_L - \Omega_{P2}, \tag{5.3}$$

$$\phi'_{i_L^2} = 4\lambda_{P3} - 2\lambda_L - 2\Omega_L, \tag{5.4}$$

where the subscripts, 1, 2, and 3, denote the three different locations of Proteus. We use ϕ' instead of ϕ here to distinguish these arguments from the new definitions to be introduced later in this section. Since the three resonant locations are very close, we can safely neglect the difference between $\dot{\Omega}_{P1}$ and $\dot{\Omega}_{P2}$. Applying Eq. (2.19) and subtracting pairs of equations yield

$$n_{P1} - n_{P2} \approx n_{P2} - n_{P3},$$

which, for closely-spaced resonances, is equivalent to

$$a_{P2} - a_{P1} \approx a_{P3} - a_{P2}.$$
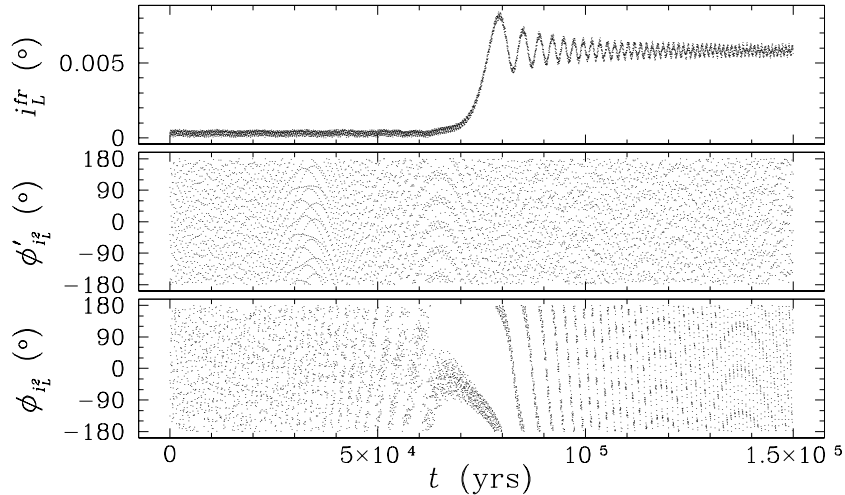
Figure 5.3: $R_{i_L^2}$ transit during the *PL 2:1* resonance passage and the corresponding resonant angles. Top: the free inclination of Larissa; middle: the traditionally-defined resonant argument $\phi'_{i_L^2} = 4\lambda_P - 2\lambda_L - 2\Omega_L$; bottom: resonant argument with new definition $\phi_{i_L^2} = 4\lambda_P - 2\lambda_L - 2\tilde{\Omega}_L$. In the Neptune-Triton system, $\phi'_{i_L^2}$ fails to librate in the vicinity of resonance; instead, $\phi_{i_L^2}$ is the true resonant argument.

Furthermore, since the migration rate of Proteus is nearly constant during the resonance passage, these locations are equally spaced in time as well (Fig. 5.1).

We continue our investigation by running a simulation that includes Triton (Fig. 5.2). Compared to Fig. 5.1, the eccentricity histories in this simulation show similar features, with only a few very weak additional kicks arising from high-order, mixed-type resonances. This justifies our neglect of Triton in the previous section. In addition, the tidal migration rate used in Fig. 5.2 is half of that of Fig. 5.1, which demonstrates that the strong resonances of this resonant passage are traversed in the adiabatic limit.

The inclinations shown in Fig. 5.2 are free inclinations with superscript "*fr*", which are defined in Chapter 4 and directly comparable to those listed in Table 3.1.

The pattern of inclination kicks is quite different from what is shown in Fig. 5.1. We identify the three traditional second-order inclination-type resonances ($R_{i_P^2}$, $R_{i_P i_L}$, and $R_{i_L^2}$) by their positions and spacing (compare with Fig. 5.1). In addition, there are several new and stronger resonances that appear near the standard ones. Evidently, Triton has a significant impact on the tilts of the small satellites' orbits. Its secular perturbation slightly augments the moonlets' orbital precession rates, but more importantly, it alters the inclination resonant pattern itself.

When two satellites pass through a mean-motion resonance, the corresponding resonant argument has a stationary value at the exact resonant location (Eq. 2.19). In our simulations with Triton, however, we notice that the resonant angles of the three second-order inclination-type resonances, as defined by the standard Eqs. (5.2-5.4), are not stationary even when the resonant kicks occur. For example, Fig. 5.3 shows the inclination of Larissa during the $R_{i_L^2}$ traverse. The traditional resonant angle $\phi'_{i_L^2}$ is plotted in the middle panel, which shows no sign of libration. This problem motivated our theoretical consideration of new orbital elements in Chapter 4. With the mathematical results therein, we now generalize the resonant argument (Eq. 2.18) to

$$\phi = (p+q)\lambda_2 - p\lambda_1 + j_3\tilde{\varpi}_1 + j_4\tilde{\varpi}_2 + j_5\tilde{\Omega}_1 + j_6\tilde{\Omega}_2 + j_T\Omega_T \qquad (5.5)$$

for the Neptune-Triton system. The new resonant angles have stationary values at the exact resonant location (bottom panel in Fig. 5.3), supporting our arguments. Note that in Eq. 5.5, we also include Triton's node to cover three-body resonances in this system, as discussed in next section. Accordingly, the second d'Alembert condition

60

Eq. (2.14) should be changed to

$$j_5 + j_6 + j_T = \text{even number.}$$

5.1.2.1   Three-Body Resonances

In a two-satellite system, the inclination evolution during the 2:1 resonance passage is dominated by three equally-spaced, second-order resonances: $R_{i_L^2}$, $R_{i_L i_P}$ and $R_{i_P^2}$ (Fig. 5.1). In the actual Neptunian system with Triton included, however, several stronger kicks appear near the traditional second-order kicks (Fig. 5.2) What are these new resonances?

A careful examination of their resonant locations shows that the strongest kicks (labeled $R_{i_L i_T}$ and $R_{i_P i_T}$ in Fig. 5.2) are shifted the same distance to the left of $R_{i_P i_L}$ and $R_{i_P^2}$, respectively, which implies that the resonant arguments of the two new resonances, $\phi_{i_L i_T}$ and $\phi_{i_P i_T}$, can be derived by adding a common term to the corresponding second-order resonant arguments. Because $R_{i_L i_T}$ only affects Larissa and $R_{i_P i_T}$ only affects Proteus, $\tilde{\Omega}_L$ cannot appear in $\phi_{i_P i_T}$, and $\tilde{\Omega}_P$ not in $\phi_{i_L i_T}$. The locations of the new kicks thus suggest the following resonant arguments:

$$\phi_{i_L i_T} = 4\lambda_P - 2\lambda_L - \tilde{\Omega}_L - \Omega_T, \tag{5.6}$$

$$\phi_{i_P i_T} = 4\lambda_P - 2\lambda_L - \tilde{\Omega}_P - \Omega_T, \tag{5.7}$$

which we verify by noticing their forced librations (Fig. 5.4) immediately prior to the resonant kicks. The node of the Laplace plane appears in both arguments through Ω_T, which means that the resonances can be considered to be amongst Proteus,

61
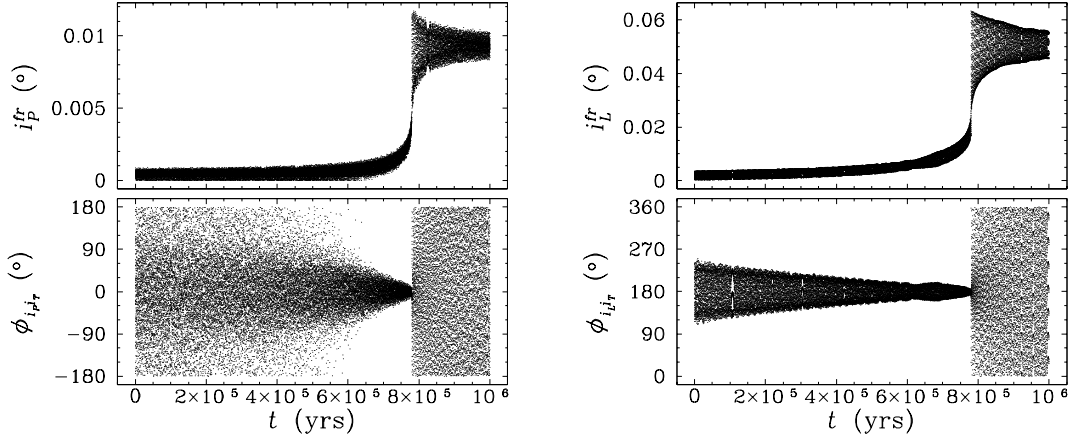
Figure 5.4: Resonant arguments ($\phi_{i_P i_T}$ and $\phi_{i_L i_T}$) of the three-body resonances $R_{i_P i_T}$ and $R_{i_L i_T}$. The top panels show the free inclinations of Proteus (i_P^{fr}) and Larissa (i_L^{fr}) as they traverse the two resonances; the bottom panels show the corresponding resonant arguments from Eqs. (5.6-5.7). These simulations use similar parameters as in Fig. 5.2, except that Proteus migrates at a slower rate ($3.6 \times 10^{-11} R_N/yr$).

Larissa and the warped rotating plane. When the system is close to $R_{i_L i_T}$ and $R_{i_P i_T}$, the associated angles $\phi_{i_L i_T}$ and $\phi_{i_P i_T}$ begin to oscillate around equilibrium points at 180° and 0°, respectively. The libration amplitude decreases and the affected inclination rises as each resonance is approached. When the resonance is crossed, the free inclination of the affected satellite is kicked up sharply and the corresponding semi-major-axis jump brings the two out of resonance. The resonant angle ceases to librate and begins to circulate again.

Since the Laplace plane is only a mathematical description of Triton's secular effects, these new resonances can also be interpreted as three-body resonances among Proteus, Larissa, and Triton, which is why we use Ω_T rather than Ω^{Lap} in Eqs. (5.6-5.7). Three-body resonances are usually weaker than two-body ones because the involvement of Triton as a resonant perturber introduces an extra factor of m_T/m_N

in the expression for resonant strengths. However, this effect is counter-balanced by Triton's large orbital tilt. Specifically, the strengths of the three-body resonant kicks on Proteus and Larissa scale as:

$$R_{i_P i_T} \quad \propto \quad \frac{m_T}{m_N} \frac{m_L}{m_N} \sin i_P^{fr} \sin i_T, \tag{5.8}$$

$$R_{i_L i_T} \quad \propto \quad \frac{m_T}{m_N} \frac{m_P}{m_N} \sin i_L^{fr} \sin i_T, \tag{5.9}$$

while those of the respective two-body resonances obey

$$R_{i_P^2} \quad \propto \quad \frac{m_L}{m_N} \sin^2 i_P^{fr},$$

$$R_{i_L i_P} \quad \propto \quad \frac{m_P}{m_N} \sin i_L^{fr} \sin i_P^{fr}.$$

The first pair differ from the second only by a factor of

$$\frac{m_T}{m_N} \frac{\sin i_T}{\sin i_P^{fr}} \approx 0.2,$$

implying comparable resonant kicks. Note that this is only a rough estimate, the exact ratio between the strengths of the resonances also depends on the numeric coefficient in each resonant term.

This type of resonance is different from previously-studied three-body resonances (e.g., the Laplace resonance among the three Jovian satellites: Io, Europa, and Ganymede) in that the third body's orbital longitude does not appear in the resonant arguments. Nevertheless, Triton's node is involved in both arguments, implying that its inclination should also be kicked during resonance crossing. This effect is, however, extremely weak due to Triton's huge mass. Since resonant locations are mostly determined by the coefficients of the orbital longitudes appearing in the resonant angles, the new resonances are located close to the standard two-body resonances.

In general, the resonant argument of a three-body resonance has the form

$$\phi = p_1\lambda_1 + p_2\lambda_2 + p_3\lambda_3 + j_1\Omega_1 + j_2\Omega_2 + j_3\Omega_3 + j_4\varpi_1 + j_5\varpi_2 + j_6\varpi_3,$$

where the integers p_i and j_i still need to satisfy the two d'Alembert constraints mentioned before. With different integer coefficients, three-body resonances should be thickly packed throughout the region of the inner satellites. In our simulations, however, we fail to locate any that involve the longitude of Triton (i.e., $p_3 \neq 0$), from which we conclude that these resonances are very weak. It is unclear why they are so weak since their strengths should scale similarly with satellite masses and inclinations as $R_{i_L i_T}$ and $R_{i_P i_T}$. A definitive explanation would require a Taylor expansion of a 3-body disturbing function similar to what has been done for two interacting satellites (Murray and Dermott, 1999, §6.4), and an examination of the relevant resonant terms. This, however, is a monumental undertaking beyond the scope of this dissertation.

5.1.2.2   Important Higher-order Resonances

By definition, $R_{i_L i_T}$ and $R_{i_P i_T}$ are second-order resonances since their strengths depend on inclinations of both Triton and a small satellite. Generally, however, "order" should refer to an expansion over small quantities. Since $\sin i_T$ is not small here, these three-body resonances (Eq. 5.8-5.9) should really be considered as first-order in inclinations. But they are much weaker than the first-order eccentricity resonances due to the extra dependence on m_T/m_N, and it is better to consider these resonances to be

second-order in the small quantities i_P^{fr}, i_L^{fr}, and m_T/m_N. We adopt this definition here.

In addition to the two second-order three-body resonant kicks, a few fairly strong higher-order kicks also contribute significantly to satellite inclination histories, two of which are identified in Fig. 5.2. The strong resonance $R_{e_L i_P i_T}$ occurs right after R_{e_L}, and has a resonant argument

$$\phi_{e_L i_P i_T} = 2\lambda_P - \lambda_L - \tilde{\varpi}_L - \tilde{\Omega}_P + \Omega_T.$$

It is a third-order resonance that affects the eccentricity of Larissa, the free inclination of Proteus, and the inclination of Triton. We expect the strength of this resonance to be of order $e_L \sim 0.01$ times the strength of the second-order $R_{i_P i_T}$, but simulations show that the two are comparable. Thus, $R_{e_L i_P i_T}$ must have a large numerical coefficient in its strength term that could be derived through Taylor expansion of the three-body disturbing function.

Another interesting resonance is marked as R_* in Fig. 5.2. It occurs almost exactly at the location where $2n_P - n_L = 0$. Since this resonance affects the inclinations of both satellites, both nodes, $\tilde{\Omega}_P$ and $\tilde{\Omega}_L$, should appear in the resonant argument. Nodal precession normally should displace the resonant location from the precise 2:1 commensurability. R_*, however, is not displaced, suggesting that the satellites' pericenters (ϖ_P and ϖ_L) must also be involved in the resonant argument. The pericenters are required to explain the lack of offset, since, to first-order in small eccentricities and inclinations, $\dot{\Omega}_P = -\dot{\varpi}_P$ and $\dot{\Omega}_L = -\dot{\varpi}_L$. A single resonance with all of these

properties would need to be at least fifth-order, e.g.,

$$\phi = 4\lambda_P - 2\lambda_L + \tilde{\varpi}_P + \tilde{\Omega}_P - \tilde{\varpi}_L - \tilde{\Omega}_L - 2\Omega_T.$$

This is surprising, as a fifth-order resonance should not be as strong as the second-order resonance $R_{i_P i_L}$ (Fig. 5.2). A careful examination of resonances in the vicinity of R_* reveals two pairs of third-order resonances:

$$\phi_{e_L i_L i_T^3} = 2\lambda_P - \lambda_L + \tilde{\varpi}_L + \tilde{\Omega}_L - 3\Omega_T;$$

$$\phi_{e_P i_P i_T^3} = 2\lambda_P - \lambda_L + \tilde{\varpi}_P + \tilde{\Omega}_P - 3\Omega_T;$$

and

$$\phi_{e_L i_L i_T} = 2\lambda_P - \lambda_L - \tilde{\varpi}_L - \tilde{\Omega}_L + \Omega_T;$$

$$\phi_{e_P i_P i_T} = 2\lambda_P - \lambda_L - \tilde{\varpi}_P - \tilde{\Omega}_P + \Omega_T.$$

Although each individual resonance affects the orbit of only one small satellite, the two resonances in either pair occur almost on top of each other, and the two pairs themselves are so close that we cannot resolve them in Fig. 5.2. The first pair is weaker than the latter pair by a factor of $\sim \sin^2 i_T \approx 0.15$, although the exact factor again depends on the numerical coefficients in their strength expressions.

A magnified look at R_* with a slower migration rate shows the slightly different locations of these four resonances (Fig. 5.5). The tiny offsets between the locations of the resonances in each pair are due to higher-order eccentricity and inclination effects on the nodal and pericenter precession rates. At the beginning of the simulation, $\phi_{e_L i_L i_T}$ shows large amplitude libration because $R_{e_L i_L i_T}$ is the strongest resonance
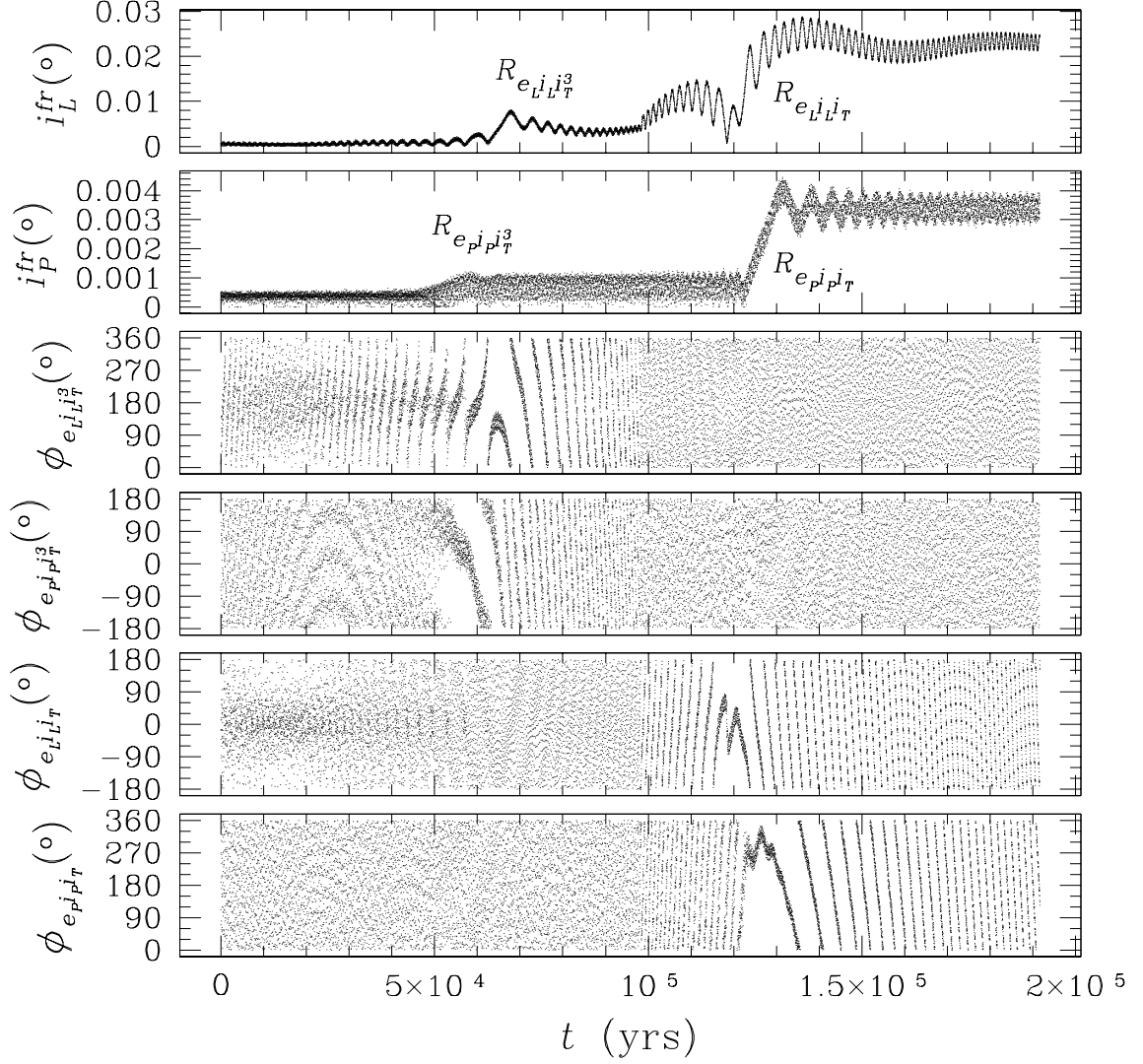
Figure 5.5: Detail of the R_* resonance in Fig. 5.2. Larissa's orbit is fixed at $2.931\,R_N$ and Proteus migrates outwards at $3.6 \times 10^{-11}\,R_N/yr$. Satellite densities are taken to be $0.8\,g/cm^3$. The simulation covers a very small vicinity around the location where $2n_P = n_L$, which occurs here at $t \sim 1.04 \times 10^5$ year. The plots show free inclinations of the two satellites, together with resonant arguments of four third-order resonances which are marked in the inclination plots and detailed in the text.
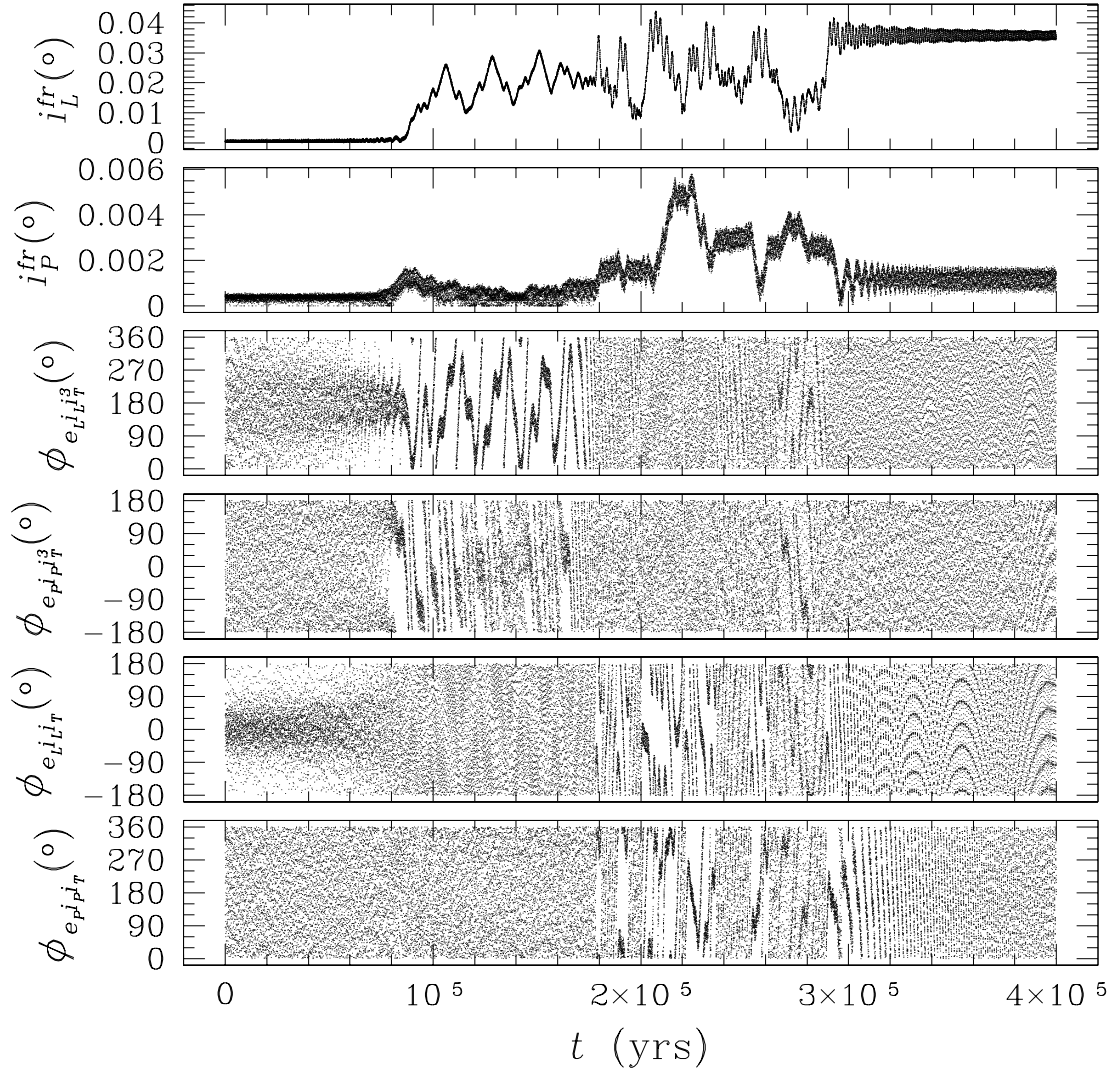
Figure 5.6: Similar simulation as shown in Fig. 5.5, but the satellites have a slightly higher density $\bar{\rho} = 1.0\,g/cm^3$. With a larger density, the resonances are stronger and the inclination excitations behave rather stochastically. The resonance angle plots show that multiple resonances are active simultaneously. The final inclinations are impossible to predict.

in the vicinity. However, the weaker resonances $R_{e_L i_L i_T^3}$ and $R_{e_P i_P i_T^3}$ are traversed first. As the orbits approach these two resonances, $\phi_{e_L i_L i_T}$ becomes out of phase for libration, and the arguments of two earlier resonances circulate even more slowly. At the resonant locations, these angles reverse their direction of circulation. The arguments of the latter pair of resonances behave similarly. Due to their weak resonance strengths, none of the four arguments strongly librates as shown for $R_{i_P i_T}$ and $R_{i_L i_T}$ in Fig. 5.4. The two Larissa resonances, which should be stronger due to higher values of e and i as well as $m_P > m_L$, display long-range effects visible as concentration in the resonant arguments around $t = 0$.

The overlap of these resonance effects is a recipe for chaos, especially if the resonances are a little bit stronger, e.g., with larger satellite masses, or if orbits linger in the region due to a slower Proteus migration rate. When two orbits diverge through an isolated resonance, the semi-major axis of the inner satellite decreases, while that of the outer satellite increases. The resulting jump causes the two orbits to diverge from each other more quickly than during tidal migration. If another resonance is in the immediate vicinity, however, the system can be affected by it before completely leaving the first resonance, resulting in stochastic behavior. In other words, all resonances have effective widths – near resonance effects emerge before, and continue after, the exact resonant location. Stronger resonances have broader widths. If two resonances are located very close to each other, and if they are strong enough that their widths overlap, temporary capture can occur and the kicks to orbital elements behave somewhat like a random walk. Fig. 5.6 shows the same resonances as Fig. 5.5

does, but with satellites just 25% more massive. As the system steps into the first pair of resonances, the two resonant angles start to librate. But the system does not exit the resonant region quickly and cleanly as in Fig. 5.5. Instead, the two resonant angles alternate between libration and circulation in a complicated way, and the inclinations are kicked up or down randomly until the system escapes these resonances. The second pair of resonances interacts chaotically in a similar manner. The random behavior of the inclinations throughout this region makes it impossible to predict their total excitation. However, given certain migration rates and low-enough satellite densities, these temporary captures only continue for a limited time. In the simulation shown in Fig. 5.6, the maximum inclination gains of Proteus and Larissa are of the same order as the $R_{i_P i_T}$ and $R_{i_L i_T}$ kicks. Similar chaotic interactions have also been noticed in simulations of the orbital resonances among the Uranian satellites by Tittemore and Wisdom (1988). The existence of these chaotic zones puts an intrinsic limit on how well the orbital histories of Neptune's small satellites can be reconstructed.

5.2   The Second-order Resonance *PD 3:1*

The previous resonant zone Proteus traversed consists of the 3:1 resonances with Despina (cf. Fig. 3.3). The 3:1 resonant zone is simpler than the 2:1 one as it contains only the second-order, fourth-order, and other even-order resonances. Compared to the *PL 2:1* zone (Fig. 5.2), which has first-order eccentricity resonances, there are not any strong eccentricity kicks and the lack of third-order resonances makes the
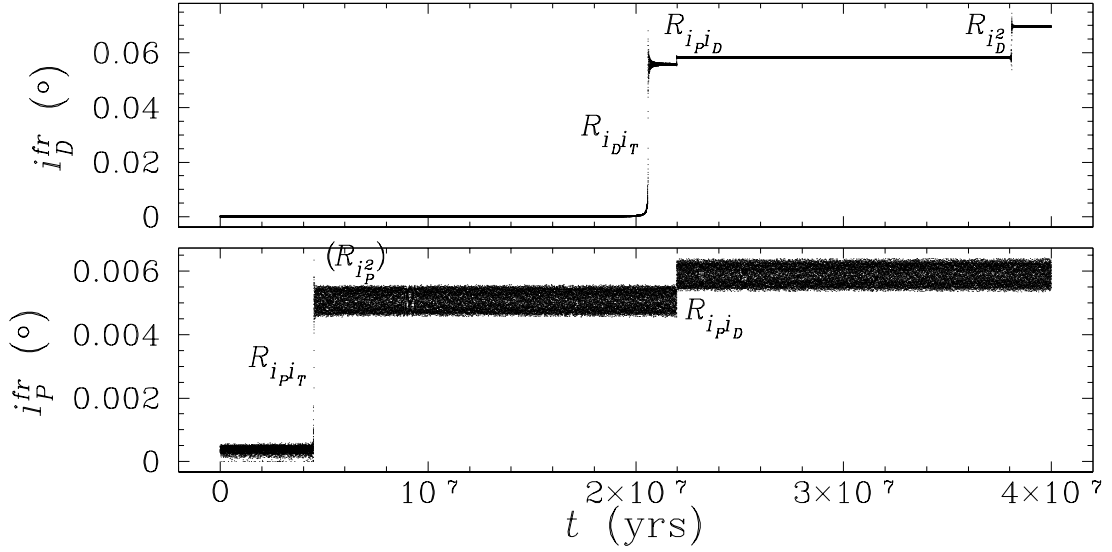
Figure 5.7: Proteus and Despina diverge through *PD 3:1*. The satellites have a density $\bar{\rho} = 0.8\,g/cm^3$, and $Q_N = 33,000$. Both satellites are initially on circular orbits in their local Laplace planes. Two of the three usual second-order resonances are identified ($R_{i_P i_D}$ and $R_{i_D^2}$), as well as the two three-body resonances, $R_{i_P i_T}$ and $R_{i_D i_T}$. Note that although the effects of the third second-order resonance $R_{i_P^2}$ is too weak to be visible, we indicate its approximate location.

inclination evolution much simpler and cleaner as well (Fig. 5.7). The two second-order three-body resonant kicks, $R_{i_P i_T}$ and $R_{i_L i_T}$, dominate the inclination growth. Two of the three traditional second-order two-body resonances can be easily identified, and fourth- and higher-order kicks are mostly too weak to have noticeable effects. The overall *PD 3:1* inclination kick on Despina is a little smaller than the overall *PL 2:1* kick on Larissa, and the Proteus kick through the *PD 3:1* is weaker by a factor of 3. This is due both to the smaller mass of Despina ($m_D \approx 0.5\,m_L$) and to the lack of contributions from odd-order resonances in the *PD 3:1*. The two sets of strong third-order three-body resonances ($R_{e_L i_P i_T}$ and R_*) that contributed significantly to the growth of i_P^{fr} do not exist in the *PL 3:1* and other second-order resonant zones,

71

including the *PL 5:3*, *PG 5:3* and *PL 7:5* from Fig. 3.3.

5.3   The *PG 2:1* and Diverging Capture

The 2:1 resonant zone between Proteus and Galatea is located between *PD 3:1* and *PL 5:3*. This resonance is similar to the first-order *PL 2:1* discussed above; the only differences come from the different mass ratios of the two satellite pairs and their different distances from Neptune. The two first-order eccentricity resonances (R_{e_G} and R_{e_P}) kick the orbital eccentricities of the two satellites strongly, as can be seen in Fig. 5.8. The inclination kicks due to three-body resonances ($R_{i_P i_T}$, $R_{i_G i_T}$, $R_{e_G i_P i_T}$, and R_*) are similar in magnitude to those due to the *PL 2:1* resonances discussed in Section 5.1. In a small fraction of our simulations such as the one shown in Fig. 5.8, however, we see a new effect that is surprising at first glance: resonance capture.

In addition to resonant kicks when satellite orbits are subject to sudden and sharp changes, two satellites may also be captured into a mean-motion resonance during tidal migration (Greenberg, 1977). When this occurs, the mean motions and orbital precession rates of the two satellites vary in such a way that the associated resonant angle librates around a stationary point rather than cycling through full 360° rotations. The affected eccentricity or inclination grows until nearby resonances or other perturbations break the system out of resonance. What is surprising is that previous studies have shown that resonant captures during tidal migration occur when the orbits of two satellites approach each other (e.g. Hamilton, 1994), while our satellites are diverging. Earlier papers, however, all focus on strong first- and second-

72
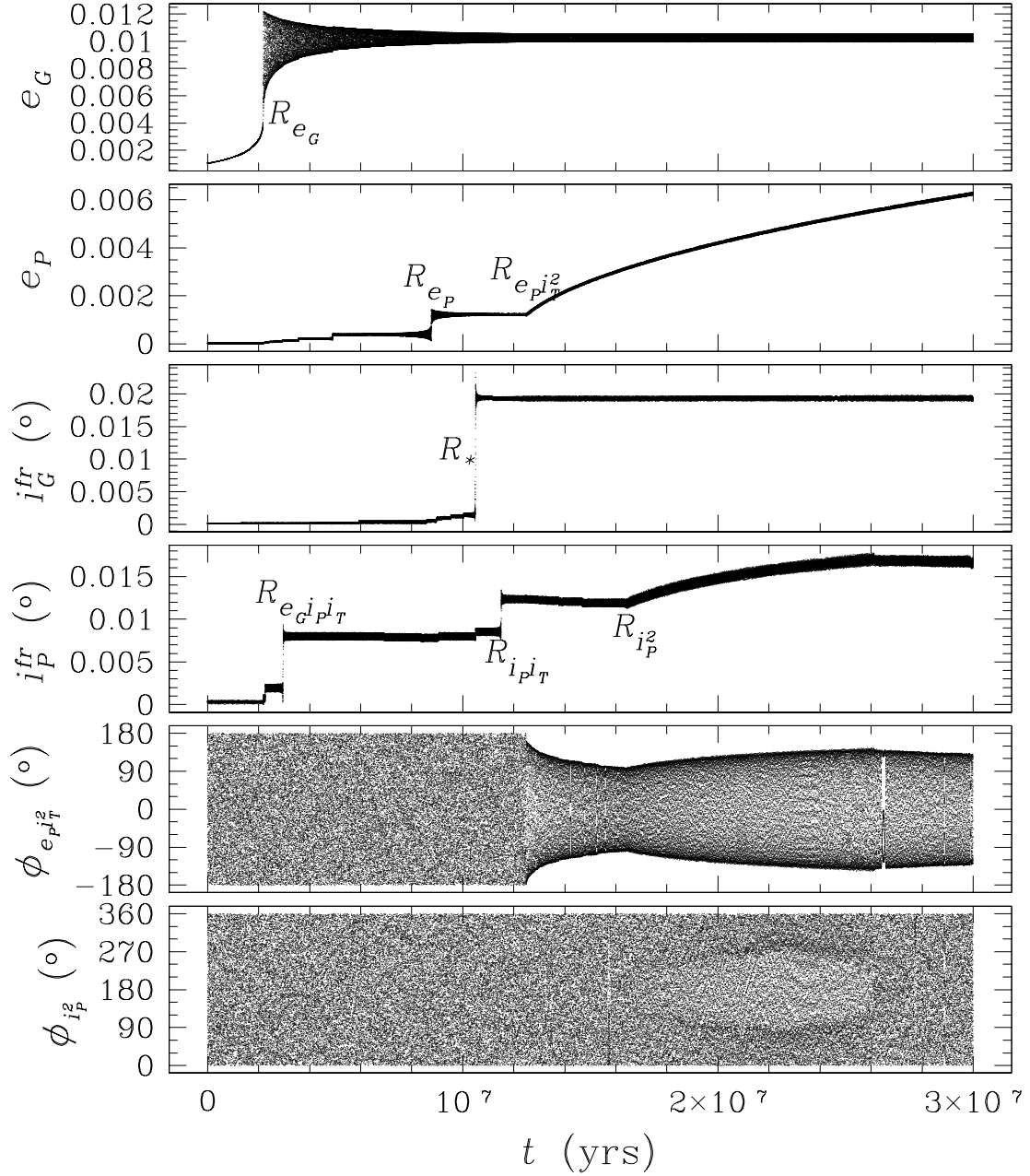
Figure 5.8: The *PG 2:1* passage with an isolated eccentricity-type resonance capture. After being captured into the $R_{e_P i_T^2}$ resonance, Proteus is later captured into the second-order resonance $(R_{i_P^2})$ which affects its inclination. The second capture is enabled by extremely slow changes to $\dot{\bar{\varpi}}_P$ and $\dot{\bar{\Omega}}_P$ induced by the first resonance. In this simulation $\bar{\rho} = 0.8\,g/cm^3$ and $Q_N = 22,000$.

order resonances. For some higher-order resonances, temporary capture is possible for diverging orbits. We have found several such resonant trappings in our simulations when the two orbits diverge slowly enough. Nevertheless, trappings are still very rare even at slow migration rates, probably because of the inherent weakness of higher-order resonances. We have run 10 simulations through the *PG 2:1* zone with $\frac{Q_N}{\bar{\rho}/(g/cm^3)}$ ranging between 25,000 and 35,000 for different satellite densities ranging between $0.4\,g/cm^3$ and $1.5\,g/cm^3$, but there is only one capture event at $\bar{\rho} = 0.8\,g/cm^3$, shown in Fig. 5.8. In this simulation, after the system has gone through the two first-order eccentricity resonances (R_{e_G} and R_{e_P}), the two third-order three-body resonances ($R_{e_G i_P i_T}$ and R_*), and the first second-order three-body resonance ($R_{i_P i_T}$), the two orbits are captured into a three-body resonance $R_{e_P i_T^2}$, second-order in the small quantities e_P and μ_T, with a critical argument

$$\phi_{e_P i_T^2} = 2\lambda_P - \lambda_G + \tilde{\omega}_P - 2\Omega_T. \tag{5.10}$$

5.3.1   Resonant Trapping Condition

We now derive the condition in which resonant trapping into $R_{e_P i_T^2}$ is possible. We assume that away from resonance, tides force Proteus and Galatea to migrate at rates $\dot{a}_P^d$ and $\dot{a}_G^d$, respectively, and that Triton's orbit is fixed in space. Following Hamilton (1994), we derive the rates of change of a_P, a_G, e_P, and i_T due to resonant and tidal

perturbations to the lowest order in e and i:

$$\dot{a}_P = \dot{a}_P^d - \frac{4\mu_G\mu_T\beta\, e_P\, i_T^2}{n_P\, a_P}\sin\phi_{e_P i_T^2}, \tag{5.11}$$

$$\dot{a}_G = \dot{a}_G^d + \frac{2\mu_P\mu_T\beta\, e_P\, i_T^2}{n_G\, a_G}\sin\phi_{e_P i_T^2}, \tag{5.12}$$

$$\dot{e}_P = \frac{\mu_G\mu_T\beta\, i_T^2}{n_P\, a_P^2}\sin\phi_{e_P i_T^2}, \tag{5.13}$$

$$\dot{i}_T = -\frac{2\mu_G\mu_P\beta\, e_P\, i_T}{n_T\, a_T^2}\sin\phi_{e_P i_T^2}. \tag{5.14}$$

Here β is the resonant strength of $R_{e_P i_T^2}$. It has the same units as $n^2 a^2$ and depends only on satellite semi-major axes. When the two orbits are in any of the 2:1 resonances, their semi-major axes must follow

$$\frac{a_P}{a_G} = \frac{\dot{a}_P}{\dot{a}_G} \approx 2^{\frac{2}{3}}. \tag{5.15}$$

With Eqs. (5.11, 5.12), and Eq. (5.15), we can solve for $\sin\phi_{e_P i_T^2}$ at resonant equilibrium:

$$\sin\phi_{e_P i_T^2} = \frac{n_P\, a_P^2}{2\mu_G\mu_T\beta e_P i_T^2}\frac{\dot{a}_P^d/a_P - \dot{a}_G^d/a_G}{2 + \sqrt[3]{2}\mu_P/\mu_G}. \tag{5.16}$$

For $\dot{a}_P^d = \dot{a}_G^d = 0$, the two equilibrium points are at $\phi_{e_P i_T^2} = 0$ and $\phi_{e_P i_T^2} = 180°$. They are shifted slightly when dissipation is present.

Substituting Eq. (5.16) into Eq. (5.13), we obtain

$$2\, e_P\, \dot{e}_P = \frac{\dot{a}_P^d/a_P - \dot{a}_G^d/a_G}{2 + \sqrt[3]{2}\mu_P/\mu_G},$$

which has the solution

$$e_P = \left[e_{P0}^2 + \frac{\dot{a}_P^d/a_P - \dot{a}_G^d/a_G}{2 + \sqrt[3]{2}\mu_P/\mu_G}\, t \right]^{\frac{1}{2}}, \tag{5.17}$$

75

where t is the time elapsed since entering the resonance, and e_{P0} is the initial eccentricity of Proteus. If resonant trapping occurs for a low eccentricity, e_P must increase with time and Eq. (5.17) thus requires

$$\frac{\dot{a}_P^d}{a_P} - \frac{\dot{a}_G^d}{a_G} > 0,$$

or that the two orbits diverge from each other. Note that this is opposite the usual requirement that the orbits converge for trapping to be possible, yet consistent with the behavior of Fig. 5.8. This interesting result – trapping for diverging orbits – is a direct consequence of the sign of the $\tilde{\varpi}$ term in the resonant angle (Eq. 5.10), as we shall see below.

The resonance $R_{e_P i_T^2}$ affects not only the eccentricity of Proteus, but also the inclination of Triton. We can solve for the evolution of i_T with Eqs. (5.14) and (5.16):

$$i_T = \left[i_{T0}^2 - \frac{2\,\mu_P}{\mu_T}\sqrt{\frac{a_P}{a_T}}\left(\frac{\dot{a}_P^d/a_P - \dot{a}_G^d/a_G}{2 + \sqrt[3]{2}\mu_P/\mu_G}\right)\right]^{\frac{1}{2}}, \qquad (5.18)$$

where the second term on the right hand side is negative for trapping. Thus, if resonant trapping occurs, e_P increases with time while i_T decreases. In typical cases when the satellites have comparable masses, the trapping will cease when i_T drops to zero. Because of Triton's huge mass, however, the change of i_T is negligible compared to that of e_P:

$$\frac{\Delta i_T}{\Delta e_P} \sim -\frac{2\,\mu_P}{\mu_T}\sqrt{\frac{a_P}{a_T}} \approx 0.002.$$

Hence, Triton's inclination decreases ~ 500 times more slowly than Proteus' eccentricity increases and the resonance trapping is stable for a long time.

76

The resonant trapping condition can be easily generalized for an arbitrary resonance with an argument defined by Eq. (5.5). Following similar procedures, we find that, in order for any relevant eccentricity or inclination to increase, the integer in front of the corresponding node or pericenter angle in Eq. (5.5), j_i, must obey

$$j_i \left(\frac{\dot{a}_2^d}{a_2} - \frac{\dot{a}_1^d}{a_1} \right) > 0, \tag{5.19}$$

For standard first-order ($q = 1$) and second-order ($q = 2$) two-body resonances, j_i must be negative, and thus we recover the standard result: resonant trapping is possible only if $\dot{a}_2^d/a_2 - \dot{a}_1^d/a_1 < 0$, i.e., for converging orbits. But for resonances with three or more node and pericenter angles involved, like $R_{e_P i_T^2}$ shown in Eq. (5.10), some of the j_i can be positive, which makes capture into these resonances possible only for diverging orbits, as we have seen in Fig. 5.8. Thus for any isolated mean-motion resonances, capture for converging orbits requires a negative node or pericenter coefficient. For capture from diverging orbits, a positive coefficient is needed.

5.3.2 Evolution in $R_{e_P i_T^2}$

We now look at the resonant angle during the resonant trapping (the fifth panel of Fig. 5.8). Assuming moderate eccentricities so that the pericenter term in Eq. (5.10) is negligible, $\phi_{e_P i_T^2}$ satisfies

$$\ddot{\phi}_{e_P i_T^2} = 2\dot{n}_P - \dot{n}_G,$$

which can be easily transformed into a harmonic equation using Eqs. (5.11) and (5.12):

$$\ddot{\phi}_{e_P i_T^2} = \omega_0^2 \sin \phi_{e_P i_T^2} - (\dot{n}_G^d - 2\dot{n}_P^d), \tag{5.20}$$

where $\dot{n}_P^d = -(3/2)n_P\,\dot{a}_P^d/a_P$ and $\dot{n}_G^d = -(3/2)n_G\,\dot{a}_G^d/a_G$ are the tidal drag rates of the two orbits expressed in terms of mean motions. Eq. (5.20) is a standard harmonic oscillator with a libration frequency

$$\omega_0^2 = \frac{6\mu_T\beta\,e_P i_T^2}{a_P^2}\left(2\mu_G + \sqrt[3]{2}\mu_P\right).$$

As shown in Fig. 5.8, $\phi_{e_P i_T^2}$ begins to librate around a stable equilibrium point at $0°$ as the orbits are first trapped into the $R_{e_P i_T^2}$ resonance. In fact, the divergence forced by tidal dissipation causes the equilibrium point to shift to a small positive value determined by Eq. (5.16). Averaging over a libration, Eqs. (5.11) and (5.12) simplify to

$$\dot{a}_P = \dot{a}_P^d - \delta_P,$$

$$\dot{a}_G = \dot{a}_G^d - \delta_G,$$

where δ_P and δ_G are small positive quantities. These terms resist the tidal divergence and allow the approximate resonance condition (Eq. 5.15) to be maintained. The libration of $\phi_{e_P i_T^2}$ continues to decrease as exact resonance is approached.

For slow changes of ω_0, the system has an adiabatic invariant (Landau and Lifshitz, 1976, §49)

$$\omega_0 \cos\Phi = \texttt{constant},$$

where Φ is the libration width, or the amplitude of the oscillating resonant angle $\phi_{e_P i_T^2}$. As e_P increases slowly, ω_0 grows and the libration width decreases as shown in Fig. 5.8 from 1.2×10^7 years until 1.6×10^7 years when a second resonance is activated.

5.3.3 Trapping into $R_{i_P^2}$

Shortly after capture into $R_{e_P i_T^2}$, the two satellites are trapped into the traditional two-body resonance $R_{i_P^2}$ (Fig. 5.8), with a resonant argument

$$\phi_{i_P^2} = 4\lambda_P - 2\lambda_G - 2\tilde{\Omega}_P.$$

The interplay between the two active resonances is quite interesting. With both resonances active, the orbits still appear to diverge, as can be seen from Eq. (5.17) and the fact that e_P continues to rise in Fig. 5.8. But, coincident with the second capture, there is an abrupt change in the behavior of $\phi_{e_P i_T^2}$ (fifth panel of Fig. 5.8) whose libration changes from decreasing with time (as expected for an isolated resonance) to increasing with time. This state of affairs continues until $t = 2.6 \times 10^7$ years at which point the second resonance ceases to be active (note the flattening of the i_P curve) and the libration amplitude of $\phi_{e_P i_T^2}$ begins decreasing again.

The sharp-eyed reader might have noticed a very subtle change in the density of points for the $\phi_{i_P^2}$ history (sixth panel of Fig. 5.8) - an oval-shaped feature between $t = 1.6 \times 10^7$ and 2.6×10^7 years that indicates that the $R_{i_P^2}$ resonance is active. The oval feature has dark edges (turning points - note the similar dark edges in the fifth panel) and a lighter center because the system spends more time near $\phi_{i_P^2} = 0$ than near $\phi_{i_P^2} = 180°$. The $R_{i_P^2}$ resonance is prevented from cleanly librating about $\phi_{i_P^2} = 0$ by the more powerful $R_{e_G i_T^2}$ resonance, but the asymmetry in the density of points that it produces is enough to cause the systematic rise in Proteus' free inclination (Fig. 5.8, fourth panel). The libration of the resonant angle $\phi_{i_P^2}$ initially decreases

(from 1.6×10^7 yr $< t < 2.2 \times 10^7$ yr) and then increases again (from 2.2×10^7 yr

$< t < 2.6 \times 10^7$ yr) until orbit finally exits the $R_{i_P^2}$ resonance.

The $R_{i_P^2}$ resonance usually requires converging orbits to trap into the stable equi-

librium point $\phi_{i_P^2} \approx 180°$ (Murray and Dermott, 1999). With the diverging orbits

of Fig. 5.8, however, we see trapping favoring the $\phi_{i_P^2} \approx 0°$ equilibrium point. Evi-

dently the drag force and the strong earlier resonance combine to make the $\phi_{i_P^2} \approx 0°$

equilibrium point stable when it is normally unstable (Murray and Dermott, 1999);

this unusual circumstance allows i_P to grow in a second-order resonance despite the

diverging orbits.

We can qualitatively account for the effects of one resonance on another by extend-

ing Eq. (5.20) and the equivalent expression for $\ddot{\phi}_{i_P^2}$ to include both perturbations:

$$\ddot{\phi}_{e_P i_T^2} = \omega_0^2 \sin \phi_{e_P i_T^2} + \omega_1^2 \sin \phi_{i_P^2} - (\dot{n}_G^d - 2\dot{n}_P^d), \tag{5.21}$$

$$\frac{\ddot{\phi}_{i_P^2}}{2} = \omega_1^2 \sin \phi_{i_P^2} + \omega_0^2 \sin \phi_{e_P i_T^2} - (\dot{n}_G^d - 2\dot{n}_P^d). \tag{5.22}$$

with

$$\omega_1^2 = \frac{12\beta'(i_P^{fr})^2}{a_P^2}\left(2\mu_G + \sqrt[3]{2}\mu_P\right).$$

Here β', similar to β, is the resonant strength of $R_{i_P^2}$. The libration of both $\phi_{e_P i_T^2}$

and $\phi_{i_P^2}$ are now modulated by new oscillations, and the presence of these new terms

breaks both adiabatic invariants.

Eq. (5.21) admits both oscillating and circulating solutions – ultimately the system

is driven to the circulating solution. Which resonance is exited first depends on the

relative resonant strengths and on the conditions when the second resonance is first

encountered. In this example, the $R_{i_P^2}$ resonance is destroyed first, which allows the unperturbed $R_{e_P i_T^2}$ resonance to resume decreasing its libration amplitude in accordance with the adiabatic invariant $\omega_0 \cos \Phi = \texttt{constant}$.

The possibility of resonant capture complicates our study of the inclination history of the small satellites because of the difficulty in predicting inclination growths. While the two orbits are trapped into $R_{i_P^2}$, the free inclination of Proteus keeps growing. It is not obvious when the resonance will be broken, and hence it is difficult to estimate i_P^{fr} after traversal of the resonant zone. We find four cases amongst ~ 200 simulations for different resonant zones, and the inclinations are affected only in one of these four cases. Since the capture probability is low, the limitation may not be serious. The actual capture probability might be higher than 2%, however, because our modeled $\frac{Q_N}{\bar{\rho}/(g/cm^3)}$ ranges from 1000 to 30,000. A smaller Q_N leads to artificially rapid orbital evolution which precludes some of the weak trapping events.

5.4 The Chaotic *PL 3:2*

As we follow Proteus and Larissa backward in time to the *PL 3:2* resonant zone, the satellites are closer and the typical spacing between resonances is also smaller. When two strong resonances are very close together, their effective widths can overlap, causing the system to display chaotic behavior. During the *PL 3:2* resonance passage (Fig. 5.9), the semi-major axis of Larissa drops so much during the R_{e_L} resonance that R_{e_P} becomes important before the system escape completely from the first resonance, resulting in temporary trapping into both resonances and chaotic changes to the

orbits. While in the two first-order eccentricity-type resonances, random kicks to the semi-major axes bring a series of higher-order inclination-type resonances into and out of play, including the strong $R_{e_L i_P i_T}$. Chaotic kicks by these resonances, some of which are crossed multiple times, force the free inclinations of the two satellites to wander randomly. The width of the chaotic region depends on the resonant strengths, and hence the masses of the satellites. The tidal migration rate also plays a non-trivial role. Stronger resonances result in wider chaotic regions, and in turn, larger inclination growth. This imposes an immediate problem in estimating the inclination growth through the traverse of the *PL 3:2* resonant zone.

5.4.1   Eccentricity Resonances Overlapping Criterion

It is important to be able to estimate when resonant overlapping occurs. Wisdom (1980) derived such a criterion for two first-order eccentricity resonances in two adjacent resonant zones, taking one satellite to be a test particle. For satellites with negligible masses compared to their planets, resonant zones are well-separated for small p (see Eq. 5.5). For Proteus and Larissa, overlap of resonant zones requires $p \gtrsim 50$, i.e., beyond the *PL 51:50* zone, which only occurs when the satellites are extremely close together. For the vast majority of their evolution history, the Neptunian moons were well-separated enough that this type of overlap does not occur. Within a single resonant zone, however, resonant overlap is much more common as we have seen in Fig. 5.9. Here we determine the criterion under which the two first-order eccentricity resonances of a single resonant zone overlap. This type of overlap
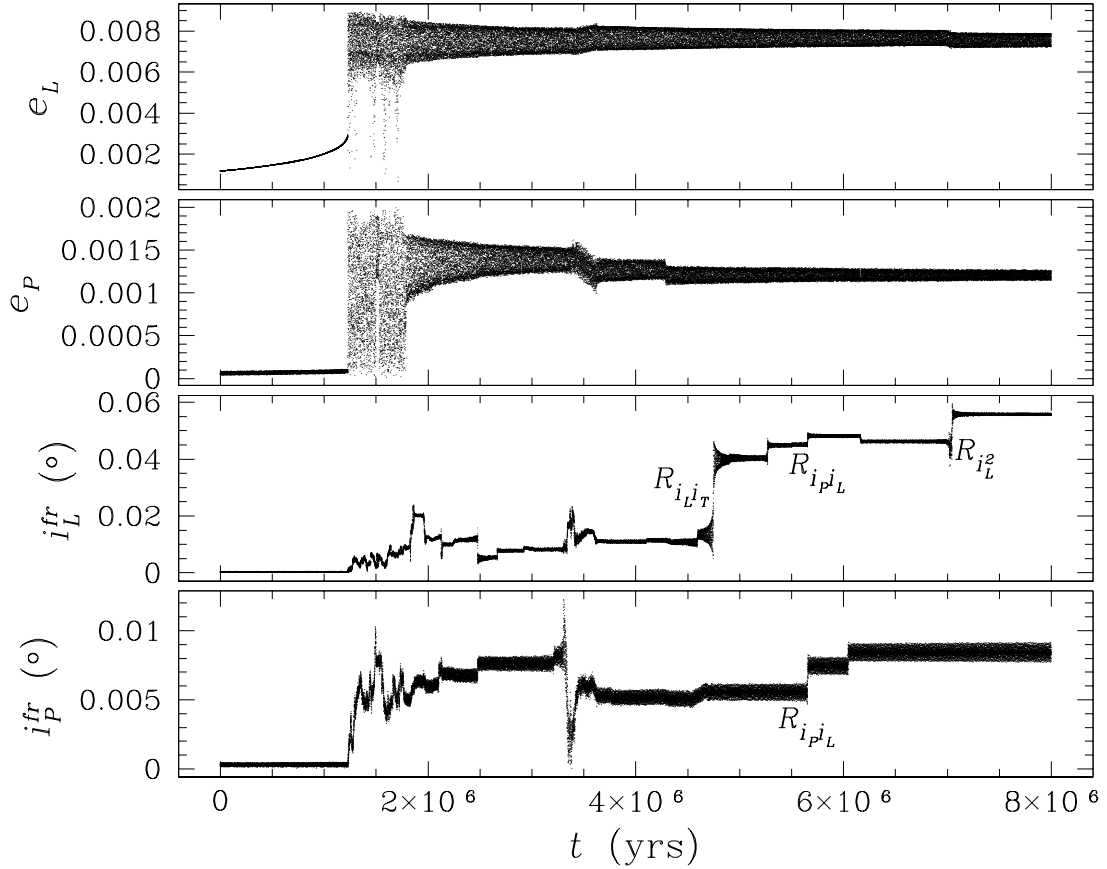
Figure 5.9: The *PL 3:2* passage. The inclinations of the satellites follow a random walk behavior due to the chaotic overlap of the first-order eccentricity resonances. This interaction forces multiple crossings of weaker resonances that affect inclinations. Subsequent to escaping from the chaotic region, additional resonances are traversed. Several second-order resonances are indicated, while other strong ones are located in the chaotic zone and are not easily recognizable. The density of the satellites is $\bar{\rho} = 0.6\,g/cm^3$ and $Q_N = 20,000$.

is particularly important when the two satellites have comparable masses.

The overlap condition is determined by comparing the resonance widths and the spacing between the two resonant centers. Murray and Dermott (1999) calculated the half-widths for the two first-order $p+1:p$ resonances in term of the variation of orbital semi-major axis of either Proteus or Larissa, which read

$$\left|\frac{(\Delta a)_{1/2}}{a}\right|_{e_L} = 4\left[-\frac{\alpha f_d(\alpha)\mu_P}{3}e_L^{res}\right]^{\frac{1}{2}} \tag{5.23}$$

and

$$\left|\frac{(\Delta a)_{1/2}}{a}\right|_{e_P} = 4\left[-\frac{\alpha^3 f_d(\alpha)\mu_L}{3}e_P^{res}\right]^{\frac{1}{2}} \tag{5.24}$$

for R_{e_L} and R_{e_P}, respectively. Here $\alpha = a_L/a_P = [p/(p+1)]^{\frac{2}{3}}$ is the semi-major axes ratio; $f_d(\alpha)$ is the coefficient for the first-order direct term in the expansion of the disturbing function; it is negative and its magnitude increases with α. The values of $f_d(\alpha)$ for small p can be found in Table 8.5 of Murray and Dermott (1999), and we find that $\alpha f_d(\alpha) \approx 0.8\,p$ gives an excellent fit. The eccentricities of Larissa and Proteus when they are exactly in resonance are denoted by e_L^{res} and e_P^{res}, respectively. When kicks occur at resonant encounters, however, e_L^{res} and e_P^{res} are not well defined since both eccentricities jump during the resonance. For example, in the *PL 2:1* zone (Fig. 5.2), $e_L \approx 0.003$ right before the R_{e_L} encounter, while $e_L \approx 0.011$ right after the encounter. Here we use the values right after the encounters, given by Murray and Dermott (1999):

$$e_L^{res} = 2\left[-\frac{\alpha f_d(\alpha)\mu_P}{3p^2}\right]^{\frac{1}{3}},$$

$$e_P^{res} = 2\left[-\frac{\alpha^3 f_d(\alpha)\mu_L}{3p^2}\right]^{\frac{1}{3}}.$$

Note that this might over-estimate the resonant width and bring in an error of about 50%. Using these eccentricities and the approximation $f_d(\alpha) = 0.8\,p$, we find

$$\left|\frac{(\Delta a)_{1/2}}{a}\right|_{e_L} = 2.34\,\sqrt[3]{\mu_P^2 p}, \tag{5.25}$$

$$\left|\frac{(\Delta a)_{1/2}}{a}\right|_{e_P} = 2.34\,\sqrt[3]{\mu_L^2 \alpha^4 p}. \tag{5.26}$$

These approximations show that resonances are wider for more closely spaced and more massive satellites.

Recall that $(\Delta a)_{1/2}/a$ can be the orbital size variation of either Proteus or Larissa in Eqs. (5.23-5.26) when the semi-major axis of the other planet is fixed. Assuming that a_L is fixed, we now calculate the separation between the two resonances in term of a_P to compare with the resonance widths. Values of a_P for R_{e_L} and R_{e_P} in the same $p+1 : p$ resonant zone can be obtain by setting the derivatives of the appropriate resonant arguments to zero:

$$\dot{\phi}_{e_L} = (p+1)\,n_P - p\,n_L - \dot{\varpi}_L \;=\; 0,$$

$$\dot{\phi}_{e_P} = (p+1)\,n_P - p\,n_L - \dot{\varpi}_P \;=\; 0.$$

The difference in a_P gives the spacing between the two resonances:

$$\frac{\delta a_P}{a_P} = \frac{2}{3}\frac{1}{p+1}\left(\frac{\dot{\varpi}_L - \dot{\varpi}_P}{n_P}\right). \tag{5.27}$$

The two eccentricity resonances are closer to each other for larger p, when the two orbits are near each other, and for slower orbital precession rates. In satellite systems, the orbital precession is usually dominated by the effect from the planet's oblateness,

and Danby (1988) gives the relevant pericenter precession rate:

$$\dot{\bar{\omega}} = \frac{3}{2} J_2\, n \left(\frac{R_N}{a}\right)^2,$$

where J_2 is the second-order planetary oblateness coefficient. Eq. (5.27) can thus be simplified to

$$\frac{\delta a_P}{a_P} = J_2 \left(\frac{R_N}{a_P}\right)^2 \frac{1 - \alpha^{\frac{7}{2}}}{p\,\alpha^2}. \tag{5.28}$$

Resonances are better separated at planets with large J_2 values (e.g., Jupiter and Saturn).

The spacing between the two resonances decreases as p or α increases, and overlap occurs when the sum of the two half-widths (Eqs. 5.25-5.26) exceeds the separation:

$$2.34\, p\alpha^2 (\sqrt[3]{\mu_P^2 p} + \sqrt[3]{\mu_L^2 \alpha^4 p}) \gtrsim J_2 \left(\frac{R_N}{a_P}\right)^2 \left(1 - \alpha^{\frac{7}{2}}\right). \tag{5.29}$$

Now we neglect the contribution from the R_{e_P} resonance in Eq. (5.29), which only causes an error of about 20% since m_L is 10 times less than m_P, and solve for large p:

$$p \gtrsim \left[\frac{J_2^3}{\mu_P^2} \left(\frac{R_N}{a_P}\right)^6\right]^{\frac{1}{7}}. \tag{5.30}$$

Although for most satellites the critical p is small, the assumption of large p only adds an error of about 50% even for $p = 1$. Assuming $\bar{\rho} = 0.6\,g/cm^3$, resonance overlap occurs when $p \gtrsim 1.9$ for Proteus and Larissa (exact solution of Eq. 5.29 gives $p \gtrsim 2.3$), which roughly agrees with our simulations: the *PL 3:2* $(p = 2)$ has resonance overlap, while the *PL 2:1* $(p = 1)$ does not.

We calculate the critical resonance where overlap first occurs for the four Neptunian satellites in Table 5.1. Since the resonant widths are dominated by the larger

Table 5.1: Critical resonances for first-order eccentricity resonance overlapping

Satellite Pair	Critical Resonance
PL	3:2
PG	3:2
PD	3:2
LG	6:5
LD	6:5
GD	7:6

mass, the three Proteus pairs have the same critical resonance. The two Larissa pairs also have the same critical resonance, but due to the similar sizes of Galatea and Despina.

This "collision" between eccentricity resonances and the resulting chaotic zone exists for all first-order resonances when the overlap criterion is met. If the resonances are weak, the chaotic zone is narrow and the satellite tilts are not significantly affected. Specifically, during the *PL 3:2* passage shown in Fig. 5.9, if the density of the satellites is less than $0.6 \, g/cm^3$ and $Q_N < 20,000$, the system shows very weak chaos and significant growth of inclinations does not take place despite the chaotic interaction of the two eccentricity resonances. If the satellites are more massive, or if they diverge more slowly, however, the random walk of the orbital elements can continue for a long time, the orbits become highly excited, and the chaotic nature of this resonant zone wipes out all information from earlier times.

Chapter 6

Constraints on Physical Parameters

The intention of this work is to use resonant excitation to explain the current non-zero inclinations of the small inner Neptunian satellites. We have shown in last chapter that the resonant kicks on inclinations are of the same magnitude as the satellites' current free tilts, and that the resonant history of the system can be constrained through an analysis of inclination excitations. Because this history depends on the satellite masses and Neptune's tidal Q, we also put limits on these quantities.

6.1   Satellite Densities

The magnitude of each resonant kick depends on the masses of the satellites, on their initial inclinations and eccentricities, and more weakly, on the tidal drag rate. As long as the two satellites diverge from each other so slowly that the major resonances are traversed in the adiabatic limit, the inclination growth is nearly independent of the actual migration rate. Since the four small satellites have probably migrated by less than a Neptune radius during their lifetime, our simulations show that most first- and second-order resonances are traversed adiabatically. Effects of higher-order resonances are usually insignificant at these migration rates, but can occasionally lead to resonant trapping as discussed above.

In principle, with a system of resonances traversed in the adiabatic limit, we can derive the resonant kick magnitudes analytically to determine how the kicks depend on satellite masses, as is done for two-body resonances by Yoder (1973), Hamilton and Burns (1993) and Murray and Dermott (1999, §8). However, for the Neptunian satellites, this derivation requires a Taylor expansion of the three-body disturbing function, which is beyond the scope of this work. Instead, we take a numerical approach, starting with an analysis of the inclination kicks from the *PL 2:1* resonance passage.

6.1.1   Constraints from a Single *PL 2:1* Passage

Assuming same density for Proteus and Larissa, we have run simulations through the *PL 2:1* resonant zone with satellite density ranging from 0.4 to 2.5 g/cm^3. The total inclination excitation from each simulation is plotted in Fig. 6.1. As we expected, a larger mean density results in greater inclination growth for both Proteus and Larissa. This 2:1 resonance passage can excite Proteus's free inclination to its current value if the satellites' mean density is $\bar{\rho} \sim 1.5\,g/cm^3$. Their density cannot be much greater, or Proteus's free tilt would exceed its observed value, and there is no mechanism to damp this inclination in a few hundred million years.

Although Proteus is able to obtain its free inclination through a single *PL 2:1* passage if $\bar{\rho} \sim 1.5\,g/cm^3$, Larissa can only acquire half of its current tilt. Perhaps this can be explained by relaxing the assumption of equal densities. We might suspect that Proteus has a greater density than Larissa due to its larger mass, even if they
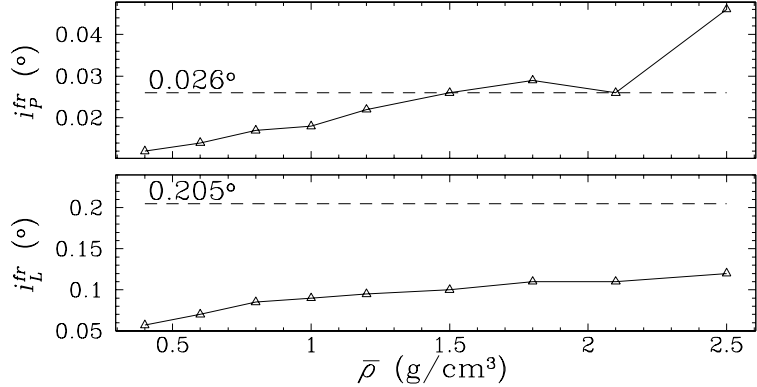
Figure 6.1: Magnitudes of the sum of all 2:1 inclination kicks versus satellite density. Triangles represent the data points obtained through different simulations with different satellite densities (assuming $\rho_P = \rho_L = \bar{\rho}$). The dashed lines show the current free inclinations of the satellites. Top panel shows the inclination kicks on Proteus; bottom panel shows those on Larissa. The inclinations shown here represent the sum over all inclination kicks in plots similar to Fig. 5.2.

formed with similar compositions. In general, the resonant kicks on one satellite depend strongly on the mass of the other one (*see* Eqs. 5.8 and 5.9). Thus, if we keep Larissa's density at 1.5 g/cm^3 (we have to do this to maintain enough of a kick to Proteus' inclination), while allowing Proteus to be denser, we might be able to maintain $i_P^{fr} \approx 0.026°$ and raise i_L^{fr} to $\approx 0.2°$ at the same time. We have run simulations with Proteus's density ρ_P ranging from 1.5 to 4.0 g/cm^3. Our results show that for $\rho_P < 3.5\,g/cm^3$, we are able to keep $i_P^{fr} \approx 0.026°$, with i_L^{fr} increasing smoothly to 0.17°. The resonant kick to Proteus' free inclination does actually drop a little bit due to its weak dependence on m_P. If $\rho_P \geq 3.5\,g/cm^3$, however, high-order resonances become too strong to be ignored (Fig. 6.2). Temporary captures and stochastic processes, similar to what we have seen for R_*, occur throughout the region, and the prediction of final inclinations is impossible.

Figure 6.2: Similar simulation as shown in Fig. 5.2, but Proteus and Larissa have larger and unequal densities: $\rho_P = 4.0 \, g/cm^3$ and 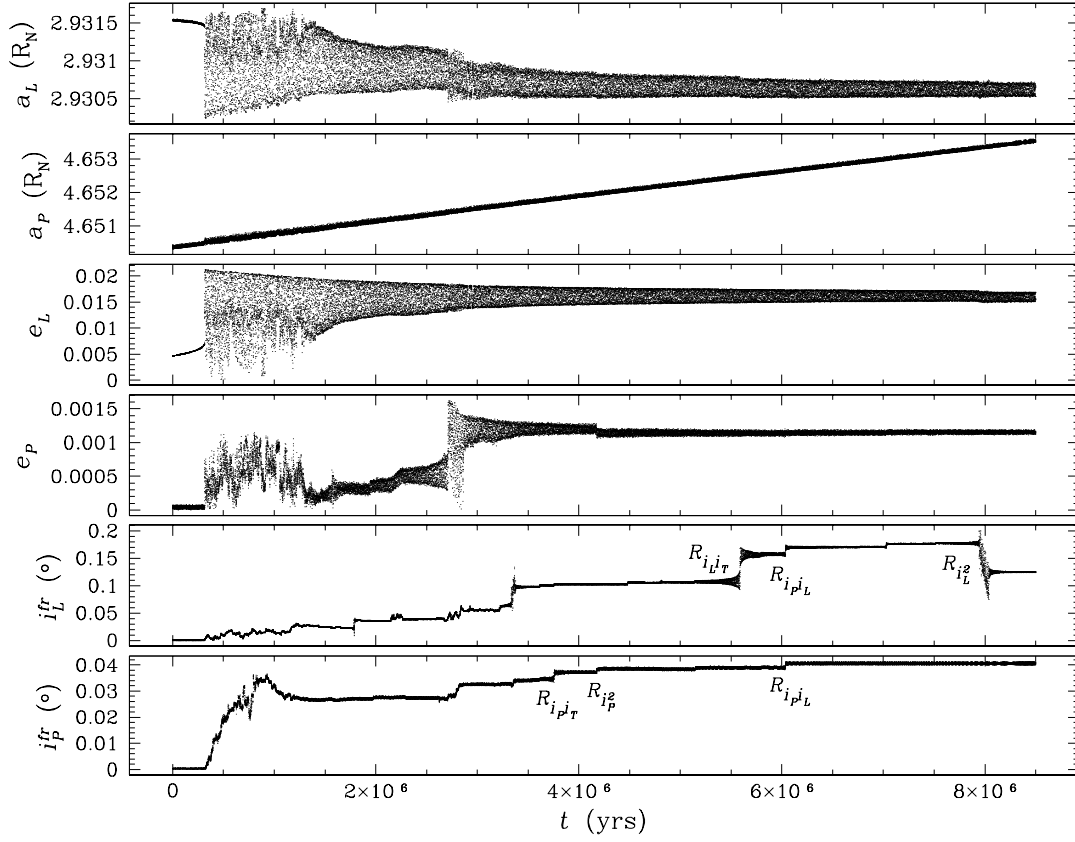$\rho_L = 1.5 \, g/cm^3$. Proteus' migration rate is $3.6 \times 10^{-10} \, R_N/yr$. Due to heavy masses, high-order resonances become important, resonance overlap occurs, and temporary captures and stochastic processes fill the region.

Table 6.1: Numerically-determined inclination kicks through different resonance passages (in degrees). Inclinations and eccentricities are initially set to zero.

Resonance	Satellite	Density (g/cm^3)					
		1.5	1.2	1.0	0.8	0.6	0.4
PL 2:1	Proteus	0.026	0.022	0.018	0.017	0.014	0.012
	Larissa	0.1	0.095	0.090	0.085	0.070	0.057
PD 3:1	Proteus	0.0076	0.0065	0.0060	0.0058	0.0050	0.0040
	Despina	0.090	0.082	0.076	0.070	0.050	0.052
PG 2:1	Proteus	0.016	0.015	0.015	0.013	0.011	0.008
	Galatea	0.100	0.095	0.085	0.085	0.063	0.042
PL 5:3	Proteus	0.013	0.013	0.012	0.011	0.0095	0.0080
	Larissa	0.08	0.075	0.068	0.062	0.056	0.048

It is unlikely that Neptune's small satellites can have densities as high as $3.5\,g/cm^3$. Even $1.5\,g/cm^3$ is probably too large since moonlets formed in the outer solar system are most likely icy and porous, with densities $\lesssim 1.0\,g/cm^3$. Since inclination excitations can be maintained for the lifetime of the satellites and earlier kicks can accumulate, multiple excitations are possible. We now look for solutions that involve most strong Proteus resonances.

6.1.2 Constraints from All Proteus Resonances

In Table 6.1 we summarize the overall inclination kicks on all satellite through the most recent four resonant zones (Fig. 3.3). These simulations are not meant to represent past histories of the satellite orbits, but instead show how the strengths of the resonances compare with one another for different assumed satellite masses. We are able to constrain the satellite masses by matching the total amount of inclination growth that a satellite obtains through multiple resonant passages to its current

92

observed tilt.
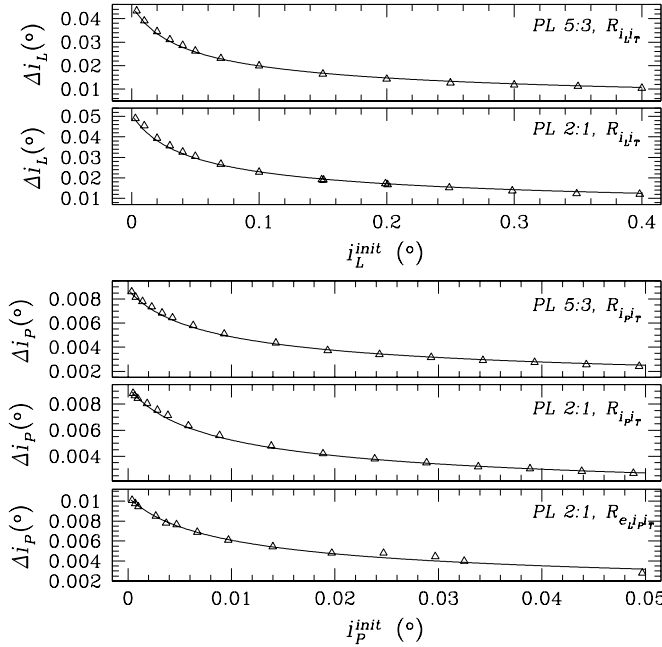
Figure 6.3: Magnitudes of the three-body resonant kicks versus satellite's initial free inclinations for five resonances. The top two panels show the $R_{i_L iT}$ kicks on Larissa during *PL 5:3* and *PL 2:1* passages. The bottom three panels show the $R_{i_P iT}$ and $R_{e_L i_P iT}$ kicks on Proteus during the same passages. *Triangle*: kick magnitudes from different simulations with various initial free inclinations; *solid line*: curves fit to Eq. (6.1).

Due to the limitation of computing power, we can only carry out realistic N-body simulations for the time spans during which two satellites cross a resonant zone. We assume that between resonant zones, satellite tides fully damp eccentricities but leave free inclinations unaltered. Adding the effects of multiple resonant zones, therefore, requires that the later resonances be encountered with non-zero free inclinations. Thus we cannot use the results in Table 6.1 to directly add up resonant perturbations to inclinations because of the assumption that satellites initially reside in their Laplace planes. In order to correctly add successive inclination kicks to a satellite, we need to understand how the total inclination growth through a resonant zone depends on initial inclinations.

To address this issue, we ran sets of simulations to measure the effects of the initial inclinations on the magnitudes of the resonant kicks for the five strongest three-body

resonances in the *PL 5:3* and *PL 2:1* resonant zones. We find that the initial free inclination of Proteus does not significantly affect the kicks on Larissa, and vice versa, confirming that the resonant kicks are forced primarily by Triton rather than the closer moon. Since the resonant strengths are proportional to satellite inclinations, we might expect that larger initial tilts would result in stronger kicks. Surprisingly, however, the kick magnitude decreases extremely rapidly with increasing initial inclination of the affected satellite, as shown in Fig. 6.3.

We find that the simulation data from all individual three-body resonances is remarkably-well fit by:

$$\Delta i = \frac{\Delta i_0}{\sqrt{1 + 2\frac{i_0}{\Delta i_0}}}, \tag{6.1}$$

where Δi is the kick magnitude, i_0 is the initial inclination, and Δi_0 is the kick magnitude at $i_0 = 0°$. We determine Δi_0 through the fitting process, with excellent agreement with numerical observations as seen in Fig. 6.3. If we treat the vertical oscillations as a simple harmonic oscillator, then Δi represents an amplitude change and the energy in the oscillation is proportional to i^2. The energy pumped into the system by each resonance is then

$$\Delta E \propto (i_0 + \Delta i)^2 - i_0^2 = \left[\frac{1 + 2i_0/\Delta i}{1 + 2i_0/\Delta i_0}\right] \Delta i_0^2.$$

The term in the bracket is an increasing function of i_0 since $\Delta i_0 > \Delta i$ for all i_0. Thus, although the amplitude of the inclination kick decreases for increasing initial inclination i_0, the energy input actually increases.

Since kicks from these three-body resonances dominate the inclination growth and all obey the same equation, the overall change in inclination attained from passage

through a full resonant zone roughly follows the same rule. Eq. (6.1) shows that the contribution to inclination growth by a resonant zone passage is more significant if those resonances occur earlier in time when the satellites' free inclinations are still small. For example, the *PL 2:1* passage can kick Larissa's inclination up to 0.085° ($\bar{\rho} = 0.8\,g/cm^3$) if it is the only resonant zone the satellite has gone through, but if the satellite already has a 0.1° free tilt excited by earlier resonances, then the kick is only 0.046° according to Eq. (6.1).

Now we know how to combine resonant kicks from different zones, and are set to compute satellite masses by equating the total resonant kicks to the satellites' current free inclinations. But an immediate difficulty is that we do not know how many resonant zones the satellites have passed through since the tidal evolution timescale itself is not well-constrained. Fortunately, however, the current free inclinations of Proteus, Larissa, Galatea, and Despina provide strong constraints on the number of past resonant encounters.

The observed free tilts of Galatea and Despina are both about 0.06°, Larissa's free inclination, at ∼ 0.2°, is three times as large, and Proteus has a smaller inclination of 0.026° (Table 3.1). While the first three satellites have similar masses (within a factor of 2), Proteus is 10 times more massive, making it simultaneously the strongest perturber in the system and the hardest to perturb. For this reason, its free inclination is significant although it is the smallest among the four. We now combine the effects of all resonances discussed in last section, and attempt to construct a migration scenario that can account for the free tilts of all four satellites.

We have shown in last section that the single *PL 2:1* resonance passage acting alone provides too little current free tilts for Larissa and probably for Proteus as well. Furthermore, the inclinations of Galatea and Despina likely require that these two satellites once had resonant interactions with Proteus, so the earlier resonances, *PD 3:1* and *PG 2:1*, must also have occurred. These three resonances have similar strengths, and the inclination kicks on the smaller satellite are about the same, as discussed previously. If these were the only resonant zones that the system has traversed, the three smaller satellites would have comparable free tilts today. Galatea and Despina do actually have similar inclinations, and Table 6.1 shows that, for an average density $0.4\,g/cm^3 < \bar{\rho} < 0.8\,g/cm^3$, the free inclinations of these two satellite can be excited to close to their current values. Larissa, however, has an inclination three times larger, which requires additional resonance passage(s). In our tidal evolution model, the next strong Proteus resonance is the *PL 5:3*, which involves Larissa. Thus, these four Proteus resonances might provide a consistent solution.

We now test the above hypothesis with our numerical data. We combine the results from Table 6.1, scaled by Eq. (6.1) as appropriate, and plot the final free inclinations acquired by the satellites for several possible past histories in Fig. 6.4. The curves for each satellite are represented by step functions with steps occurring at resonant zones that involve that satellite. It is important to realize that these curves are not evolutionary tracks, but are rather final status plots: inclinations at any given point in the past represent the predicted orbital tilts of the satellites today assuming that the system formed at that past time. We only calculate kicks for the
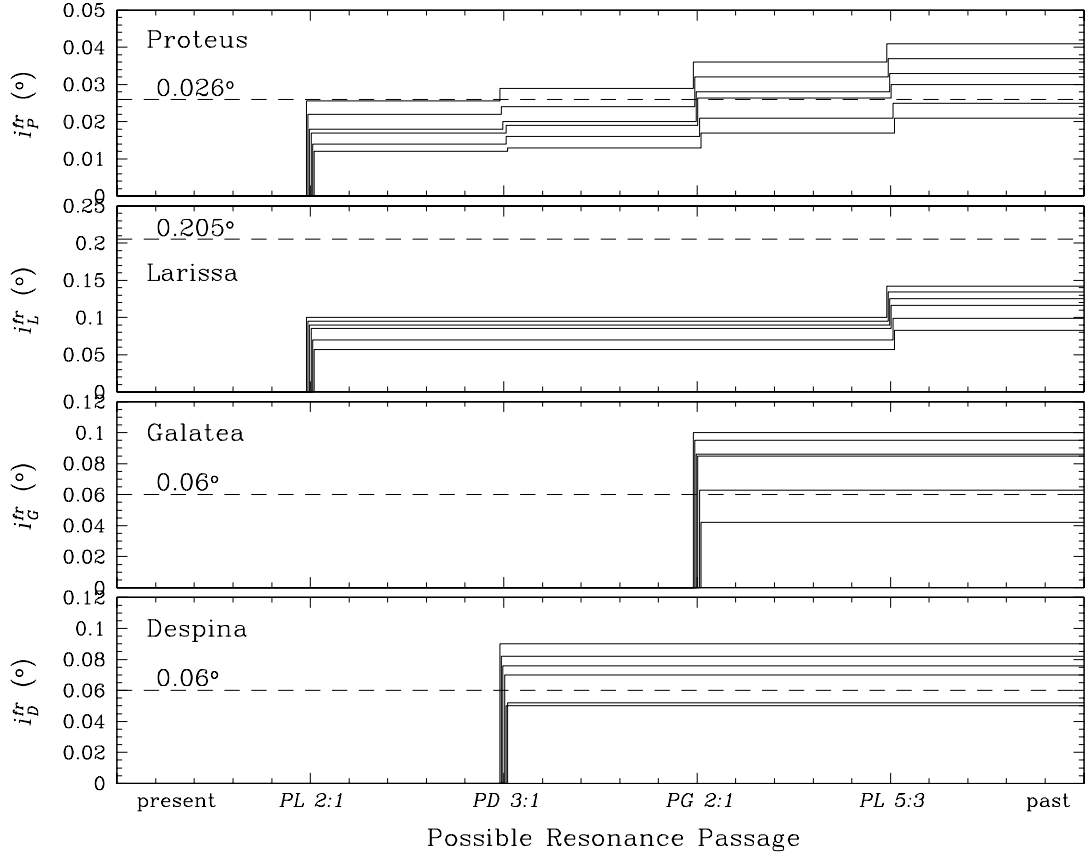
Figure 6.4: The cumulative free inclinations of Proteus (i_P^{fr}), Larissa (i_L^{fr}), Galatea (i_G^{fr}), and Despina (i_D^{fr}). The curves show the final free inclinations that the satellites acquire versus their formation time represented in terms of resonant zone passages (c.f. Fig. 3.3). Resonances to the left of the formation time have actually occurred, while those to the right have not. We assume all satellites have the same densities; solid curves represents different bulk densities: from top to bottom: $\bar{\rho} = 1.5$, 1.2, 1.0, 0.8, 0.6, $0.4\,g/cm^3$. The single exception to this is the Despina 0.4 curve which is actually above the 0.6 curve due to stochastic variations. The dashed horizontal lines represent the current free inclinations of the satellites.

most recent four Proteus resonances since the chaotic behavior of *PL 3:2* prevents any useful estimates of prior inclination growth. The curves for Galatea and Despina are very simple (with only one step) since they each can only be involved in at most one major resonant zone passage. Larissa may go through two major zones, and there are four possible ones for Proteus.

If *PL 2:1* is the only resonant zone the system has gone through, Fig. 6.4 shows that, with a mean density of $1.5\,g/cm^3$, i_P^{fr} can be kicked up to near its current value, but Larissa can only obtain about half of its current orbital tilt, as we have discussed in the last section. If the system starts from an earlier configuration to include both the *PD 3:1* and the *PG 2:1* resonant zones, the inclinations of both Galatea and Despina can be pushed high enough with a density satisfying $0.4\,g/cm^3 < \bar{\rho} < 0.8\,g/cm^3$. For i_P^{fr} to reach $0.026°$ in this case, however, a density of $0.6\,g/cm^3 < \bar{\rho} < 1.0\,g/cm^3$ is required. This three-resonant-zone scenario leaves Larissa with less than half its current tilt. With an earlier formation time so that all four Proteus resonances are traversed, the density required by Proteus's free inclination drops to $0.4\,g/cm^3 < \bar{\rho} < 0.8\,g/cm^3$ due to the extra kick from Larissa. Although i_L^{fr} is more excited, however, Larissa still attains just over a half of its current inclination for this density range. In fact, i_L^{fr} can only be excited to $\sim 0.14°$ even if the mean density is as high as $1.5\,g/cm^3$. Thus the three or four Proteus resonance passages provide a consistent solution for the free tilts of Proteus, Galatea, and Despina with $0.4\,g/cm^3 < \bar{\rho} < 0.8\,g/cm^3$, a density range that is physically plausible. But the current inclination of Larissa cannot be matched with the assumptions of equal satellite densities in any of the

scenarios considered so far. What happened to Larissa?

The first possible solution to the Larissa problem is to allow satellites to have different densities. But this leads immediately to the same problem that we faced in last section: in order for i_L^{fr} to be kicked more, we need a more massive Proteus, or a less massive Larissa. The mass of Proteus cannot be increased much since this would result in larger inclinations for Galatea and Despina than currently observed. Reducing Larissa's mass helps a little, but the dependence of the PL kick strengths on Larissa's mass is very weak since Proteus is the dominate mass. Our simulations show that the cumulative inclination kick on Larissa only increase from $0.1°$ to $\sim 0.13°$ if we drop ρ_L from $0.6\,g/cm^3$ to $0.05\,g/cm^3$ while keeping ρ_P at $0.6\,g/cm^3$. Even this unrealistically-low satellite density does not solve the problem.

A second possible solution is to allow Larissa to pass through more resonances. The next Proteus-Larissa resonant zone is the chaotic *PL 3:2*. For this zone, our simulations indicate that chaotic behavior becomes significant only for density $\bar{\rho} > 0.8\,g/cm^3$, in which case Proteus usually gets an overall kick $> 0.025°$ through the random walk process). Adding kicks from later resonances, this results in too large a tilt. However, for density $\bar{\rho} \le 0.6\,g/cm^3$, the chaotic behavior is weak and the orbital inclination growths are reasonable. In our example shown in Fig. 5.9 ($\bar{\rho} = 0.6\,g/cm^3$), the kicks on Proteus and Larissa are $0.009°$ and $0.06°$, respectively, which bring the overall inclination growths of the two satellites through the 5 resonance passages to $i_P^{fr} = 0.029°$ and $i_L^{fr} = 0.128°$, where we have used Eq. (6.1) to model the later kicks. If $\bar{\rho} = 0.4\,g/cm^3$, the *PL 3:2* kicks on the two satellites are $0.008°$ and $0.05°$,

99

which can only promote the inclination growth of Larissa through the five resonant zones to a total of $i_L^{fr} = 0.107°$. Although the actual inclination kicks may vary, our simulations show that for a specific density, they all fall in roughly this range. Hence, Larissa's orbit cannot be effectively tilted even if the troublesome *PL 3:2* resonant zone is included. Perhaps there is a rare outcome of the chaotic interactions in which Larissa's inclination is highly excited, but we have seen no evidence that this is the case. Including earlier resonances is problematic: the preceding one, *PD 2:1*, excites the inclination of Despina, forcing Proteus' density to $\bar{\rho} < 0.4\,g/cm^2$ to keep that satellite's inclination low and making it less likely to produce similar tilts for Despina and Galatea. The earlier *PG 5:3* would then be required. The trend here is clear – additional *PD* and *PG* resonances force Proteus' density down, making additional *PL* resonances less effective. Tweaking the tidal model might change the order of some resonances (e.g. the *PL 3:2* and *PD 2:1*, cf. Fig. 3.3), but our basic conclusion is unaltered. There is no set of Proteus resonances that can simultaneously make the inclination of Larissa large while keeping those of Galatea and Despina low.

A third possibility includes invoking the weaker, but more numerous, resonances among the three smaller satellites (Fig. 3.3), which we have neglected until now. Could the inclusion of these resonances solve the problem of Larissa's inclination excess? Since the masses of Larissa, Galatea, and Despina are 10 times smaller than Proteus', these resonances are very weak even though the satellites are closer to one another than to Proteus. Our simulations show that typically inclinations of both satellites show a $\sim 0.01°$ overall growth through a single zone passage, assuming zero

initial free inclinations. The cumulative effect of these kicks could potentially be large given that there are so many of them. However, due to the strong dependence of the kick magnitude on the initial free inclinations, these weak kicks, albeit numerous, do not add much to the satellites' free tilts, especially for the ones occurring after any of the more powerful Proteus resonances. Furthermore, Fig. 3.3 shows that Larissa, Galatea, and Despina have all traversed a similar number of these weak resonant zones – in fact, Galatea receives more kicks than the other two because of its central location – it is nearly impossible to increase Larissa's inclination significantly while keeping those of the other two small. Inclusion of these weak resonances, however, does systematically drive our solution for $\bar{\rho}$ towards slightly lower values.

A fourth possible cause of Larissa's inclination excess is that the satellite might actually have been captured into a resonance. We have seen an unusual inclination capture following a three-body eccentricity capture with the result that both Proteus' eccentricity and inclination are forced to increase (Fig. 5.8). Although the chance is low because of Larissa's smaller mass, it is possible that the satellite was once captured into a similar resonance ($R_{i_L^2}$) with either Galatea or Despina. Fig. 3.3 shows that there are several possibilities, with earlier resonances more likely to capture Larissa than later ones because its inclination was smaller in the past. Expanding our search to include the tiny inner moons, Naiad and Thalassa, we note that captures are more likely since Larissa's orbit is approaching the inner two orbits and resonant trapping into strong low-order inclination resonances is possible without a prior capture. Naiad's extremely high free inclination also points to a previous capture (Banfield and

101

Murray, 1992), and Larissa would be a natural candidate. Assuming that Larissa's semi-major axis migrated from the synchronous orbit to its current orbit, Larissa's interior 2:1 resonance would move from $2.08\,R_N$ to $1.83\,R_N$, which brackets the current orbit of Naiad at $1.91\,R_N$. Although Naiad was somewhat further away from Neptune in the past, there is a good chance that the 2:1 Larissa-Naiad resonance did actually occur. Similarly, Larissa's 2:1 or 5:3 internal resonances may have swept across Thalassa's orbit, implying possible strong interactions with that satellite. The odds of capture into a resonance involving Larissa's inclination is a strongly decreasing function of its initial tilt, and it is hardly possible if Larissa's orbit is tilted more than some critical value (Borderies and Goldreich, 1984). Hence, the capture probably occurred earlier on. Two main possibilities exist: i) capture occurred prior to the *PL 5:3*, with two subsequent Larissa kicks from the *PL 5:3* and *PL 2:1*, and ii) capture occurred prior to the *PG 2:1* with only one subsequent Larissa kick, the recent *PL 2:1*. For the density range $0.4\,g/cm^3 < \bar{\rho} < 0.8\,g/cm^3$, scenario (i) requires Larissa to have a free inclination of $0.14°$ after escaping from the hypothetical resonant capture, while in scenario (ii), the satellite needs to have a $0.16°$ free tilt after escape. Although requiring an additional resonant capture, we think that this is the most likely scenario and will pursue the details in a future publication.

Densities in the range $0.4\,g/cm^3 < \bar{\rho} < 0.8\,g/cm^3$ implies large porosities, but similar values are measured for both Saturnian and Jovian satellites. Nicholson et al. (1992) measured the densities of Saturn's co-orbital satellites, Janus and Epimetheus, at $\bar{\rho} \approx 0.6\,g/cm^3$. More recently, Renner et al. (2005) measured the densities of

Prometheus ($0.4\,g/cm^3$) and Pandora ($0.49\,g/cm^3$), and Porco et al. (2005) estimated the densities of Atlas and Pan to be $\sim 0.5\,g/cm^3$. All those Saturnian satellites are made of nearly-pure porous water ice. The density of the Jovian satellite Amalthea ($\bar{\rho} = 0.9\,g/cm^3$ Anderson et al., 2005) is a little bit higher, but the satellite is made of a mixture of water ice and rock, so high porosity is also expected.

For such low densities, the Roche limit of the Neptunian system is located between $3.1\,R_N$ and $3.9\,R_N$. Accretion for small satellites, however, is possible within the Roche limit through non-gravitational amalgamation. Or perhaps the satellites are fragments from larger bodies that were forced inside the Roche radius and were then disrupted.

6.2 Tidal Evolution Timescale and Q_N

The four satellites have most likely passed though three or four strong Proteus resonant zones: definitely the *PL 2:1*, the *PD 3:1*, and the *PG 2:1*, and possibly the *PL 5:3* before those. If the system formed with a configuration between *PL 3:2* and *PG 2:1* in Fig. 3.3, this provides a natural explanation for the inclinations of at least three of the four satellites. We enlarge this region of the plot in Fig. 6.5. Due to the observational error in satellite size measurements (Table 3.1), which leads to mass uncertainties, the evolution tracks of Proteus and Larissa fall somewhere within the lightly-shaded area in Fig. 6.5, resulting in uncertainties of the location of *PL 3:2* and *PG 2:1* at $4.99\,Gyr < t < 6.06\,Gyr$ and $2.92\,Gyr < t < 3.72\,Gyr$, respectively, as indicated by the darkly-shaded area. As discussed before, the evolution timescale is
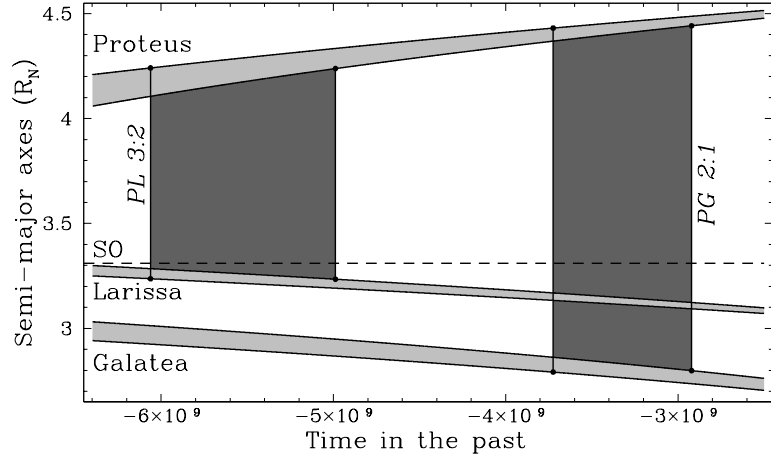
Figure 6.5: Possible initial configurations of the system. The plot shows a magnified region of Fig. 3.3. The evolution tracks of Proteus, Larissa, and Galatea lie anywhere in the respective lightly-shaded areas. The darkly-shaded areas show the possible locations of *PL 3:2* and *PG 2:1* resonant zones. The boundaries of these areas are determined by the observational uncertainties of satellite sizes. The system started with an initial configuration between the earliest possible *PL 3:2* and the latest possible *PG 2:1*. As with Fig. 3.3, times need to be multiplied by the factor $\frac{Q_N/20,000}{\bar{\rho}/(0.6\,g/cm^3)}$.

affected by Q_N and $\bar{\rho}$. Thus, the formation time of the system is estimated at

$$\left(\frac{Q_N/20,000}{\bar{\rho}/(0.6\,g/cm^3)} \times 2.92\,Gyrs\right) \quad < \quad t \quad < \quad \left(\frac{Q_N/20,000}{\bar{\rho}/(0.6\,g/cm^3)} \times 6.06\,Gyrs\right). \quad (6.2)$$

Triton was most likely captured at a very early stage of Solar System history ($\sim 4.5\,Gyr$ ago), when there were still plenty of planetesimals for Neptune to interact with (Agnor and Hamilton, 2006). The circularization of Triton takes merely a few $100\,Myr$, thus, we assume that the inner satellites date back to ~ 4 billion years. Substituting $t \approx 4\,Gyrs$ and $0.4\,g/cm^3 < \bar{\rho} < 0.8\,g/cm^3$ into Eq. (6.2), we estimate

$$9,000 < Q_N < 36,000.$$

Part of this uncertainty comes from satellite size and density uncertainties, while the rest comes from not knowing whether the system formed closer to *PL 3:2* or

104

PG 2:1. Although $4\,Gyrs$ is a feasible age for the small satellites, they may have been subsequently destroyed by cometary bombardment as suggested by Smith et al. (1989). This effectively resets the clock to the time of destruction and lowers the lower bound on Q_N. Nevertheless, we believe that this late and complete destruction of the inner Neptunian satellites is not a very likely possibility. Another uncertain factor that affects the Q_N determination is k_{2N}. The Love numbers of the giant planets are computed by several authors with different models. We have adopted $k_{2N} = 0.41$ from Burša (1992), while an earlier estimation by Gavrilov and Zharkov (1977) gives a much smaller value ($k_{2N} = 0.13$). Since the tidal constraints are actually on Q_N/k_{2N} (Eq. 3.1), the smaller Love number would lead to a drop in both the upper and lower bounds of Q_N by a factor of 3.

Banfield and Murray (1992) estimated Q_N with similar method but different dynamical constraints. They took $k_{2N} = 0.39$ based on a model by Dermott et al. (1988), assumed satellite densities to be $\sim 1.2\,g/cm^3$, and obtained a lower limit $Q_N > 12,000$ by requiring Proteus to form outside of the synchronous orbit and an upper limit $Q_N < 330,000$ from the Naiad capture event. As our determined satellite density of $0.4-0.8\,g/cm^3$ is half that assumed by Banfield and Murray (1992), we scale their Q_N estimates to $4,000 < Q_N < 220,000$ so that they can be directly compared to our estimates. Instead of assuming that Proteus migrated from the synchronous orbit at $\sim 3.31\,R_N$, we have shown that the satellite could not have formed closer to Neptune than $4.20\,R_N$ in order to avoid the *PL 3:2* resonance. This explains our improved lower bound of $Q_N > 9,000$. Our biggest improvement, a factor of 6 times

Table 6.2: Q of giant planets

Planet	Author	Q	k_2	Q/k_2
Jupiter	GS66	$\geq 100,000$	1.5	$\geq 66,000$
	YP81	$(0.6-20) \times 10^5$	0.379 (GZ77)	1.6×10^5-5×10^6
Saturn	GS66	$\geq 60,000$	1.5	$\geq 40,000$
	P80	$\geq 16,000$	0.341 (GZ77)	$\geq 45,000$
Uranus	GS66	$\geq 72,000$	1.5	$\geq 48,000$
	TW89	11,000 - 39,000	0.104 (GZ77)	105,000 - 375,000
Neptune	BM92	4,000 - 220,000*	0.39 (D88)	10,000 - 560,000*
	This work	9,000 - 36,000	0.41 (B92)	22,000 - 90,000

GS66: Goldreich and Soter (1966); GZ77: Gavrilov and Zharkov (1977); P80: Peale et al. (1980); YP81: Yoder and Peale (1981); D88: Dermott et al. (1988); TW89: Tittemore and Wisdom (1989); BM92: Banfield and Murray (1992); B92: Burša (1992);

reduction in the upper limit of Q_N, arises from the constraint that Proteus traversed at least 3 resonant zones.

Several authors have previously estimated Q for other giant planets based on similar dynamical constraints; we collect these results in Table 6.2 and compare them to our own. It is best to compare the values of Q/k_2 in the final column because this is the quantity directly constrained by all dynamical studies. Goldreich and Soter (1966) were the first to systematically investigate the planetary Q's in the solar system. Based on the known satellites at that time, they estimated lower limits of Q for Jupiter ($Q_J \geq 100,000$), Saturn ($Q_S \geq 60,000$), and Uranus ($Q_U \geq 72,000$). They ignored the internal structure of the planets and assumed a uniform $k_2 = 1.5$. They also assumed that these satellites could initially migrate from the surface of the planet. The existence of synchronous orbits, however, reduces the amount of tidal migration and lifts their lower limits by a factor of $2-3$. Yoder and Peale (1981)

addressed this and obtained a lower bound for Jupiter's Q: $Q_J \geq 64,000$, using $k_{2J} = 0.379$ computed by Gavrilov and Zharkov (1977). Yoder and Peale (1981) also estimated the upper limit of Q_J based on tidal heating required by Io, and obtained $Q_J \leq 2 \times 10^6$. Peale et al. (1980) corrected Saturn's Q with more reliable k_{2S} from Gavrilov and Zharkov (1977), and estimated the lower bound to be $Q_S \geq 16,000$. The lower bounds of both Q_J/k_{2J} and Q_S/k_{2S} are larger than what we find for Neptune. Recall that Q is an empirical measurement of the energy dissipation properties of planets that is not well understood physically.

For Uranus, the closest sibling of Neptune, Tittemore and Wisdom (1989) placed Q_U between 11,000 and 39,000 based on the resonant history of the Uranian satellites. However, their Q_U/k_{2U} value is about 4 times larger than our Q_N/k_{2N}. Although one might expect these two similar-sized planets to have similar Q and k_2, different internal structures of the planets – Neptune is denser and has a much stronger internal heat source – may lead to significantly different Q/k_2 values.

6.3 Q_P and Q_L

The current eccentricities of Proteus and Larissa have significant non-zero values (Table 3.1), which we have interpreted as a signature of the recent *PL 2:1* resonance passage. In Chapter 5, we derived a constraint on satellite Q based on this interpretation (Eq. 5.1).

With density between 0.4 and $0.8\,g/cm^3$, our numerical simulations show that Proteus and Larissa can attain eccentricities of $0.0011 - 0.0014$ and $0.008 - 0.01$ dur-

ing the *PL 2:1* passage, respectively. After the resonance, their eccentricities damp to current values of 0.00053 and 0.00139 according to Eq. (2.28). Immediately after *PL 2:1*, the satellites' semi-major axes must satisfy $a_P^3/a_L^3 \simeq 4$; they then evolve following Eq. (3.1), and the two satellites migrate to their current orbits simultaneously. Based on these constraints, we calculate the semi-major axes displacements of the two satellites after the *PL 2:1* encounter: Larissa has migrated $0.014 - 0.016\,R_N$ inward, while Proteus' semi-major axis has increased by $0.010 - 0.013\,R_N$. The uncertainties are primarily due to the observational error of satellite sizes. Substituting these measurements into Eq. (5.1), we find

$$0.004 < \frac{Q_P}{Q_N} < 0.02, \ 0.002 < \frac{Q_L}{Q_N} < 0.006.$$

We have adopted Neptune's Love number $k_{2N} = 0.41$, as computed by Burša (1992). The internal strength, $\tilde{\mu}_s$, is unknown for most satellites, but it is not expected to be as sensitive to satellite composition and shape as Q_s is. We estimate $\tilde{\mu}_P$ and $\tilde{\mu}_L$ based on the formula $\tilde{\mu}_s \approx (10^4\,km/R_s)^2$ given by Murray and Dermott (1999). For $9,000 < Q_N < 36,000$, we find

$$36 < Q_P < 700, \ 18 < Q_L < 200.$$

This is an interesting result since the tidal Q of satellites is more poorly known than planetary Q's – very few dynamical events can provide useful constraints. The only satellite with a well-determined Q is our own Moon, with $Q_M = 27$ (Yoder, 1995). This is within the range of our estimates for Proteus and Larissa, but the size of the Moon is much larger than the two Neptunian satellites. For other satellites

of the giant planets, Goldreich and Soter (1966) estimated that $Q_s < 500$ based on a rough assumption of satellite rigidity. Yoder and Peale (1981) estimated Europa's Q with an eccentricity damping method similar to what we have used, and obtained $Q_E \gtrsim 2 \times 10^{-4} Q_J$. They were also able to estimate Io's Q through an analysis of tidal heating of the melting moon: $Q_I \approx 0.001 Q_J$. These values fall into the same general range as our new estimates for Proteus and Larissa.

Part III

Secular Interactions with Eccentricity Damping

Chapter 7

Background

In this and the following three chapters, we investigate secular interactions between planetary pairs. Initially, we follow Wu and Goldreich (2002) to study the role of secular interaction in maintaining the eccentricities of "hot-Jupiters", and extend the basic secular theory to apply to systems subject to tidal damping of eccentricities. Finally, we apply our results to actual extrasolar planetary systems and explain how our theory can guide planet searches. The material in this part is currently in preparation for submission to *ApJ*.

7.1 Extrasolar Planets

Since the first Jupiter-sized planet was discovered outside the Solar System around 51 Pegasi in 1995 (Mayor and Queloz, 1995), more than 230 extrasolar planets have been found orbiting Sun-like stars (the Extrasolar Planet Encyclopaedia, *http://exoplanet.eu/*). These extrasolar planetary systems are largely unlike our own Solar System. The majority of the planets are Jupiter-sized, are located much closer to their stars, and display substantially larger eccentricities (Juric and Tremaine, 2007). In the past decade, many mechanisms have been studied in order to explain these unusual planetary architectures (see a recent review by Namouni (2007), and references therein),

including planet-planet scattering, planet-disk interaction, mean-motion resonance passage, Kozai resonances, etc. All these mechanisms can excite orbital eccentricity effectively. For planets with large semi-major axes, the excited eccentricities may last for billions of years, explaining why their orbits are still eccentric today. Problems arise, however, for planets very close to stars – the so-called "hot-Jupiters" with orbital periods typically less than a week.
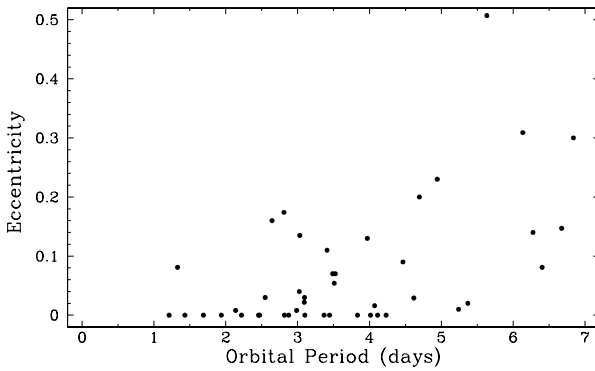
Figure 7.1: Eccentricities of "hot-Jupiters". Data courtesy the Extrasolar Planet Encyclopaedia (*http://exoplanet.eu/*).

Stars and planets raise tides on each other which, in turn, perturb the planet's orbit. Planetary tides raised by the star damp the orbital eccentricity quickly in the same way that satellite tides circularize a satellite's orbit (Section 2.5), especially for systems with "hot-Jupiters" in which tides are rather strong due to the small separations. We rewrite Eq. (2.28) in terms of stellar and planetary parameters:

$$\lambda = -\frac{\dot{e}}{e} = \frac{63}{4} \frac{1}{\tilde{\mu}_p Q_p} \frac{m_*}{m_p} \left(\frac{R_p}{a}\right)^5 n, \tag{7.1}$$

where m_* is the mass of the star. For giant planets in the Solar System, $\tilde{\mu}_p Q_p \gtrsim 10^5$ (see Goldreich and Soter, 1966; Peale et al., 1980; Yoder and Peale, 1981). We assume most extra-solar "hot-Jupiters" have similar values, and thus their typical eccentricity damping timescales are only a few hundred million years, implying that they should all have circular orbits.

We plot the eccentricities of all "hot-Jupiters" with sub-week orbital periods in Fig. 7.1 and notice that, although the average eccentricity is much less than that of all known planets, more than half of the 44 "hot-Jupiters" have orbits with eccentricities significantly different from zero. This observation requires an explanation; possibilities include i) the systems are recently formed, ii) the planetary $\tilde{\mu}_p Q_p$ values are underestimated so that tidal timescales are much longer, and iii) forcing from an exterior planet prevents circularization. We explore the third option here and investigate the interactions between a "hot-Jupiter" and a more distant companion.

In systems with more than one planet, the most significant orbit-orbit interactions are mean-motion resonances, which have been studied in detail for the satellite systems (see Part II and reviews by Greenberg, 1977; Peale, 1986) and for some extrasolar planetary systems (Chiang, 2003; Beaugé et al., 2003; Lee, 2004). Mean-motion resonance passages during planetary migration can be effective at exciting orbital eccentricities. In addition, a long-term secular interaction exists among orbits. Studies of the secular perturbations of the Solar System have been undertaken by Brouwer et al. (1950), and of the Uranian satellites by Dermott and Nicholson (1986). The discovery of extrasolar multi-planet systems (Butler et al., 1999) provides more places to apply secular theory (Adams and Laughlin, 2006). Wu and Goldreich (2002) were the first to use secular interactions to explain the non-zero eccentricity of a "hot-Jupiter". More recently, Barnes and Greenberg (2006b) have shown that the known multi-planet systems tend to be near the separatrix dividing apsidal circulation from libration.

7.2 Secular Modes

Secular perturbations arise from terms of the disturbing function that do not involve the fast-changing orbital longitudes. In Section 2.3, we pointed out that for the lowest-order terms with angular arguments (Eq. 2.15)

$$\phi_e = \varpi_1 - \varpi_2 \text{ and } \phi_i = \Omega_1 - \Omega_2,$$

Lagrange's planetary equations can be linearized.

With the disturbing potentials for both orbits independent of λ and ϵ, Eq. (2.6) shows that the semi-major axes of the two orbits remain constant. This is a general result: secular or orbital-averaged perturbations between planets never affect the semi-major axes, which means that long-term energy transfer between the orbits does not occur. For small e and i, Eqs. (2.7 - 2.10) can be simplified to (Murray and Dermott, 1999, §7.1)

$$\frac{de_j}{dt} = -\frac{1}{n_j a_j^2 e_j} \frac{\partial \mathcal{R}_j^{\text{sec}}}{\partial \varpi_j}, \tag{7.2}$$

$$\frac{d\varpi_j}{dt} = +\frac{1}{n_j a_j^2 e_j} \frac{\partial \mathcal{R}_j^{\text{sec}}}{\partial e_j}; \tag{7.3}$$

$$\frac{di_j}{dt} = -\frac{1}{n_j a_j^2 i_j} \frac{\partial \mathcal{R}_j^{\text{sec}}}{\partial \Omega_j}, \tag{7.4}$$

$$\frac{d\Omega_j}{dt} = +\frac{1}{n_j a_j^2 i_j} \frac{\partial \mathcal{R}_j^{\text{sec}}}{\partial i_j}. \tag{7.5}$$

Here the subscript j denotes each individual planet. Note that the evolution equations of (e_j, ϖ_j) and (i_j, Ω_j), are completely decoupled, and hence can be analyzed separately. We neglect the inclination and node pair since these elements are not currently observable for most extrasolar planets discovered by the radial velocity technique. Be-

cause the two sets of equations take the same form, however, our eccentricity results below can be easily applied to inclination equations with the transformation $i \leftrightarrow e$ and $\Omega \leftrightarrow \varpi$.

The eccentricity components of the first-order secular disturbing functions for the two orbits are given by Murray and Dermott (1999):

$$\mathcal{R}_1^{\text{sec}} = n_1 a_1^2 \, \sigma q \left[\frac{1}{2} e_1^2 - \beta \, e_1 e_2 \cos(\varpi_1 - \varpi_2) \right], \tag{7.6}$$

$$\mathcal{R}_2^{\text{sec}} = n_2 a_2^2 \, \sigma \sqrt{\alpha} \left[\frac{1}{2} e_2^2 - \beta \, e_1 e_2 \cos(\varpi_1 - \varpi_2) \right], \tag{7.7}$$

where the subscript "1" refers to the inner planet and "2" to the outer one. Orbital mean motions are denoted by n_1 and n_2, respectively, which are both constant since the a_j are constant. For compactness of notation, we define:

$$\alpha = a_1/a_2, \quad \beta = b_{3/2}^{(2)}/b_{3/2}^{(1)},$$

$$q = m_2/m_1, \quad \sigma = \frac{1}{4} n_1 \frac{m_1}{m_*} \alpha^2 b_{3/2}^{(1)}.$$

Here the dimensionless quantities α, q, and β are the semi-major axis ratio, the mass ratio, and the ratio between two Laplace coefficients defined in Murray and Dermott (1999, §6.6). The quantity σ has units of frequency, which we will see later characterizes the secular precession rates. It is proportional to the planet-star mass ratio m_1/m_* and depends on the planetary spacing.

Following Brouwer et al. (1950), we transform an (e_j, ϖ_j) pair into a complex Poincaré canonical variable h_j with the mapping:
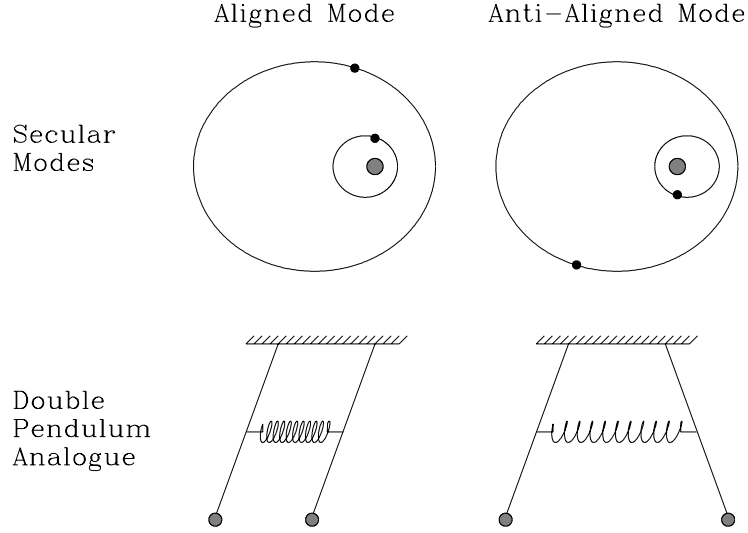
$$h_j = e_j \exp(i\varpi_j), \tag{7.8}$$

115

Figure 7.2: Analogy between the normal modes of the two-planet and the double pendulum systems.

where $i = \sqrt{-1}$. Use of the complex Poincaré variable simplifies notation compared to the more commonly used pair: $h = e \sin \varpi$, $k = e \cos \varpi$. Substituting Eqs. (7.6-7.7) into Eqs. (7.2) and (7.3) and rewriting in terms of h_j yields a set of linear homogeneous ordinary differential equations similar to those for a double pendulum system:

$$\dot{h}_j = i \sum_{k=1}^{2} A_{jk} h_k, \tag{7.9}$$

where the coefficient matrix is

$$A = \sigma \left\{ \begin{array}{cc} q & -q\beta \\ -\sqrt{\alpha}\beta & \sqrt{\alpha} \end{array} \right\}.$$

Two orthogonal special solutions (or secular eigen-modes) of the system Eq. (7.9), are given by

$$\left(\begin{array}{c} \hat{h}_{1\pm} \\ \hat{h}_{2\pm} \end{array} \right) = \left(\begin{array}{c} 1 \\ \eta_{\pm}^{s} \end{array} \right) \exp(i g_{\pm}^{s} t), \tag{7.10}$$

where the eigen-frequencies $g_{\pm}^{s}$ and eigenvector parameters $\eta_{\pm}^{s}$ are obtained from the

116

matrix A:

$$g_{\pm}^s = \frac{1}{2}\sigma\left[q + \sqrt{\alpha} \mp \sqrt{(q - \sqrt{\alpha})^2 + 4q\sqrt{\alpha}\beta^2}\right], \qquad (7.11)$$

$$\eta_{\pm}^s = \frac{q - \sqrt{\alpha} \pm \sqrt{(q - \sqrt{\alpha})^2 + 4q\sqrt{\alpha}\beta^2}}{2q\beta}. \qquad (7.12)$$

We use the superscript "s" to indicate that these parameters are for a "static", or non-dissipative, system. Note that $(g_{+}^s + g_{-}^s) = \sigma(q + \sqrt{\alpha})$ is the trace of matrix A.

We seek to elucidate the physical meaning of the two modes by transforming the solution of h_j back to the orbital elements (e, ϖ) with Eq. (7.8). If the system is fully in either the "+" or the "−" mode, we find

$$\dot{\varpi}_{1\pm} = \dot{\varpi}_{2\pm} = g_{\pm}^s, \qquad (7.13)$$

$$(e_2/e_1)_{\pm} = |\eta_{\pm}^s|, \qquad (7.14)$$

$$\cos(\Delta\varpi_{\pm}) = \eta_{\pm}^s/|\eta_{\pm}^s|, \qquad (7.15)$$

where $\Delta\varpi = \varpi_2 - \varpi_1$ is the difference between the two pericenter angles. In either mode, the two orbits precess at the same rate $g_{\pm}$ (Eq. 7.13), and their eccentricities keep a fixed ratio (Eq. 7.14). Furthermore, Eq. (7.12) shows that $\eta_{+}^s > 0$ while $\eta_{-}^s < 0$. Thus, Eq. (7.15) states that the pericenters of the two orbits are always aligned in the "+" mode ($\cos(\Delta\varpi) = 1$), and always anti-aligned in the "−" mode ($\cos(\Delta\varpi) = -1$). In fact, in an eigenmode, the system behaves as a rigid body with the shapes and relative orientation of the elliptical orbits remaining fixed while the entire structure rotates in space (Fig. 7.2). The 2-planet secular system is in many ways reminiscent of a double pendulum system. The equations for a simple double pendulum system have the same form as Eq. (7.9), only with a symmetric coefficient matrix A. In both

117

systems, the anti-aligned mode has the faster frequency ($g_- > g_+$) due to a larger restoring force provided by the spring in the pendulum problem, and the more closely spaced orbits in the planetary problem.
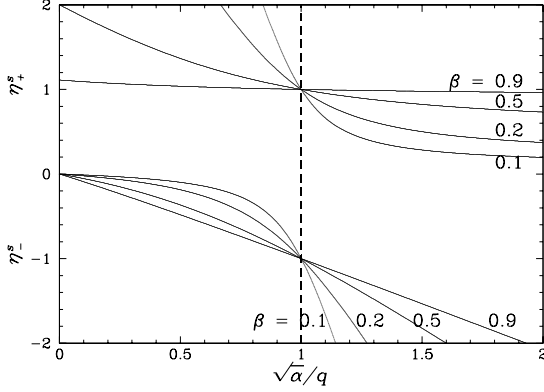

Figure 7.3: Eccentricity ratios versus $\sqrt{\alpha}/q$ in the secular modes as given by Eq. (7.12). Different curves represent different β values. The dashed line representing $q = \sqrt{\alpha}$ is a turning point; these orbits have $e_1 = e_2$ in both modes.

We now explore how the eccentricity ratios in secular modes depend on the physical parameters q and α. We plot $\eta_\pm^2$ as a function of $\sqrt{\alpha}/q$ for different β values in Fig. 7.3. Although rare in real systems, $q = \sqrt{\alpha}$ makes an interesting special case. When this condition is met, $\eta_\pm^s = \pm 1$ (Eq. 7.12), and therefore, the inner and outer orbits have the same eccentricity (Eq. 7.14). When $q > \sqrt{\alpha}$, either the outer planet is more massive (larger q), or the two planets are further apart (smaller α). Then the outer planet has a higher eccentricity in the aligned mode and a lower eccentricity in the anti-aligned mode. The opposite is true for $q < \sqrt{\alpha}$.

Only very special initial conditions will put a system exactly in one of its eigenmodes. In general, most systems are composed of a linear combination of the two modes:

$$h_j = e_+ \exp(i\varphi_+)\,\hat{h}_{j+} + e_- \exp(i\varphi_-)\,\hat{h}_{j-}. \tag{7.16}$$

Here the mode amplitudes $e_\pm$ and phases $\varphi_\pm$ are determined by the initial conditions.

Plotting the solution Eq. (7.16) on the complex plane yields a phase portrait
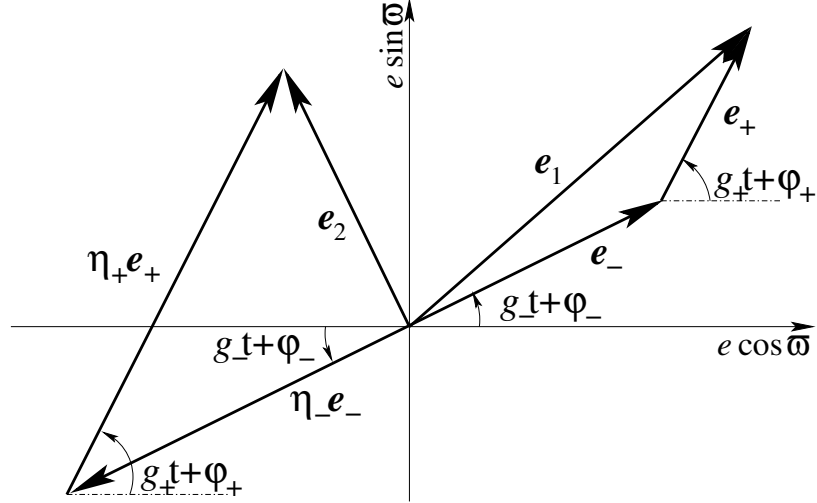
Figure 7.4: Phase plot of the secular solution of a system with two planets (Eq. 7.16). The arrows represent the eccentricity vector $e \exp(i\omega)$. The total eccentricity of each orbit (e_1 or e_2) is the vector sum of an aligned ($+$) and an anti-aligned ($-$) component. The two aligned mode components, $\mathbf{e}_+$ and $\eta_+^s \mathbf{e}_+$, rotate (precess) at rate g_+^s, while the two anti-aligned mode components ($\mathbf{e}_-$ and $\eta_-^s \mathbf{e}_-$) rotate at rate g_-^s. The maximum of e_1 occurs when e_2 is at minimum, and vice versa.

of $e \cos \varpi$ versus $e \sin \varpi$ as shown in Fig. 7.4. The $\mathbf{e}_1$ and $\mathbf{e}_2$ vectors in the plot

represent (e, ϖ) pairs for the two orbits at a given time. The length of a vector is the

instantaneous eccentricity, and its azimuthal angle is the instantaneous longitude of

pericenter. Each eccentricity vector is a vector sum of an aligned and an anti-aligned

component ($\mathbf{e}_1 = \mathbf{e}_+ + \mathbf{e}_-$, $\mathbf{e}_2 = \eta_+^s \mathbf{e}_+ + \eta_-^s \mathbf{e}_-$). In the pure aligned eigenmode, $e_- = 0$,

the $\mathbf{e}_1$ and $\mathbf{e}_2$ vectors are parallel, and as time progresses, the vectors rotate together

at rate g_+^s while maintaining their lengths. This corresponds to the aligned orbits in

Fig. 7.2. For the anti-aligned eigenmode, $e_+ = 0$ so that $\mathbf{e}_1$ and $\mathbf{e}_2$ are anti-parallel

and rotate together at rate g_-^s. This is the anti-aligned mode in Fig. 7.2. In the most

general system, both motions occur simultaneously: the parallel eccentricity vectors

($\mathbf{e}_+$ and $\eta_+^s \mathbf{e}_+$) rotate at rate g_+^s, while the anti-parallel vectors ($\mathbf{e}_-$ and $\eta_-^s \mathbf{e}_-$) spin
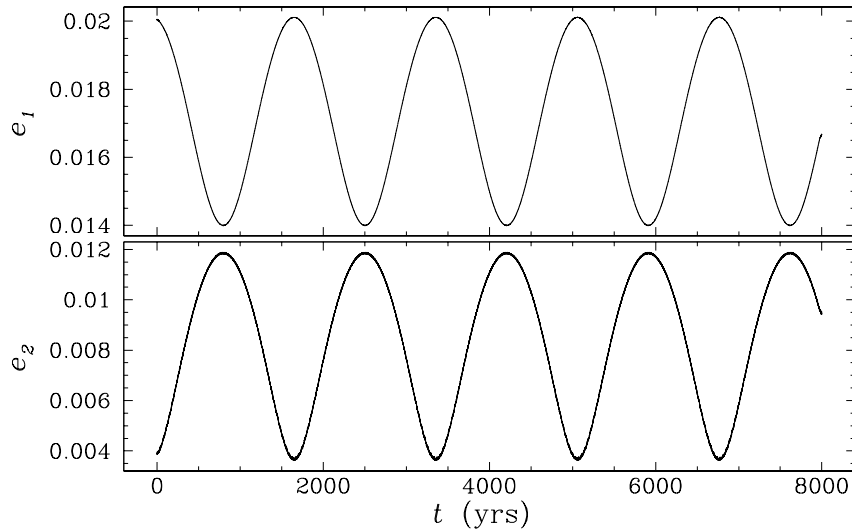
Figure 7.5: Secular changes of orbital eccentricities. Plot shows the eccentricities of two planetary orbits in a computer-simulated system consisting of a 1 Solar-mass star, a 1 Jupiter-mass "hot-Jupiter" at 0.05 AU, and a 0.8 Jupiter-mass companion at 0.2 AU. The simulation shows an oscillation period of ~ 1690 years, closely agreeing with the prediction of the secular model:f $2\pi/(g_- - g_+) = 1670$ years. This simulation was carried out with the *HNBody* package by Rauch and Hamilton (2002).

at rate g_-^s. The resulting lengths of $\mathbf{e}_1$ and $\mathbf{e}_2$ thus vary periodically as illustrated in Fig. 7.5. The maximum value of e_1 occurs when $\mathbf{e}_+$ is parallel to $\mathbf{e}_-$. At the same time, however, $\eta_+^s \mathbf{e}_+$ and $\eta_-^s \mathbf{e}_-$ are anti-parallel to each other, leading to a minimum value for e_2. The simultaneous maximum for e_1 and minimum for e_2 are guaranteed by angular momentum conservation. The two eccentricities, in mathematical form, are (Murray and Dermott, 1999)

$$e_1 = \sqrt{e_+^2 + e_-^2 + 2e_+e_- \cos(g_-^s - g_+^s)t},$$

$$e_2 = \sqrt{(e_+\eta_+^s)^2 + (e_-\eta_-^s)^2 + 2e_+e_-\eta_+^s\eta_-^s \cos(g_-^s - g_+^s)t}.$$

Both eccentricities oscillate at the difference frequency $(g_-^s - g_+^s)$.

Chapter 8

Secular Solutions with Eccentricity Damping

Since a planet close to its host star experiences a drag force due to planetary tides raised by the star, we seek a way to include tides into the mathematical formalism of Chapter 7. Because the force is radial (Section 2.5), there is no torque and the planet's angular momentum is conserved: $a(1 - e^2) = \text{const.}$ For small eccentricities for which the secular solution Eq. (7.16) is valid, this implies that changes in a are negligible compared to the damping in e. Because the damping timescales for "hot-Jupiters" ($\sim 10^8$ yrs) are much slower than secular timescales ($\sim 10^3$ yrs), we can treat the damping effect as a small perturbation to the secular solution.

8.1   Secular Modes with Eccentricity Damping

The addition of the constant tidal damping (Eq. 7.1) adds an extra term to the eccentricity equation in Eq. (7.3), which now reads

$$\dot{e}_j = -\frac{1}{n_j a_j^2 e_j} \frac{\partial \mathcal{R}_j}{\partial \varpi_j} - \lambda_j e_j.$$

This causes the coefficient matrix of Eq. (7.9) to change to

$$A = \sigma \left\{ \begin{matrix} q + i\,\xi_1 & -q\beta \\ -\sqrt{\alpha}\beta & \sqrt{\alpha} + i\,\xi_2 \end{matrix} \right\}, \tag{8.1}$$

where the dimensionless $\xi_j = \lambda_j / \sigma \ll 1$.

Eccentricity damping causes the eigen-frequencies of matrix A to have both real and imaginary parts. As in other dynamical systems, the real parts ($g_\pm$) of the eigen-frequencies still represent the precession rates of the secular modes, while the imaginary parts ($\gamma_\pm$) indicate that the amplitudes of the modes change over time. This is clearer if we rewrite the two orthogonal special solutions of the system as

$$\begin{pmatrix} \hat{h}_{1\pm} \\ \hat{h}_{2\pm} \end{pmatrix} = \begin{pmatrix} 1 \\ \eta_\pm \end{pmatrix} \exp(-\gamma_\pm t) \, \exp(i g_\pm t), \tag{8.2}$$

where $\eta_\pm$ is the new eccentricity ratio for each mode.

For $\xi_j \ll 1$, we solve the new matrix for the complex frequencies and find

$$g_\pm = g_\pm^s \pm \frac{q\sqrt{\alpha}\beta^2}{[(q-\sqrt{\alpha})^2 + 4\,q\sqrt{\alpha}\beta^2]^{3/2}} \, \sigma\,(\xi_1 - \xi_2)^2, \tag{8.3}$$

$$\gamma_\pm = \frac{1}{2}\left[\lambda_1 + \lambda_2 \pm \frac{\sqrt{\alpha} - q}{\sqrt{(q-\sqrt{\alpha})^2 + 4\,q\sqrt{\alpha}\beta^2}}(\lambda_1 - \lambda_2)\right], \tag{8.4}$$

with $g_\pm^s$ given by Eq. (7.11). Eccentricity damping increases the precession rate of the aligned mode and decreases that of the anti-aligned mode, but only by a small amount of order ξ_j^2, which can usually be neglected. These tiny frequency changes are due to the slightly different orbital configurations in the secular modes as we shall see below. The new eigen-vectors of the matrix A are:

$$\eta_\pm = \eta_\pm^s \left[1 \pm i \frac{\xi_1 - \xi_2}{\sqrt{(q-\sqrt{\alpha})^2 + 4\,q\sqrt{\alpha}\beta^2}}\right]. \tag{8.5}$$

Here we have neglected terms of the second- and higher-order power of ξ_j.

In general, the $\eta_\pm$ are complex, with small imaginary components. If we ignore the imaginary parts for the moment, then $\eta_\pm$ are real and Eq. (8.2) shows that the pericenter angles of the two orbits are the same (positive η_+, aligned mode) or $180°$

apart (negative η_-, anti-aligned mode). For complex $\eta_\pm$, however, the two orbits are not exactly aligned or anti-aligned any longer (Fig. 8.1). Instead, $\Delta\varpi_\pm$ shifts from $0°$ and $180°$ by a small angle

$$\epsilon = \tan^{-1}\left(\frac{\xi_1 - \xi_2}{\sqrt{(q - \sqrt{\alpha})^2 + 4\,q\sqrt{\alpha}\beta^2}}\right) \approx \frac{\xi_1 - \xi_2}{\sqrt{(q - \sqrt{\alpha})^2 + 4\,q\sqrt{\alpha}\beta^2}}.$$
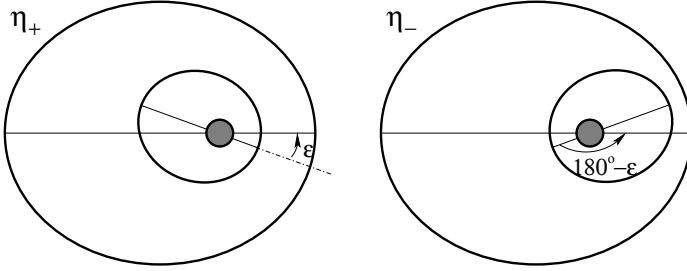

Figure 8.1: Mis-aligned orbital configurations for secular modes with eccentricity damping. In each mode, both orbits precess counter-clockwise at the same rate and keep their orientation fixed.

In the "aligned" mode, the new pericenter difference is $\Delta\varpi_+ = \epsilon$. Because of this mis-alignment, the minimum distance between the two orbits is slightly less than that in the undamped case. This causes the average interaction between the two orbits to be stronger, leading to an increase of the precession frequency as indicated by Eq. (8.3). Similarly, $\Delta\varpi_- = 180° - \epsilon$ in the "anti-aligned" mode; the slight rotation results in a weaker average interaction and a slightly slower mode-precession rate. The deviation angle ϵ is tiny, and the eccentricity ratios in the two modes, $|\eta_\pm|$, are nearly the same as $|\eta_\pm^s|$. Thus, we continue to use "aligned" and "anti-aligned" to refer to the two modes.

In addition to the little mis-alignment, each mode amplitude also damps at the rate given by Eq. (8.4). If only planetary tides contribute to eccentricity damping, Eq. (7.1) shows that the damping rate decreases rapidly with the planet's semi-major axis ($\lambda \propto a^{-6.5}$). In the absence of secular interaction between the planets, the outer orbit is hardly affected. With this interaction, however, the damping applied to the
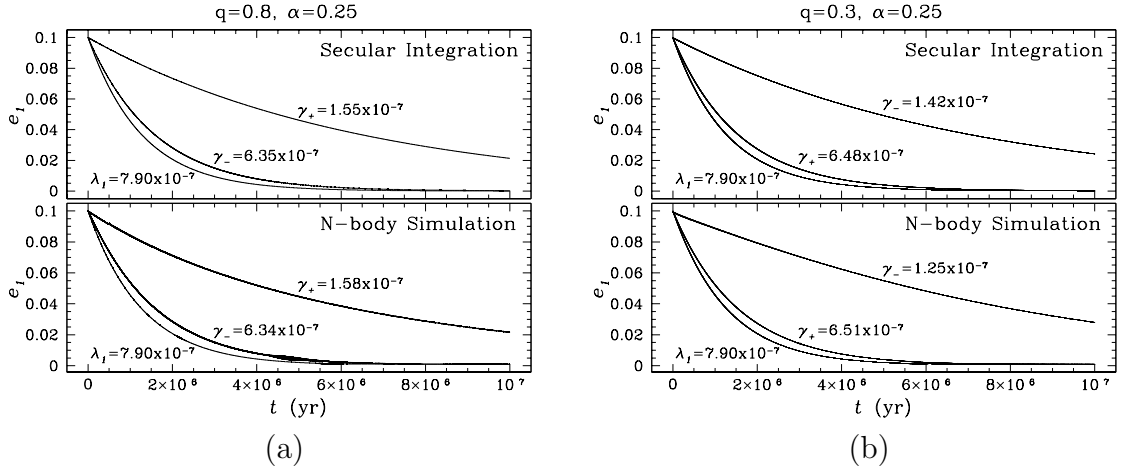
123

Figure 8.2: Eccentricity damping of systems in different secular modes found by integration of the secular equations (top panels) and direct N-body simulations (bottom panels). The plots show the eccentricity evolution of a "hot-Jupiter" (1 Jupiter-mass planet at 0.05 AU from a 1 Solar-mass star) with a companion; γ_+ and γ_- represent the mode damping rates. The "hot-Jupiter" is subject to an artificial eccentricity damping having a rate $\lambda_1 = 7.9 \times 10^{-7}\, yr^{-1}$, which is also plotted in each panel. a) A 0.8 Jupiter-mass companion is located at 0.2 AU ($q > \sqrt{\alpha}$); b) A 0.3 Jupiter-mass companion is located at 0.2 AU ($q < \sqrt{\alpha}$).

eccentricity of the inner orbit is partially transmitted to the outer planet, causing a decrease of its eccentricity as well. The damping rates of the two modes are different, unless $q = \sqrt{\alpha}$, or $m_1^2 a_1 = m_2^2 a_2$. An interesting result from Eq. (8.4) is that the sum of the two mode-damping rates is equal to the sum of the two individual eccentricity damping rates:

$$\gamma_+ + \gamma_- = \lambda_+ + \lambda_-;$$

secular interactions simply redistribute where the damping occurs.

In Fig. 8.2, we compare our analytical results with numerical integration of both the secular equations and the direct N-body equations, with an artificial eccentricity damping added for the inner planet in all cases. The eccentricity evolution curves of the inner planet are plotted for two different cases, and e-folding rates are mea-

124

sured and marked for all curves. Fig. 8.2a illustrates a system with $q > \sqrt{\alpha}$, or $m_1^2 a_1 < m_2^2 a_2$. The top panel shows results from secular equations, and the bottom panel shows the corresponding N-body simulations. Each panel plots three curves: i) the single planet case, in which the eccentricity of the inner planet damps at rate λ_1, ii) a two-planet aligned mode with damping rate γ_+, and iii) a two-planet anti-aligned mode (damping rate γ_-). For $q > \sqrt{\alpha}$, eccentricities damp much faster in the anti-aligned mode than in the aligned mode, as predicted by Eq. (8.4). A comparison between the top and bottom panel shows close agreement (within 2%) between full-scale N-body simulation and integration of the approximate secular equations. Damping rates predicted by Eq. (8.4) also agree well with these observed values. Fig. 8.2b shows a system with $m_1^2 a_1 > m_2^2 a_2$, for which the aligned mode damps faster than the anti-aligned mode. The faster damping rate of the aligned mode in the N-body simulation is still within 2% of the prediction, but that of the slow anti-aligned mode, however, is $\sim 10\%$ off. This is probably due to the fact that the drag force that we used in the N-body simulations damps the inner body's semi-major axis slightly, weakening the coupling between the planets a little.

The different damping rates for the two modes are particularly interesting, especially for well-separated nearly-decoupled orbits for which α and β are small. In this case, the $4q\sqrt{\alpha}\beta^2$ term under the square root of Eq. (8.4) is much smaller than the other term. As a result, if the eccentricity damping on one orbit is much faster than on the other, as the case for tides ($\lambda_1 \ll \lambda_2$), one mode damps much faster than the other and the system quickly evolves to a single mode. The more rapid damping rate

is near the single-planet tidal rate λ_1, while the other mode decays substantially more slowly.

We now carry out secular integrations and N-body simulations for the same two-planet system ($q > \sqrt{\alpha}$) shown in Fig. 8.2a, but with initial conditions that lead to a superposition of the two eigen-modes at the beginning. The results are depicted in Fig. 8.3. The two numerical methods agree with each other very well, except for some blurring of the orbital elements in the N-body simulations arising from fast variations at the orbital periods. These oscillations are partially due to impulses at conjunction, and partially due to the subtle difference between the osculating and geometrical orbital elements as discussed by Greenberg (1981). Before about 4×10^6 years, the system is in a combination of the two modes, so both eccentricities, as well as their ratio, oscillate (cf. Figs. 7.4 and 7.5). As the short-lived anti-aligned mode damps away, the orbits begin to librate around $\Delta\varpi = 0°$, the two eccentricities oscillate less and less, and in the end, the eccentricity ratio settles at the aligned mode ratio $|\eta_+|$ predicted by Eq. (8.5). Fig. 8.3 shows the corresponding plots for $q < \sqrt{\alpha}$. The orbital elements undergo similar evolution, except that the aligned mode damps faster and the system ends up in the anti-aligned mode.

8.2   Apsidal Circulation and Libration

In both Figs. 8.3 and 8.4, the orientations of the two orbits change from libration ($\Delta\varpi$ librates about 0° or 180°) to circulation ($\Delta\varpi$ circulates a full 360°), and to libration again during the eccentricity damping. In order to understand what determines the
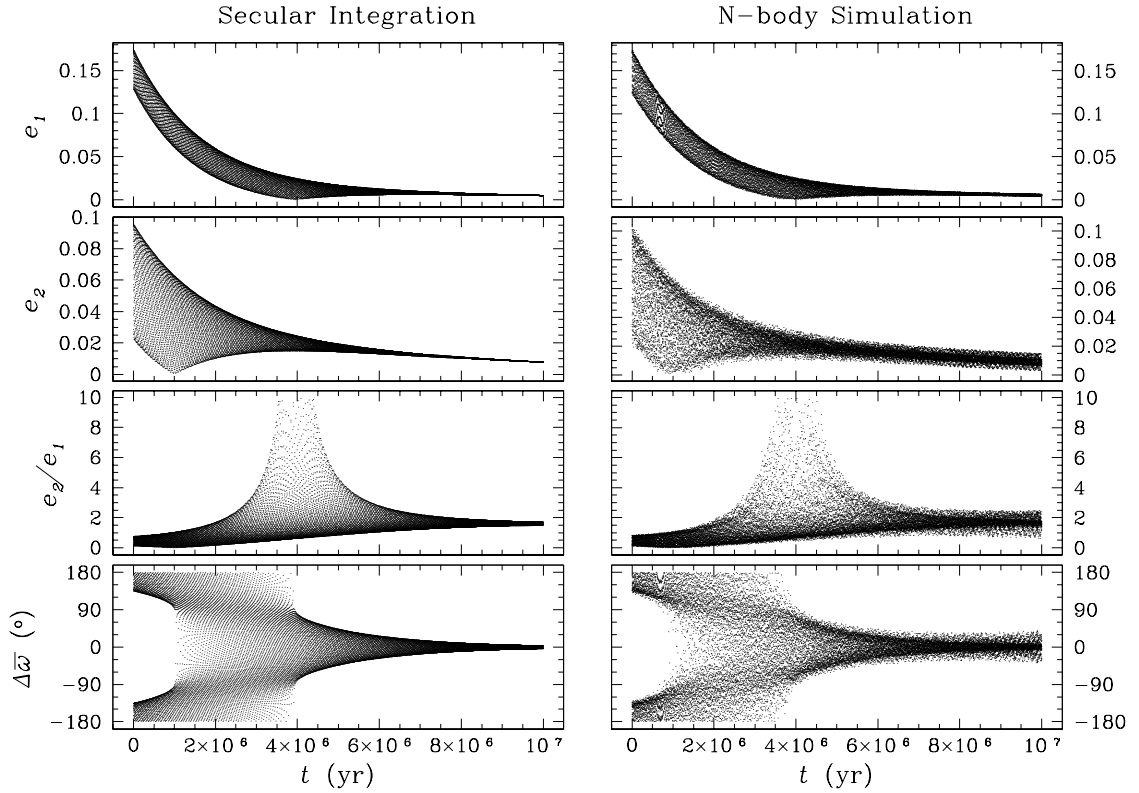
Figure 8.3: Secular evolution for systems with $m_1^2 a_1 < m_2^2 a_2$. The same planetary system as in Fig. 8.2a is shown, but with a different initial condition so that the system starts in a combination of the two modes. The anti-aligned mode damps quickly at rate γ_- from Fig. 8.2a, and the system evolves to the aligned mode. Secular integration results are shown in the left panels, while the N-body results are in the right panels. Agreement between the two integration methods is very good.
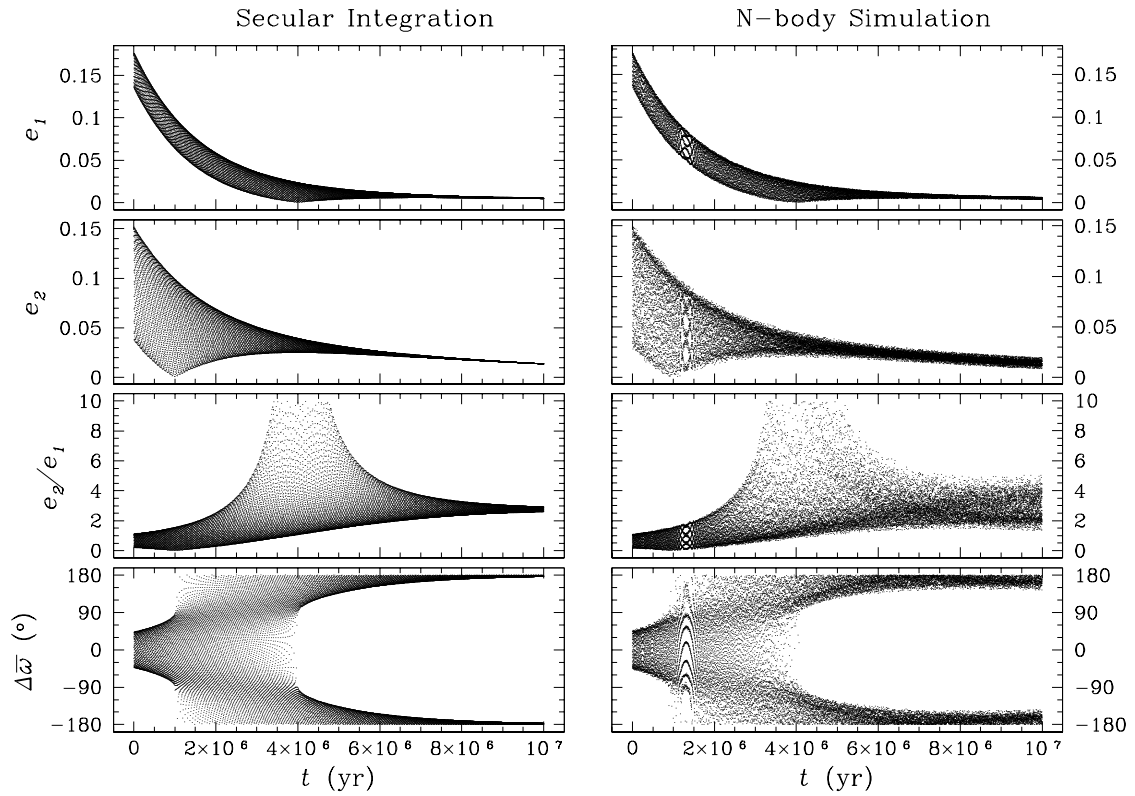
Figure 8.4: Secular evolution for systems with $m_1^2 a_1 > m_2^2 a_2$. Similar to Fig. 8.3, but the planetary system in Fig. 8.2b is shown. The aligned mode damps more rapidly and the system evolves to the anti-aligned mode.

128

apsidal state of the orbits, we plot the aligned and anti-aligned components of the eccentricities for Fig. 8.3 in the top two panels of Fig. 8.5. Recall that the total eccentricities of the orbits at any time can be obtained from the components as illustrated in Fig. 7.4. The lower panels in the figure show the phase diagrams of both orbits ($e\cos(\Delta\varpi)$ versus $e\sin(\Delta\varpi)$) at five different points in time indicated in the top two panels. The two orbits travel along the phase curves, which themselves change slowly over time. Two critical instants, labeled s_- and s_+, are circulation-libration separatrices, which represent the transitions of the apsidal state from anti-aligned libration to circulation (s_-), and from circulation to aligned libration (s_+). These two points divide the evolution curves into three regions.

In region I ($t < 10^6$ yrs), the anti-aligned components are stronger than the aligned ones for both orbits ($e_- > e_+$ and $|\eta_-^s|e_- > \eta_+^s e_+$). In the phase plots, both the e_1 and the e_2 curves are closed and stay on the left side of the $e\sin(\Delta\varpi)$ axis, indicating the libration of $\Delta\varpi$ about $180°$. With the decrease in the amplitudes of all components, especially the faster damping of the anti-aligned ones, the curves move closer toward the origin, resulting in an increased libration width of $\Delta\varpi$.

The anti-aligned separatrix s_- crossing occurs at $t = 10^6$ yrs, when the two components for the outer orbit are equal ($|\eta_-^s|e_- = \eta_+^s e_+$) and e_2 may drop to zero, resulting in a phase curve for the orbit that is tangential to the $e\sin(\Delta\varpi)$ axis at the origin (cf. Fig. 8.5). The phase curve for e_1 at s_- is a half-oval whose straight edge includes the origin. Accordingly, when e_2 drops to zero, $\Delta\varpi$ jumps from $90°$ to $-90°$ for the largest possible full libration amplitude of $180°$.
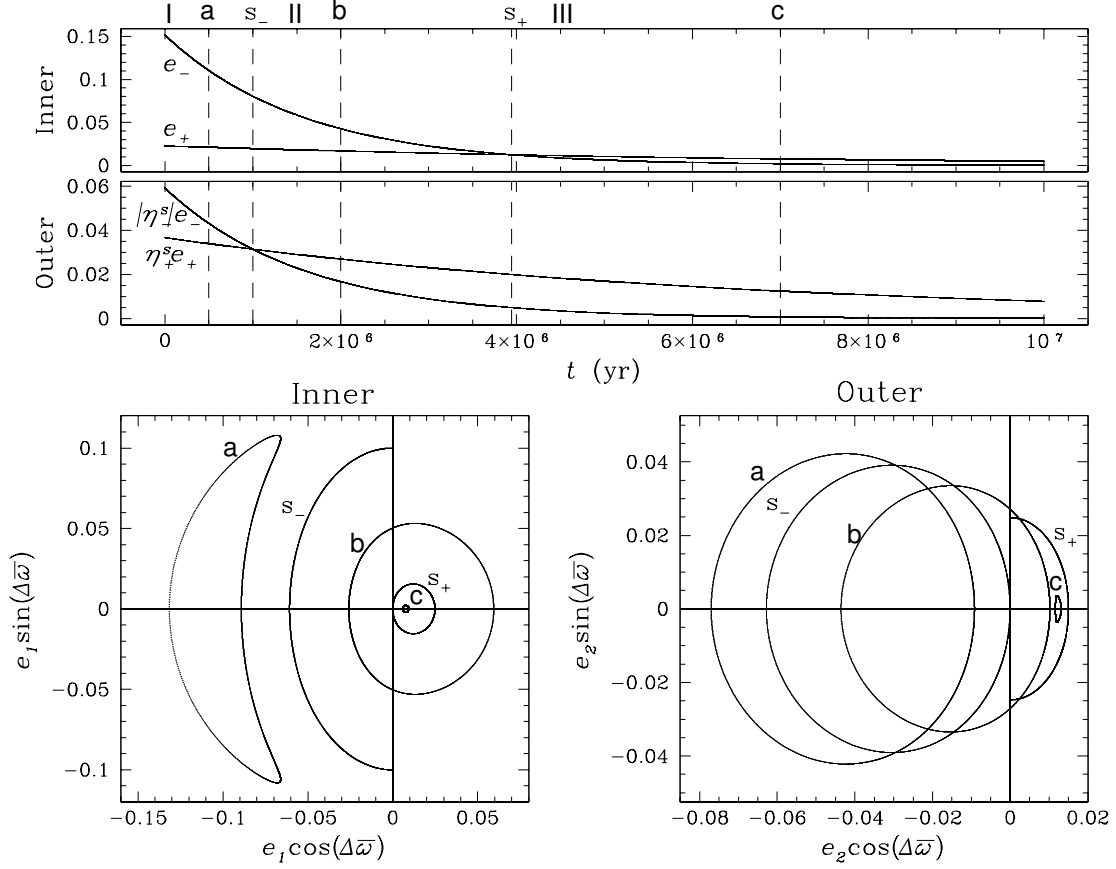
Figure 8.5: Evolution of the apsidal states during eccentricity damping. The top two panels show the time evolution of the eccentricity components for the system in Fig. 8.3 for which $m_1^2 a_1 < m_2^2 a_2$. The inner orbit has an aligned component e_+ and an anti-aligned one e_-, while $\eta_+^s e_+$ and $|\eta_-^s| e_-$ are the components for the outer orbit. Two circulation-libration separatrices (s_- and s_+) divide the evolution curves into three parts: anti-aligned libration (region I), circulation (region II), and aligned libration (region III). The bottom panels show phase diagrams of the inner and outer orbits on the complex $e \exp(i\Delta\varpi)$ plane at the corresponding points indicated in the top panels. The shape of the phase curves depends on the relative strength of the two components for each orbit. Banana shapes result from the large difference between the two components: $e_- \ll e_+$ at (a), while $|\eta_-^s| e_- \ll \eta_+^s e_+$ at (c).

130

As the system moves past s_-, the phase curves for both orbits enclose the origin and circulation results. The circulation region (II) is located between the two separatrices (i.e., when 10^6 yrs $< t < 3.95 \times 10^6$ yrs), where the anti-aligned component of the inner orbit is stronger than the aligned one ($e_- > e_+$), while it is weaker for the outer orbit ($|\eta_-^s|e_- < \eta_+^s e_+$). With the continuous fast damping of the anti-aligned mode, the system crosses the aligned separatrix s_+ at $t = 3.95 \times 10^6$ yrs, when the two components for the inner orbit are equal ($e_- = e_+$). The two separatrices occur at those times when each phase curve in Fig. 8.5 touches the origin.

After s_+, both phase curves are to the right of the $e \sin(\Delta\varpi)$ axis, indicating libration about the aligned mode (region III). The two anti-aligned components are both significantly damped and the system now has both $e_- > e_+$ and $|\eta_-^s|e_- > \eta_+^s e_+$.

The geometry of the orbits can also be illustrated with a component diagram similar to Fig. 7.4, but in a frame rotating at the same rate as the anti-aligned mode (Fig. 8.6). Note that in this rotating frame, the aligned component vectors rotate clockwise because their precessions are slower than those of the anti-aligned ones. Evolution in these coordinates can be visualized as circles whose radii and distances to the origin shrink at the different rates γ_+ and γ_-. Since the anti-aligned components initially dominate the aligned ones (region I), the $\mathbf{e}_1$ vector stays on the right side of the $e \sin \varpi$ axis, and the $\mathbf{e}_2$ vector on the left side. When the aligned components are parallel to the vertical axis, the angle between $\mathbf{e}_1$ and $\mathbf{e}_2$, $|\Delta\varpi| > 90°$, is at minimum; thus the orbits librate about $\Delta\varpi = 180°$ (anti-aligned libration). When the $\mathbf{e}_2$ circle moves to enclose the origin and the $\mathbf{e}_1$ circle is still confined in the first and fourth
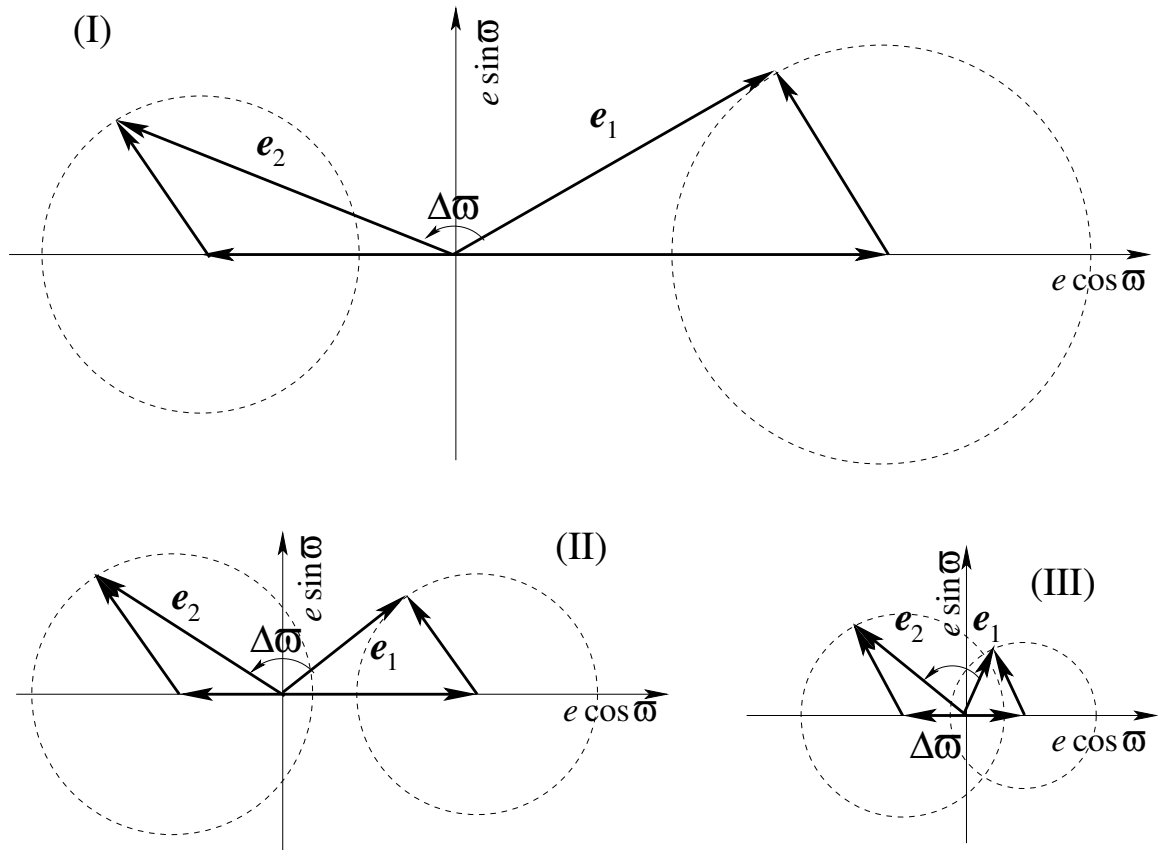
131

Figure 8.6: Eccentricity component diagrams for different regions in Fig. 8.5. These diagrams are similar to Fig. 7.4, but now shown in a frame rotating at the same rate as the anti-aligned mode. Here the anti-aligned mode damps faster than the aligned mode ($\gamma_- > \gamma_+$) so that the circles move toward the origin faster than their radii shrink.

quadrants, the system reaches circulation region II. This geometry enables $\Delta\varpi$ to cycle through a full $360°$ (Fig. 8.6). Finally, when the anti-aligned components are sufficiently damped and both circles contain the origin, the system goes to aligned mode libration (region III). Now the maximum value of $\Delta\varpi < 90°$ occurs when the two aligned components are parallel to the $e\sin\varpi$ axis, and the orbits librate about $\Delta\varpi = 0°$.

Fig. 8.7 shows the case of Fig. 8.4, where the two aligned components are initially stronger and the system starts in the aligned libration region III. The two orbits evolve to cross the aligned separatrix s_+ into the circulation region II, and then pass the anti-aligned separatrix s_- to reach the final anti-aligned libration region I. The equivalent of Fig. 8.6 for this system would show the radii of the circles shrinking faster than the distances of their center from the origin.

In conclusion, the apsidal state of a two-planet secular system depends on the relative strengths of the mode components in the following way:

$$\text{Libration: } (e_+ - e_-)(\eta_+^s e_+ + \eta_-^s e_-) > 0; \tag{8.6}$$

$$\text{Circulation:} (e_+ - e_-)(\eta_+^s e_+ + \eta_-^s e_-) < 0. \tag{8.7}$$

Libration occurs when the same mode components are stronger for both orbits, and circulation occurs when one mode is stronger for the inner orbit, but weaker for the outer one. Barnes and Greenberg (2006b) studied the non-dissipative secular apsidal state and found the distinction between circulation and libration can be expressed in
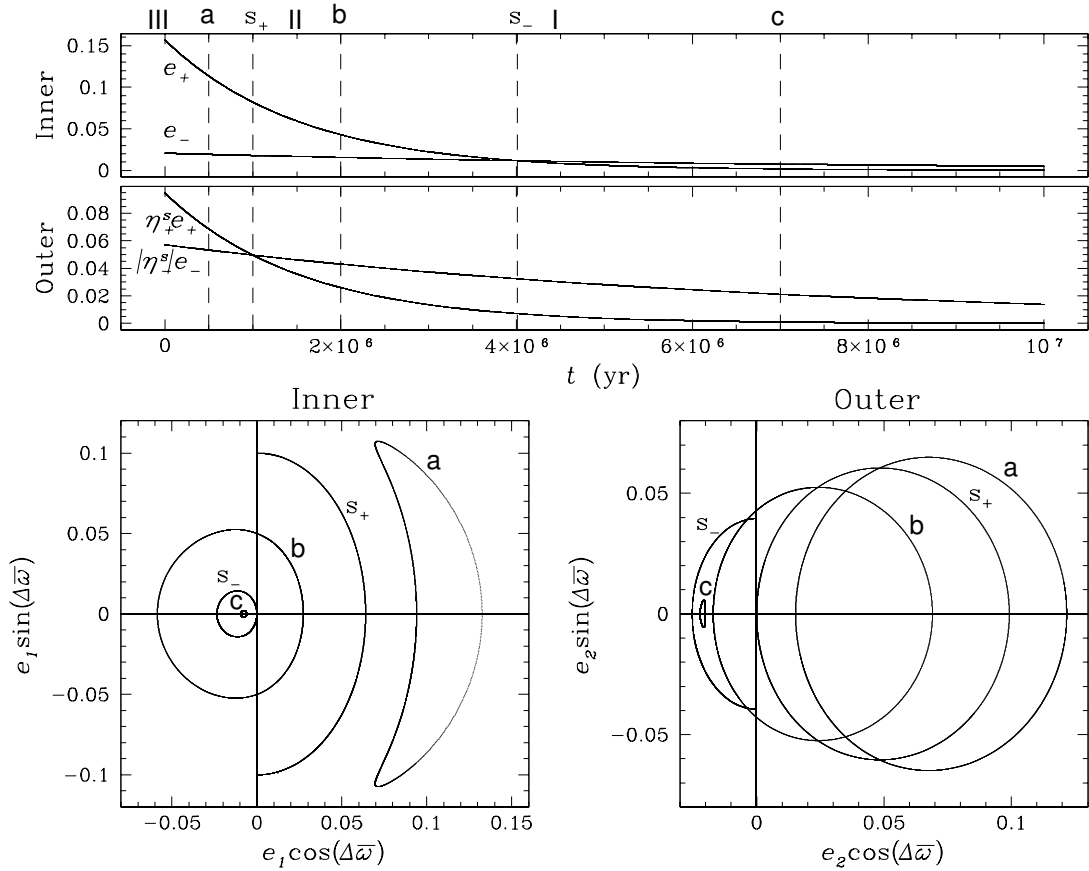
Figure 8.7: Evolution of the apsidal state during eccentricity damping. Similar to Fig. 8.5, but using data from Fig. 8.4. The system moves from aligned libration to circulation, and finally to anti-aligned libration.

134

terms of the quantity

$$S = \frac{(\eta_+^s + \eta_-^s)e_+e_-}{\eta_+^s e_+^2 + \eta_-^s e_-^2}.$$

They found that the pericenter difference $\Delta\varpi$ circulates if $|S| > 1$, and $\Delta\varpi$ librates if $|S| < 1$, which is equivalent to our conclusion.

Eccentricity damping is effective in changing the apsidal state of the orbits because the two modes damp at different rates. In fact, not only eccentricity damping, but eccentricity excitation is also able to move the two orbits across the libration-circulation separatrices. This can be easily visualized by running the plots in Fig. 8.5 and 8.7 backwards in time. For systems with $m_1^2 a_1 < m_2^2 a_2$ (Fig. 8.5), eccentricity excitation eventually brings the systems into anti-aligned libration (region I), and eccentricity damping brings them into aligned libration (region III). The opposite is true for systems with $m_1^2 a_1 > m_2^2 a_2$ (Fig. 8.7). All mechanisms that change eccentricities slowly cause planetary systems to move toward apsidal libration.

8.3   Relativistic Correction

Extrasolar "hot-Jupiters" are close enough to their host stars that general relativistic effects are important. In particular, it is well-known that the post-Newtonian potential produces an apsidal precession of the orbit which, to the lowest order in eccentricities, is (Danby, 1988)

$$\dot{\varpi}^{GR} = \frac{3\,a^2 n^3}{c^2},$$

where c is the speed of light. We define a dimensionless quantity κ to measure the relativistic effect:

$$\kappa = \frac{\dot{\varpi}_1^{GR}}{\sigma},$$

which is the ratio of the relativistic precession to the characteristic secular precession.

General relativity adds an extra term to Eq. (7.3), which now reads

$$\dot{\varpi}_j = +\frac{1}{n_j a_j^2 e_j}\frac{\partial \mathcal{R}_j}{\partial e_j} + \dot{\varpi}_j^{GR}.$$

Since $\dot{\varpi}^{GR}$ is independent of e for small eccentricities, the extra terms do not change the form of Eq. (7.9), and so all discussion of the general secular modes still holds. In particular, the system still has aligned and anti-aligned modes and the two modes damp separately. The mode frequencies, damping rates, and eccentricity ratios, however, need to be revised. Now the diagonal terms of the coefficient matrix A_{jk} should be adjusted to

$$A = \sigma \left\{ \begin{array}{cc} q + \kappa + i\xi_1 & -q\beta \\ -\sqrt{\alpha}\beta & \sqrt{\alpha}(1 + \alpha^2\kappa) + i\xi_2 \end{array} \right\},$$

which gives the new mode frequencies and eccentricity ratios:

$$g_\pm^s = \frac{1}{2}\sigma\left\{(q+\kappa) + \sqrt{\alpha}(1+\alpha^2\kappa) \mp \sqrt{[q+\kappa-\sqrt{\alpha}(1+\alpha^2\kappa)]^2 + 4\,q\sqrt{\alpha}\beta^2}\right\} \tag{8.8}$$

$$\eta_\pm^s = \frac{q+\kappa-\sqrt{\alpha}(1+\alpha^2\kappa) \pm \sqrt{[q+\kappa-\sqrt{\alpha}(1+\alpha^2\kappa)]^2 + 4\,q\sqrt{\alpha}\beta^2}}{2\,q\beta}, \tag{8.9}$$

$$g_\pm = g_\pm^s \pm \frac{q\sqrt{\alpha}\beta^2}{\{[q+\kappa-\sqrt{\alpha}(1+\alpha^2\kappa)]^2 + 4q\sqrt{\alpha}\beta^2\}^{3/2}}\,\sigma\,(\xi_1-\xi_2)^2, \tag{8.10}$$

$$\gamma_\pm = \frac{1}{2}\left[\lambda_1 + \lambda_2 \pm \frac{\sqrt{\alpha}(1+\alpha^2\kappa) - (q+\kappa)}{\sqrt{[q+\kappa-\sqrt{\alpha}(1+\alpha^2\kappa)]^2 + 4q\sqrt{\alpha}\beta^2}}(\lambda_1 - \lambda_2)\right], \tag{8.11}$$

$$\eta_\pm = \eta_\pm^s\left\{1 \pm i\frac{\xi_1 - \xi_2}{\sqrt{[q+\kappa-\sqrt{\alpha}(1+\alpha^2\kappa)]^2 + 4\,q\sqrt{\alpha}\beta^2}}\right\}. \tag{8.12}$$

Note that these equations can be obtained from Eqs. (7.11, 7.12, 8.3, 8.4, and 8.5) with the substitution $(q \pm \sqrt{\alpha}) \rightarrow [q + \kappa \pm \sqrt{\alpha}(1 + \alpha^2 \kappa)]$.

The relativistic effect increases both secular rates $g_\pm^s$ (Eq. 8.8) since it causes the orbits to precess in the same direction as the secular interaction does. Both mode eccentricity ratios are also increased (Eq. 8.9), because the eccentricity of a faster precessing inner orbit is less forced by the outer planet. As for the mode damping rates (Eq. 8.11), relativistic precession decreases the aligned mode damping rate, but increases that of the anti-aligned mode. It also decreases the deviation ϵ of the mode apsidal lines from perfect alignment (Eq. 8.12).

Chapter 9

Applications to Extrasolar Planetary Systems

The purpose of the Wu and Goldreich (2002) study of secular theory and tidal damping was to explain the eccentricity of the planet HD 83443b. At the time there was thought to be a second planet in the system, a claim that has since been retracted. In addition to tidal eccentricity damping, they also considered the small change to the semi-major axis that arises from energy dissipation. They found that, even in a single apsidal aligned or anti-aligned mode, the eccentricities of the two orbits damp at different rates – e_1 damps faster because of the semi-major axis migration. For small eccentricities, however, the inward migration, is slower than the eccentricity damping by a factor of e_1^2. Thus we have neglected the semi-major axis migration, which is consistent with the low e assumption made within linear secular theory, and we have derived a simpler theory to study the apsidal state of orbits and to estimate eccentricities. Our expression for the mode damping rates, Eq. (8.9), are consistent with that of Wu and Goldreich (2002). In this chapter, we first use the theory developed in Chapter 8 to analyze the current status of a two-planet system, and then discuss how our equations can be used to predict possible companions of "hot-Jupiters".

Table 9.1: Properties of planets and stars discussed in this chapter

Planet	Orbital Period (days)	$m \sin i$ (M_J)	a (AU)	e	ω (°)	m_* ($M_\odot$)	Age (Gyrs)
HIP 14810b	6.674 ± 0.002	3.9 ± 0.6	0.069 ± 0.004	0.147 ± 0.006	159 ± 2	~ 0.99	~ 4
HIP 14810c	95.285 ± 0.002	0.8 ± 0.1	0.41 ± 0.02	0.409 ± 0.006	354 ± 2	~ 0.99	~ 4
GJ 436b	2.64385 ± 0.00009	0.0713 ± 0.006	0.029 ± 0.002	0.16 ± 0.02	351 ± 1	0.44 ± 0.04	> 3
GJ 674b	4.6938 ± 0.007	0.037	0.039	0.20 ± 0.02	143 ± 6	0.35	$0.1\text{-}1$

Data for HIP 14810 system are from Wright et al. (2007); GJ 436 from Maness et al. (2007); GJ 674 from Bonfils et al. (2007).

9.1 A Test of the Theory: the HIP 14810 System

Several multi-planet systems that host one or more "hot-Jupiters" have been discovered, but most are not good candidates upon which to test our theory. The Gliese 876, 55 Cnc, and υ And systems all have three or more planets, which makes apsidal analysis more complicated (Barnes and Greenberg, 2006a). The HD 217107 system has two planets, but the outer planet is 60 times further away from the star than the inner one, resulting in weak secular interactions that are insufficient to force any interesting eccentricity on the inner orbit. The recent discovery of a two-planet system HIP 14810 (Wright et al., 2007), however, provides a good test for our theory. Star HIP 14810a is a Solar-type star with a mass of 0.99 Solar mass. The orbital parameters of the two planets are listed in Table 9.1: the 3.9 Jupiter-mass inner planet (HIP 14810b) has an orbital period of 6.674 days, and its orbital eccentricity is as large as 0.147; the outer HIP 14810c is about 20% as massive, and about 6 times further away. It has a larger eccentricity of 0.4.

At 0.147 and 0.4, the eccentricities of the two orbits are larger than that assumed by our linear secular theory. But this brings merely a $\sim$20% error as shown in Fig. 9.1. Here we depict the orbital histories of the two planets on a phase diagram, similar to the ones shown in Figs. 8.5 and 8.7. We plot curves computed both from secular theory (red) and from N-body simulation (black) and find reasonable agreement. It appears as if the system librates about $\Delta\varpi = 180°$, but is near the anti-aligned separatrix so that the libration amplitude is large. This is an example of a general observation that extrasolar multi-planet systems tend to be near a secular separatrix

140
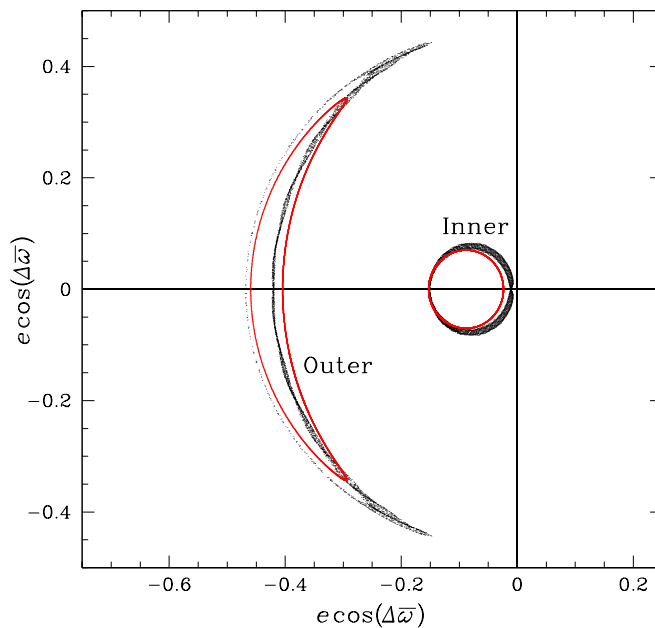
Figure 9.1: The current apsidal state of the HIP 14810 system. We show the orbits of both planets on the $e \exp(i\Delta\varpi)$ plane, similar to the lower plots in Fig. 8.5 and 8.7. The red curves represent the solution of secular equations, while black curves are obtained through an N-body simulation. The orbits librate about $\Delta\varpi = 180°$, with the libration width $\sim 100°$ predicted by the secular theory, and $\sim 140°$ measured from N-body simulation.

(Barnes and Greenberg, 2006b). The near-separatrix state of the system is surprising; perhaps it is due to insufficient tidal circularization. HIP 14810b is about 0.07 AU from its star, which is relatively far compared to other "hot-Jupiters" so that tidal dissipation may simply too weak to significantly alter the apsidal state.

How does the current state of the system compare with the expectation from tidal-damping theory as developed in Chapter 8? In Section 8.2, we found that if tides are strong enough, every system will rapidly damp to either apsidally aligned or anti-aligned. Which mode the system finally ends up in depends on the damping rates given by Eqs. (8.4) and (8.11). In a secular eigen-mode, the outer and inner

141

orbits have a predictable eccentricity ratio (Eqs. 8.5 and 8.12). In Fig. 9.2, we show

a contour plot of the eccentricity ratio between the two orbits for the more slowly

damped eigen-mode in the parameter space (q, α), assuming a fixed inner planet b

and varying the parameters q and α of planet c. The dashed line divides the space into

a slow aligned mode region (top left) and a slow anti-aligned region (bottom right). In

the blue area, the lifetime of the aligned mode is longer than the age of the systems; in

the red region, the anti-aligned mode can last the age of the system; and in the white

middle area, both modes should have already damped away. Hence, we expect to find

that the two orbits are apsidally aligned or in aligned libration in the blue area, and

they are anti-aligned or in anti-aligned libration in the red region. The boundaries of

these areas depend only on the age of the system and the tidal damping timescale.

We have assumed an age of 4 billion years and a tidal circularization timescale at 500

million years. An older system age and/or faster damping rate will expand the white

area and further constrain the outer planet. The actual location of planet c in the

HIP 14810 system is marked in both plots of Fig. 9.2. It resides in the more slowly

damped anti-aligned mode region, as expected from Fig. 9.1.

A comparison between the two plots in Fig. 9.2 shows the effect of relativistic

pericenter precession. The anti-aligned area (red) diminishes while the aligned area

(blue) expands into the region of low-mass distant companions (small q, small α,

the bottom left corner in the plots), systems in which the relativistic precession rate

competes with the planet-induced ones ($\sigma \sim \dot{\varpi}^{GR}$). The shrinking of the red area

agrees with Eq. (8.11) which shows that relativistic precession tends to increase the

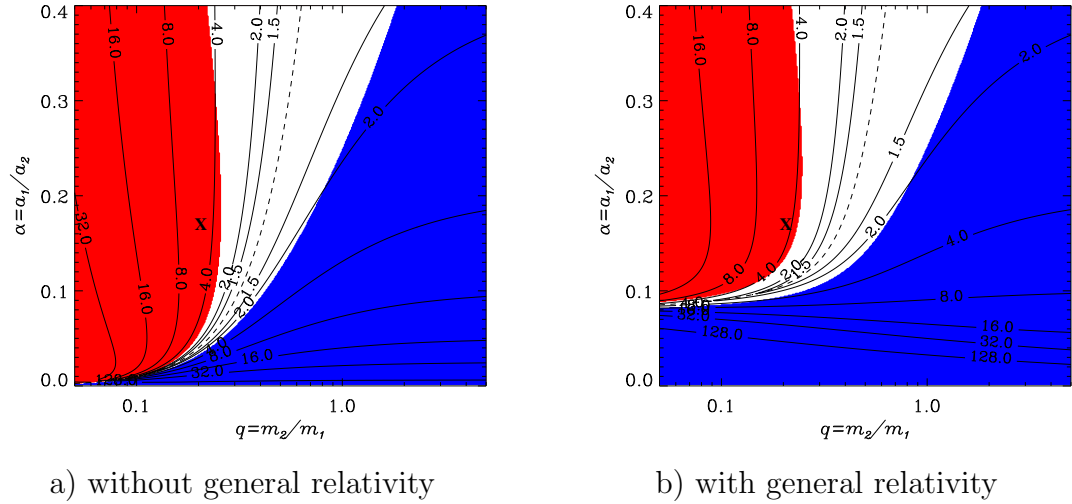a) without general relativity b) with general relativity

Figure 9.2: Orbital states of possible companions for HIP 14810b without (a) and with (b) general relativistic precession. We have assumed the tidal-damping timescale to be 500 million years. Each point in these q - α plots represents an outer companion with corresponding mass and semi-major axis. The dashed curve divides the plane into regions in which the aligned mode damps faster (top-left) and the anti-aligned mode damps faster (bottom-right). Furthermore, in the colored regions, either the aligned mode (blue) or the anti-aligned mode (red) can survive tidal dissipation and last longer than the age of the system (4 Gyrs). The solid contour lines represent the eccentricity ratio η^s of the long-lived (slower) mode. The location of HIP 14810c is marked by the black cross.

damping rate of the anti-aligned mode and to decrease that of the aligned mode.

9.2 Constraints on Possible Companions of "Hot-Jupiters"

If tidal dissipation is strong enough, an extrasolar two-planet system should have evolved into either an aligned or an anti-aligned apsidal-lock state. Equations (8.9) and (8.11) thus provide a constraint on these three parameters: the mass ratio q of the two planets, the semi-major axis ratio α, and eccentricity ratio of the two orbits. For a lonely "hot-Jupiter" with confirmed parameters and non-zero eccentricity, we can predict possible companion that may force its orbital eccentricity. We illustrate

our method with a few examples.

Figure 9.3a is similar to Fig. 9.2, but now for the planetary system around the M dwarf star GJ 436; here we plot contours of the companion's eccentricity rather than the eccentricity ratios. With only 1.3 Neptune masses, GJ 436b is the first Neptune-sized extrasolar planet detected through a radial velocity survey (Butler et al., 2004). It has recently been found to transit its host star (Gillon et al., 2007), which removes the uncertainty in the determination of its mass. The planet is $0.023\,AU$ away from the star (orbital period ~ 2.6 days), and has an orbital eccentricity of about 0.16. If this eccentricity is due to another planet and the system has damped to an eigen-mode, then Fig. 9.3a excludes almost the entire anti-aligned region and all companions that are less that 1/10 as massive as GJ 436b, or more than 5 times further away – these planets are simply too weak to force the inner planet's eccentricity. In fact, if we consider the age of the system, which is estimated to be older than 3 billion years (Gillon et al., 2007) and probably much older, most possible outer companions are much more massive than GJ 436b. Larger planets in this region are very likely within the radial-velocity detection window, but none have been found. Most planets outside this region, however, cannot be observationally excluded. Recall that the boundaries between the long-lived mode zones and the short-lives one (dotted lines in Fig. 9.3a) depend on both the tidal timescale and how long the eccentricities have been damped. We have assumed that tides have acted to circularize the orbits throughout the evolution history of the system. It is possible that a later event, such as a resonance crossing, excites the eccentricities and tides have worked for a much
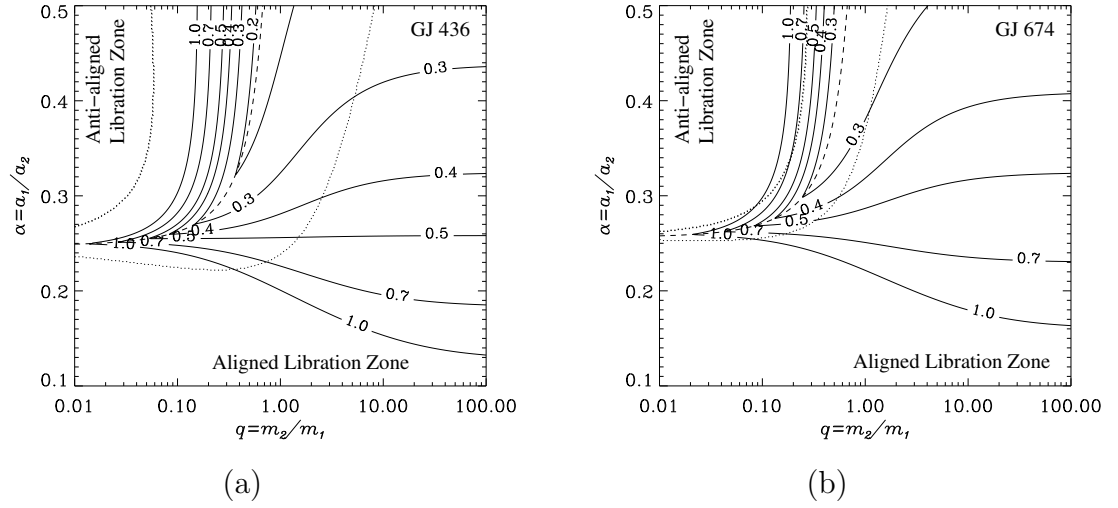
144

Figure 9.3: Eccentricities of possible companions for the "hot-Neptunes" a) GJ 436b, and b) GJ 674b. These plots are similar to Fig. 9.2b, except that contours show the eccentricity of the outer orbit, and dotted lines replace boundaries between the colored areas; between the dotted lines, both modes should damp away within the 3 Gyr age of the system.

shorter time. This pushes the two dotted lines toward the boundary between the faster aligned zone and faster anti-aligned zone (dashed line in Fig. 9.3a), and makes more parameters available to the outer planet. Furthermore, the secular theory is accurate only for small eccentricities. For very eccentric orbits, e.g., $e > 0.4$, further analysis is necessary to include higher-order terms in the disturbing functions.

Another recently discovered "hot-Neptune", GJ 674b in shown in Fig. 9.3b. This system is very similar to the GJ 436 system, except that the star is much younger. With an age of only about half a billion years, most of the parameter space in the $q-\alpha$ plane is available for a possible secular companion. The slightly larger eccentricity of GJ 674b, however, pushes the eccentricity contours towards the upper-right in Fig. 9.3b, which means that all possible companions with small masses or large semi-major axes are excluded.

The assumption of an apsidal lock that we made at the beginning of this section, however, is probably too strong. What we have seen for the HIP 14810 system may be true for most systems: although one mode has been significantly damped, its amplitude is not yet near zero. In this case, for a "hot-Jupiter" with known mass, semi-major axis, and eccentricity, the eccentricity of the companion is still free to vary somewhat even for a given mass and semi-major axis. We have shown that the existence of a companion certainly slows the tidal circularization of "hot-Jupiters" and can maintain non-zero orbital eccentricities.

Part IV

Conclusion

Chapter 10

Conclusion and Future Directions

Modern computing technology has made it possible to study the orbital motion of the planets over their 4.5 billion year histories, and we are rapidly approaching the point where this will also be possible for satellite systems. Numerical simulation also proves to be an effective tool to test analytical theories. In this dissertation, we have combined numerical methods with mathematical techniques to address several problems in both resonant and secular orbital dynamics. In the last chapter of this dissertation, we summarize our results, tie up some loose ends, and indicate some promising future directions.

10.1   The Inner Neptunian System

In Chapters 3 - 6, we have shown that the dynamics of the small inner Neptunian satellites are strongly affected by Neptune's large moon, Triton. We derived mathematical tools (Chapter 4) to analyze resonances in this system, and we numerically studied the details of resonance passages between Proteus and other satellites. Triton's huge mass and large orbital tilt lead to strong three-body resonant kicks in the traditional two-body resonant zones between a pair of small satellites (Chapter 5). We showed that these resonant kicks can explain the existing non-zero orbital tilts of

three of the four largest inner moons. If the satellites have a common mean density between 0.4 and 0.8 g/cm^3, the inclinations of Proteus, Galatea, and Despina can be excited by three or four Proteus resonance passages. The tilt of Larissa, however, is twice as large as can be explained with these resonant events alone. In Chapter 6, we suggested that a resonant capture event might have tilted Larissa's orbit, and that this event might also be responsible for the large inclination of Naiad (Table 3.1).

10.1.1   The 4.7° Inclination of Naiad

The origin of Naiad's large tilt was first investigated by Banfield and Murray (1992), who undertook a resonant-history analysis for the inner Neptunian satellites similar to our study in Section 3.2. Since the importance of three-body resonances was not known at the time, the authors suggested that Naiad might have been trapped into one of the standard two-body resonances with another satellite. Because two-body resonances are so weak (cf. Fig. 5.2), the probability of resonant capture is low, typically only a few percent. The number of possible resonance passages, however, is large and the total capture probability could reach $\sim 76\%$ with multiple resonance passages invoked (Banfield and Murray, 1992).

With our discovery of the strong three-body resonances with Triton, resonance trapping is much more probable. Our numerical observations show that the capture probability for a zero-degree-inclined Naiad approaches one hundred percent. In other words, Naiad would likely be trapped into the first three-body resonance it passes across, as shown in Fig. 10.1. This figure shows that Naiad and Galatea are
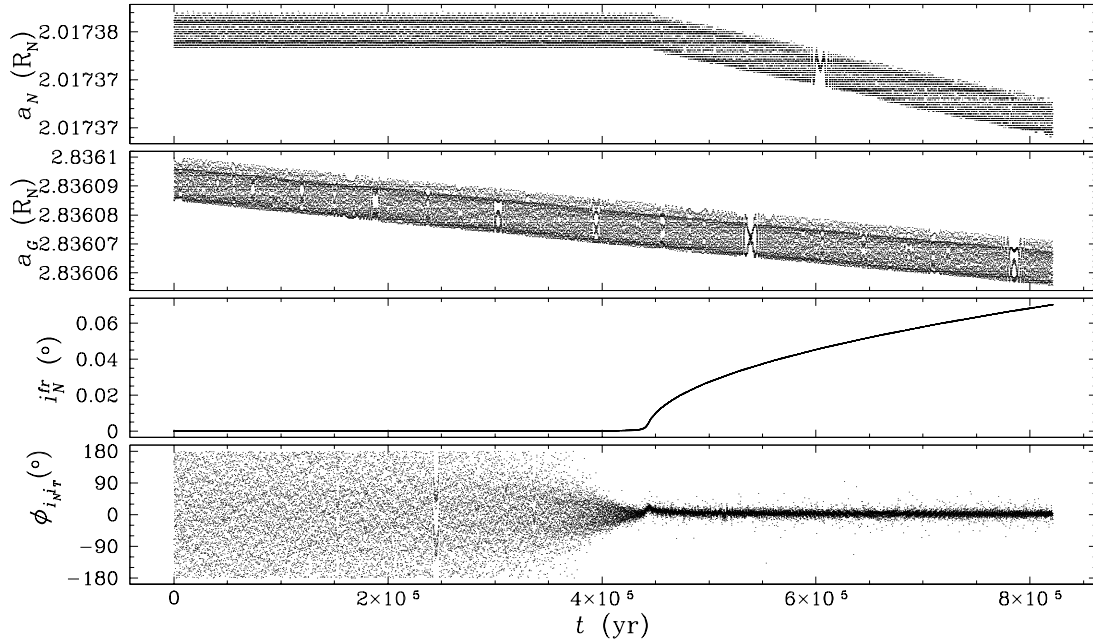
Figure 10.1: A numerical simulation in which Naiad and Galatea are trapped into their 5:3 mean-motion resonance with Triton. The corresponding resonant angle $\phi_{i_N i_T} = 5\lambda_G - 3\lambda_N - \tilde{\Omega}_N - \Omega_T$ is shown in the bottom panel.

trapped into a 5:3 inclination resonance with Triton when Galatea migrates inward and the two orbits converge. During the resonant trapping, the free inclination of Naiad grows in time, and its semi-major axis decreases with Galatea's to keep the satellites in resonance.

In order to explain Naiad's current tilt, the satellites must exit the resonance when $i_N^{fr} \sim 4.7°$. Multiple excitations are unlikely because the capture probability decreases dramatically once the satellite's inclination is above a critical value (Borderies and Goldreich, 1984). Several mechanisms can break the resonance lock, including additional mean-motion resonances, secondary resonances (resonances between the libration frequencies of nearby mean-motion resonances, Malhotra, 1990),

150

and possible non-resonant perturbations from other satellites. A systematic study is necessary to understand which resonance, with which satellite, might have been responsible for the capture, and to determine how resonance evolves after capture. Besides providing an explanation for the large inclinations of Larissa and Naiad, a successful theory would also further constrain tidal models.

10.1.2 Confinement of Neptunian Ring Arcs

The puzzles in the inner Neptunian system arose even before the discovery of the six small satellites. After the first evidence for the existence of Larissa (Reitsema et al., 1982), several observations of stellar occultations (e.g. Hubbard et al., 1986) implied possible narrow ring arcs around Neptune, which were later confirmed during the *Voyager 2* fly-by (Smith et al., 1989). Goldreich et al. (1986) suggested that the sharp edge of the rings could be confined by a Lindblad resonance ($\phi = (p+1)\lambda_2 - p\lambda_1 - \varpi_1$) with a hypothetical satellite, and further proposed that the ring arcs were azimuthally confined by an inclination co-rotation resonance ($\phi = (p+2)\lambda_2 - p\lambda_1 - 2\Omega_1$). This shepherd satellite turns out to be Galatea, whose 43:42 resonance multiplet sits near the ring arcs (Porco, 1991). More recent observations (Sicardy et al., 1999; Dumas et al., 1999), however, showed that the rings are not centered on the inclination co-orbital resonance. This led Namouni and Porco (2002) to seek a new explanation in which the non-zero mass of the ring arcs moves the location of the resonances. These authors invoked an eccentricity co-rotation resonance to confine the ring arcs and estimated that the total mass of the ring arcs is $0.002 - 0.2$ times the mass of

Galatea, which is large for such a narrow ring system.

The requirement for a massive ring might be relaxed if Triton's effect were to be considered. Although none of the strong Triton resonances are located especially close to the ring arcs, and the standard two-body resonances are not shifted significantly, the system is complicated and warrants a more careful investigation.

10.2 Perturbed Secular Interactions

Additional perturbations that affect planetary orbits, such as mass accretion and radial migration, may interfere with secular interactions. In Chapter 7 - 9, we examined the case of slow eccentricity decay due to tidal drag. Because of secular interactions, eccentricity damping imposed on one orbit can be transmitted to the other, and the timescale for total damping can be substantially slowed. The current eccentricities of "hot-Jupiters" might be secularly forced by unknown companions. Here we expand our attention to consider the effects of additional perturbations on the system.

10.2.1 Effects of Adiabatic Changes in a and m

Although tidal circularization is important for "hot-Jupiters", additional perturbations on orbits may be important in other situations. Here we consider both planet migration and mass loss or accretion. For the simplest case in which the mass of the outer planet is much less than that of the inner planet, or $q \ll \sqrt{\alpha}$, Eqs. (7.11) and (7.12) can be simplified to:

$$g_+^s = 0, g_-^s = \sigma\sqrt{\alpha}; \ \eta_+^s = \beta, \eta_-^s = -\infty;$$

and the general solution of the two orbits are (Eq. 7.16)

$$h_1 = e_+,$$

$$h_2 = \beta \, e_+ + e_- \exp[i(\sigma\sqrt{\alpha}t + \varphi_-)].$$

Thus, the inner orbit is not affected, and the eccentricity of the outer orbit consists of a "forced" component $e^{forced} = \beta \, e_+$ and a "free" component $e^{fr} = e_-$, similar to the discussion in Chapter 4 where Triton forces the inclinations of small Neptunian satellites. Note that for a small free eccentricity, these are aligned orbits. Similar arguments for a system with an inner planet of negligible mass ($q \ll \sqrt{\alpha}$) also lead to a near aligned configuration:

$$h_1 = e_+ + e_- \exp[i(\sigma q t + \varphi_-)],$$

$$h_2 = \frac{1}{\beta} \, e_+.$$

For slow adiabatic changes of any of a_1, a_2, m_1, and m_2, we find that the free eccentricity is an adiabatic invariant of the system, so it remains nearly constant over time. For more general cases where the two masses are comparable, we expect that similar adiabatic invariants exist, but to date we have been unable to prove this assertion. If these more general adiabatic invariants can be found, we would be able to determine the response of a system to a broad class of slow perturbations.

10.2.2   Systems with Three or More Planets

Approximately 10 planetary systems with 3 or more planets have been discovered to date, which motivates us to extend our approach to N planets. Since the system

in Eq. (7.9) is linear, a solution exists for any N. The solution to the characteristic equation for the eigenmodes requires solving a polynomial of order N, which is best done numerically. The identification of the eigenmodes, however, can be explored qualitatively. Recall that for a two-planet system, there are two natural apsidal co-precession states (aligned and anti-aligned as in Fig. 7.2) and they comprise the two eigenmodes. With three planets, it can be shown that all eigenmodes consist of aligned and/or anti-aligned pericenters. There are four possible states (Figure. 10.2) while the system can have only three eigenmodes. We have found that for different systems, sets of three eigenmodes are selected from the four natural states: the fully aligned and fully anti-aligned states are always eigen-modes, while the remaining one depends on mass ratios and orbital spacings. For N (> 3) planets, it is even more complicated to determine N eigen-modes from 2^{N-1} candidates, but is interesting to pursue.

The application of this study would not be limited to extrasolar planetary systems, but could also be used to further understand the dynamics of our own Solar System. One long-standing puzzle is the origin of the inclinations and ec-
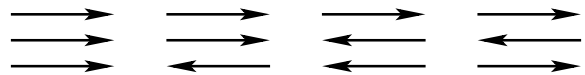
Figure 10.2: The natural apsidal co-precession states for a three-planet system. Arrows show the direction from the star to the orbital pericenters for each planet, with the inner-most planet on the top. The left-most (fully aligned) and rightmost (fully anti-aligned) sets are always eigenmodes.

centricities of the giant planets. Much attention has been paid to the large eccentricities seen in other planetary systems, leading to speculation that large eccentricities might be the norm and that our Solar System is an exception. On the other hand,

the simplest disk formation scenarios suggest that planetary orbital planes should be precisely parallel to one another (as the case of inner Neptunian satellites discussed in Part II), and planets should all orbit along perfect circles. This may indeed be the primitive state, with all non-zero eccentricities and inclinations generated by subsequent planetary interactions (Tsiganis et al., 2005) and/or interactions with the gas and planetesimal disks.

References

Adams, F. C., Laughlin, G., 2006. Effects of secular interactions in extrasolar planetary systems. *ApJ* **649**, 992–1003.

Adams, J. C., 1846. Explanation of the observed irregularities in the motion of Uranus, on the hypothesis of disturbance by a more distant planet. *MNRAS* **7**, 149–152.

Agnor, C. B., Canup, R. M., Levison, H. F., 1999. On the character and consequences of large impacts in the late stage of terrestrial planet formation. *Icarus* **142**, 219–237.

Agnor, C. B., Hamilton, D. P., 2006. Neptune's capture of its moon Triton in a binary-planet gravitational encounter. *Nature* **441**, 192–194.

Anderson, J. D., Johnson, T. V., Schubert, G., Asmar, S., Jacobson, R. A., Johnston, D., Lau, E. L., Lewis, G., Moore, W. B., Taylor, A., Thomas, P. C., Weinwurm, G., 2005. Amalthea's density is less than that of water. *Science* **308**, 1291–1293.

Aumann, H. H., 1985. IRAS observations of matter around nearby stars. *PASP* **97**, 885–891.

Banfield, D., Murray, N., 1992. A dynamical history of the inner Neptunian satellites. *Icarus* **99**, 390–401.

Barnes, R., Greenberg, R., 2006a. Behavior of apsidal orientations in planetary systems. *ApJ* **652**, L53–L56.

Barnes, R., Greenberg, R., 2006b. Extrasolar planetary systems near a secular separatrix. *ApJ* **638**, 478–487.

Beaugé, C., Ferraz-Mello, S., Michtchenko, T. A., 2003. Extrasolar planets in mean-motion resonance: Apses alignment and asymmetric stationary solutions. *ApJ* **593**, 1124–1133.

Bonfils, X., Mayor, M., Delfosse, X., Forveille, T., Gillon, M., Perrier, C., Udry, S., Bouchy, F., Lovis, C., Pepe, F., Queloz, D., Santos, N. C., Bertaux, J. ., 2007. The HARPS search for southern extra-solar planets. X. a $m \sin I = 11 M_E$ planet around the nearby spotted M dwarf GJ 674. *ArXiv e-prints*, astro–ph/0704.0270.

Boquet, F., 1889. Developpement de la fonction perturbatrice : calcul des termes DU huitie ME ordre. *Annales de l'Observatoire de Paris* **19**, B1–B75.

Borderies, N., Goldreich, P., 1984. A simple derivation of capture probabilities for the J+1:J and J+2:J orbit-orbit resonance problems. *Celestial Mechanics* **32**, 127–136.

Bottke, W. F., Jedicke, R., Morbidelli, A., Petit, J.-M., Gladman, B., 2000. Understanding the distribution of near-Earth asteroids. *Science* **288**, 2190–2194.

Bottke, W. F., Morbidelli, A., Jedicke, R., Petit, J.-M., Levison, H. F., Michel, P., Metcalfe, T. S., 2002. Debiased orbital and absolute magnitude distribution of the near-Earth objects. *Icarus* **156**, 399–433.

Brouwer, D., Clemence, G. M., 1961. *Methods of celestial mechanics*. New York: Academic Press.

Brouwer, D., van Woerkom, A., Jasper, J., 1950. *The secular variations of the orbital elements of the principal planets*. Washington, U. S. Govt. Print. Off.

Burns, J. A., 1977. Orbital evolution. In: Burns, J. A. (Ed.), *Planetary Satellites*. Univ. of Arizona Press, Tuscon, AZ, USA, pp. 113–156.

Burns, J. A., 1986. The evolution of satellite orbits. In: Burns, J. A., Matthews, M. S. (Eds.), *Satellites*. Univ. of Arizona Press, Tuscon, AZ, USA, pp. 117–158.

Burns, J. A., Showalter, M. R., Morfill, G. E., 1984. The ethereal rings of Jupiter and Saturn. In: Greenberg, R., Brahic, A. (Eds.), *Planetary Rings*. Univ. of Arizona Press, Tuscon, AZ, USA, pp. 200–272.

Burša, M., 1992. Secular Love numbers of the major planets. *Earth, Moon, and Planets* **59**, 239–244.

Butler, R. P., Marcy, G. W., Fischer, D. A., Brown, T. M., Contos, A. R., Korzennik, S. G., Nisenson, P., Noyes, R. W., 1999. Evidence for multiple companions to υ Andromedae. *ApJ* **526**, 916–927.

Butler, R. P., Vogt, S. S., Marcy, G. W., Fischer, D. A., Wright, J. T., Henry, G. W., Laughlin, G., Lissauer, J. J., 2004. A Neptune-mass planet orbiting the nearby M dwarf GJ 436. *ApJ* **617**, 580–588.

Chambers, J. E., 1999. A hybrid symplectic integrator that permits close encounters between massive bodies. *MNRAS* **304**, 793–799.

Chambers, J. E., Wetherill, G. W., 1998. Making the terrestrial planets: N-body integrations of planetary embryos in three dimensions. *Icarus* **136**, 304–327.

Chambers, J. E., Wetherill, G. W., 2001. Planets in the Asteroid Belt. *Meteoritics and Planetary Science* **36**, 381–399.

Chiang, E. I., 2003. Excitation of orbital eccentricities by repeated resonance crossings: Requirements. *ApJ* **584**, 465–471.

Cohen, C. J., Hubbard, E. C., 1965. Libration of the close approaches of Pluto to Neptune. *AJ* **70**, 10–13.

Ćuk, M., Gladman, B. J., 2005. Constraints on the orbital evolution of Triton. *ApJ* **626**, L113–L116.

Cuzzi, J. N., Lissauer, J. J., Esposito, L. W., Holberg, J. B., Marouf, E. A., Tyler, G. L., Boishchot, A., 1984. Saturn's rings - properties and processes. In: Greenberg, R., Brahic, A. (Eds.), *Planetary Rings*. Univ. of Arizona Press, Tuscon, AZ, USA, pp. 73–199.

Danby, J. M. A., 1988. *Fundamentals of Celestial Mechanics* (2nd ed.). Willmann-Bell Inc., P.O.Box 35025, Richmond, VA, USA.

Darwin, G. H., 1879. A tidal theory of the evolution of satellites. *The Observatory* **3**, 79–84.

Darwin, G. H., 1880. On the secular effects of tidal friction. *Astronomische Nachrichten* **96**, 217–222.

Dermott, S. F., Malhotra, R., Murray, C. D., 1988. Dynamics of the Uranian and Saturnian satellite systems - a chaotic route to melting Miranda? *Icarus* **76**, 295–334.

Dermott, S. F., Nicholson, P. D., 1986. Masses of the satellites of Uranus. *Nature* **319**, 115–120.

Dobrovolskis, A. R., 1993. The Laplace planes of Uranus and Pluto. *Icarus* **105**, 400–407.

Dumas, C., Terrile, R. J., Smith, B. A., Schneider, G., Becklin, E. E., 1999. Stability of Neptune's ring arcs in question. *Nature* **400**, 733–735.

Duncan, M. J., Levison, H. F., 1997. A scattered comet disk and the origin of Jupiter family comets. *Science* **276**, 1670–1672.

Duncan, M. J., Levison, H. F., Budd, S. M., 1995. The dynamical structure of the Kuiper Belt. *AJ* **110**, 3073–3081.

Duncan, M. J., Levison, H. F., Lee, M. H., 1998. A multiple time step symplectic algorithm for integrating close encounters. *AJ* **116**, 2067–2077.

Elliot, J. L., Dunham, E., Mink, D., 1977. The rings of Uranus. *Nature* **267**, 328–330.

Ellis, K. M., Murray, C. D., 2000. The disturbing function in Solar System dynamics. *Icarus* **147**, 129–144.

Esposito, L., 2006. *Planetary Rings*. Cambridge University Press, The Edinburgh Building, Cambridge CB2 2RU, UK.

Fernandez, J. A., Ip, W.-H., 1984. Some dynamical aspects of the accretion of Uranus and Neptune - the exchange of orbital angular momentum with planetesimals. *Icarus* **58**, 109–120.

Ford, E. B., Havlickova, M., Rasio, F. A., 2001. Dynamical instabilities in extrasolar planetary systems containing two giant planets. *Icarus* **150**, 303–313.

Froeschle, C., Scholl, H., 1987. Orbital evolution of asteroids near the secular resonance ν_6. *A&A* **179**, 294–303.

Galle, J. G., 1846. Account of the discovery of Le Verrier's planet Neptune, at Berlin. *MNRAS* **7**, 153–163.

Gavrilov, S. V., Zharkov, V. N., 1977. Love numbers of the giant planets. *Icarus* **32**, 443–449.

Gillon, M., Pont, F., Demory, B. ., Mallmann, F., Mayor, M., Mazeh, T., Queloz, D., Shporer, A., Udry, S., Vuissoz, C., 2007. Detection of transits of the nearby hot Neptune GJ 436 b. *ArXiv e-prints*, astro–ph/0705.2219.

Goldreich, P., Murray, N., Longaretti, P. Y., Banfield, D., 1989. Neptune's story. *Science* **245**, 500–504.

Goldreich, P., Sari, R., 2003. Eccentricity evolution for planets in gaseous disks. *ApJ* **585**, 1024–1037.

Goldreich, P., Soter, S., 1966. Q in the Solar System. *Icarus* **5**, 375–389.

Goldreich, P., Tremaine, S., Borderies, N., 1986. Towards a theory for Neptune's arc rings. *AJ* **92**, 490–494.

Goldreich, R., 1963. On the eccentricity of satellite orbits in the solar system. *MNRAS* **126**, 257–268.

Gomes, R., Levison, H. F., Tsiganis, K., Morbidelli, A., 2005. Origin of the cataclysmic Late Heavy Bombardment period of the terrestrial planets. *Nature* **435**, 466–469.

Greaves, J. S., Holland, W. S., Wyatt, M. C., Dent, W. R. F., Robson, E. I., Coulson, I. M., Jenness, T., Moriarty-Schieven, G. H., Davis, G. R., Butner, H. M., Gear, W. K., Dominik, C., Walker, H. J., 2005. Structure in the ϵ Eridani debris disk. *ApJ* **619**, L187–L190.

Greenberg, R., 1977. Orbit-orbit resonances among natural satellites. In: Burns, J. A. (Ed.), *Planetary Satellites*. Univ. of Arizona Press, Tuscon, AZ, USA, pp. 157–168.

Greenberg, R., 1981. Apsidal precession of orbits about an oblate planet. *AJ* **86**, 912–914.

Greenberg, R. J., Counselman, C. C., Shapiro, I. I., 1972. Orbit-orbit resonance capture in the solar system. *Science* **178**, 747–749.

Hamilton, D. P., 1994. A comparison of Lorentz, planetary gravitational, and satellite gravitational resonances. *Icarus* **109**, 221–240.

Hamilton, D. P., 1996. The asymmetric time-variable rings of Mars. *Icarus* **119**, 153–172.

Hamilton, D. P., Burns, J. A., 1993. Lorentz and gravitational resonances on circumplanetary particles. *Adv. Space Res.* 13 (10), 241–248.

Hamilton, D. P., Zhang, K., Agnor, C., 2005. Constraints on Triton's orbital evolution. *AAS/Division of Dynamical Astronomy Meeting* **36**, 11.04.

Henrard, J., 1982. Capture into resonance - an extension of the use of adiabatic invariants. *Celestial Mechanics* **27**, 3–22.

Holland, W. S., Greaves, J. S., Zuckerman, B., Webb, R. A., McCarthy, C., Coulson, I. M., Walther, D. M., Dent, W. R. F., Gear, W. K., Robson, I., 1998. Submillimetre images of dusty debris around nearby stars. *Nature* **392**, 788–790.

Holman, M., Touma, J., Tremaine, S., 1997. Chaotic variations in the eccentricity of the planet orbiting 16 Cygni B. *Nature* **386**, 254–256.

Holman, M. J., Wisdom, J., 1993. Dynamical stability in the outer Solar System and the delivery of short period comets. *AJ* **105**, 1987–1999.

Hubbard, W. B., Brahic, A., Sicardy, B., Elicer, L.-R., Roques, F., Vilas, F., 1986. Occultation detection of a Neptunian ring-like arc. *Nature* **319**, 636–640.

Jacobson, R. A., Owen, W. M., 2004. The orbits of the inner Neptunian satellites from Voyager, Earth-based, and Hubble Space Telescope observations. *AJ* **128**, 1412–1417.

Jacobson, R. A., Riedel, J. E., Taylor, A. H., 1991. The orbits of Triton and Nereid from spacecraft and earthbased observations. *A&A* **247**, 565–575.

Jeffreys, H., 1961. The effect of tidal friction on eccentricity and inclination. *MNRAS* **122**, 339–343.

Juric, M., Tremaine, S., 2007. The eccentricity distribution of extrasolar planets. *ArXiv Astrophysics e-prints*, astro–ph/0703160.

Karkoschka, E., 2003. Sizes, shapes, and albedos of the inner satellites of Neptune. *Icarus* **162**, 400–407.

Kaula, W. M., 1964. Tidal dissipation by solid friction and the resulting orbital evolution. *Rev. Geophys.* **2**, 661–685.

Kuchner, M. J., Holman, M. J., 2003. The geometry of resonant signatures in debris disks with planets. *ApJ* **588**, 1110–1120.

Landau, L. D., Lifshitz, E. M., 1976. *Course of Theoretical Physics, Volume 1: Mechanics* (3rd ed.). Pergamon Press, Elmsford, NY, USA.

Le Verrier, M., 1846. Sur la rectification des orbites des comètes au moyen de l'ensemble des observations faites pendant leur apparition. *Astronomische Nachrichten* **23**, 183–188.

Le Verrier, U.-J., 1855. Recherches astronomiques: Chapitre IV. - développement de la fonction qui sert de base au calcul des perturbations des mouvements des planètes. *Annales de l'Observatoire de Paris* **1**, 258–342.

Lee, M. H., 2004. Diversity and origin of 2:1 orbital resonances in extrasolar planetary systems. *ApJ* **611**, 517–527.

Levison, H. F., Duncan, M. J., 1994. The long-term dynamical behavior of short-period comets. *Icarus* **108**, 18–36.

Levison, H. F., Duncan, M. J., 1997. From the Kuiper Belt to Jupiter-family comets: The spatial distribution of ecliptic comets. *Icarus* **127**, 13–32.

MacDonald, G. J. F., 1964. Tidal friction. *Rev. Geophys.* **2**, 467–541.

Malhotra, R., 1990. Capture probabilities for secondary resonances. *Icarus* **87**, 249–264.

Malhotra, R., 1993. The origin of Pluto's peculiar orbit. *Nature* **365**, 819–821.

Malhotra, R., 1995. The origin of Pluto's orbit: Implications for the Solar System beyond Neptune. *AJ* **110**, 420–429.

Malhotra, R., Dermott, S. F., 1990. The role of secondary resonances in the orbital history of Miranda. *Icarus* **85**, 444–480.

Maness, H. L., Marcy, G. W., Ford, E. B., Hauschildt, P. H., Shreve, A. T., Basri, G. B., Butler, R. P., Vogt, S. S., 2007. The M dwarf GJ 436 and its Neptune-mass planet. *PASP* **119**, 90–101.

Marzari, F., Scholl, H., 2000. The role of secular resonances in the history of Trojans. *Icarus* **146**, 232–239.

Mayor, M., Queloz, D., 1995. A Jupiter-mass companion to a Solar-type star. *Nature* **378**, 355–359.

McKinnon, W. B., 1984. On the origin of Triton and Pluto. *Nature* **311**, 355–358.

Michel, P., Migliorini, F., Morbidelli, A., Zappalà, V., 2000. The population of Mars-crossers: Classification and dynamical evolution. *Icarus* **145**, 332–347.

Milani, A., Carpino, M., Hahn, G., Nobili, A. M., 1989. Dynamics of planet-crossing asteroids - classes of orbital behavior. *Icarus* **78**, 212–269.

Miner, E. D., Wessen, R. R., Cuzzi, J. N., 2007. Springer and Praxis Publishing, Chichester, UK.

Morbidelli, A., 1997. Chaotic diffusion and the origin of comets from the 2/3 resonance in the Kuiper Belt. *Icarus* **127**, 1–12.

Morbidelli, A., 2002. Modern integrations of Solar System dynamics. *Annual Review of Earth and Planetary Sciences* **30**, 89–112.

Morbidelli, A., Gladman, B., 1998. Orbital and temporal distributions of meteorites originating in the Asteroid Belt. *Meteoritics and Planetary Science* **33**, 999–1016.

Morbidelli, A., Levison, H. F., Gomes, R., 2007. The dynamical structure of the Kuiper Belt and its primordial origin. *ArXiv Astrophysics e-prints*, astro–ph/0703558.

Morbidelli, A., Levison, H. F., Tsiganis, K., Gomes, R., 2005. Chaotic capture of Jupiter's Trojan asteroids in the early Solar System. *Nature* **435**, 462–465.

Murray, C. D., 1986. Structure of the 2:1 and 3:2 Jovian resonances. *Icarus* **65**, 70–82.

Murray, C. D., Dermott, S. F., 1999. *Solar System Dynamics*. Cambridge University Press, The Edinburgh Building, Cambridge CB2 2RU, UK.

Murray, C. D., Harper, D., 1993. *Expansion of the planetary disturbing function to eighth order in the individual orbital elements*. QMW Math Notes No. 15, Queen Mary and Westfield College, Mile End Road, London E1 4NS, U.K.

Murray, N., Holman, M., 1999. The origin of chaos in the outer Solar System. *Science* **283**, 1877–1881.

Nagasawa, M., Ida, S., 2000. Sweeping secular resonances in the Kuiper Belt caused by depletion of the solar nebula. *AJ* **120**, 3311–3322.

Namouni, F., 2007. Origin theories for the eccentricities of extrasolar planets. *ArXiv Astrophysics e-prints*, astro–ph/0702203.

Namouni, F., Porco, C., 2002. The confinement of Neptune's ring arcs by the moon Galatea. *Nature* **417**, 45–47.

Nesvorný, D., Ferraz-Mello, S., 1997. On the asteroidal population of the first-order Jovian resonances. *Icarus* **130**, 247–258.

Nesvorný, D., Roig, F., 2001. Mean motion resonances in the trans-Neptunian region part II: The 1:2, 3:4, and weaker resonances. *Icarus* **150**, 104–123.

Nicholson, P. D., Hamilton, D. P., Matthews, K., Yoder, C. F., 1992. New observations of Saturn's coorbital satellites. *Icarus* **100**, 464–484.

Owen, T., Danielson, G. E., Cook, A. F., Hansen, C., Hall, V. L., Duxbury, T. C., 1979. Jupiter's rings. *Nature* **281**, 442–446.

Owen, W. M., Vaughan, R. M., Synnott, S. P., 1991. Orbits of the six new satellites of Neptune. *AJ* **101**, 1511–1515.

Peale, S. J., 1976. Orbital resonances in the solar system. *ARA&A* **14**, 215–246.

Peale, S. J., 1986. Orbital resonances, unusual configurations and exotic rotation states among planetary satellites. In: Burns, J. A., Matthews, M. S. (Eds.), *Satellites*. Univ. of Arizona Press, Tuscon, AZ, USA, pp. 159–223.

Peale, S. J., Cassen, P., Reynolds, R. T., 1980. Tidal dissipation, orbital evolution, and the nature of Saturn's inner satellites. *Icarus* **43**, 65–72.

Peirce, B., 1849. Development of the perturbative function of planetary motion. *AJ* **1**, 1–8.

Petit, J.-M., Morbidelli, A., Chambers, J., 2001. The primordial excitation and clearing of the Asteroid Belt. *Icarus* **153**, 338–347.

Porco, C. C., 1991. An explanation for Neptune's ring arcs. *Science* **253**, 995–1001.

Porco, C. C., Baker, E., Barbara, J., Beurle, K., Brahic, A., Burns, J. A., Charnoz, S., Cooper, N., Dawson, D. D., Del Genio, A. D., Denk, T., Dones, L., Dyudina, U., Evans, M. W., Giese, B., Grazier, K., Helfenstein, P., Ingersoll, A. P., Jacobson, R. A., Johnson, T. V., McEwen, A., Murray, C. D., Neukum, G., Owen, W. M., Perry, J., Roatsch, T., Spitale, J., Squyres, S., Thomas, P., Tiscareno, M., Turtle, E., Vasavada, A. R., Veverka, J., Wagner, R., West, R., 2005. Cassini imaging science: Initial results on Saturn's rings and small satellites. *Science* **307**, 1226–1236.

Porco, C. C., Hamilton, D. P., 2007. Planetary rings. In: McFadden, L. A., Weissman, P. R., Johnson, T. V. (Eds.), *Encyclopedia of the Solar System* (2nd ed.). Academic Press, San Diego, US, pp. 503–518.

Rauch, K. P., Hamilton, D. P., 2002. The HNBody package for symplectic integration of nearly-Keplerian systems. *Bulletin of the American Astronomical Society* **34**, 938.

Reitsema, H. J., Hubbard, W. B., Lebofsky, L. A., Tholen, D. J., 1982. Occultation by a possible third satellite of Neptune. *Science* **215**, 289–291.

Renner, S., Sicardy, B., French, R. G., 2005. Prometheus and Pandora: masses and orbital positions during the Cassini tour. *Icarus* **174**, 230–240.

163

Roy, A. E., 2005. *Orbital Motion* (4th ed.). Institute of Physics Publishing, Dirac House, Temple Back, Bristol BS1 6BE, UK.

Scholl, H., Froeschle, C., 1990. Orbital evolution of known asteroids in the ν_5 secular resonance region. *A&A* **227**, 255–263.

Sheppard, S. S., Trujillo, C. A., 2006. A thick cloud of Neptune Trojans and their colors. *Science* **313**, 511–514.

Showalter, M. R., Burns, J. A., 1982. A numerical study of Saturn's F-ring. *Icarus* **52**, 526–544.

Sicardy, B., Roddier, F., Roddier, C., Perozzi, E., Graves, J. E., Guyon, O., Northcott, M. J., 1999. Images of Neptune's ring arcs obtained by a ground-based telescope. *Nature* **400**, 731–733.

Smith, B. A., Soderblom, L. A., Banfield, D., Barnet, C., Basilevsky, A. T., Beebe, R. F., Bollinger, K., Boyce, J. M., Brahic, A., Briggs, G. A., Brown, R. H., Chyba, C., Collins, S. A., Colvin, T., Cook, A. F., Crisp, D., Croft, S. K., Cruikshank, D., Cuzzi, J. N., Danielson, G. E., Davies, M. E., De Jong, E., Dones, L., Godfrey, D., Goguen, J., Grenier, I., Haemmerle, V. R., Hammel, H., Hansen, C. J., Helfenstein, C. P., Howell, C., Hunt, G. E., Ingersoll, A. P., Johnson, T. V., Kargel, J., Kirk, R., Kuehn, D. I., Limaye, S., Masursky, H., McEwen, A., Morrison, D., Owen, T., Owen, W., Pollack, J. B., Porco, C. C., Rages, K., Rogers, P., Rudy, D., Sagan, C., Schwartz, J., Shoemaker, E. M., Showalter, M., Sicardy, B., Simonelli, D., Spencer, J., Sromovsky, L. A., Stoker, C., Strom, R. G., Suomi, V. E., Synott, S. P., Terrile, R. J., Thomas, P., Thompson, W. R., Verbiscer, A., Veverka, J., 1989. Voyager 2 at Neptune - Imaging science results. *Science* **246**, 1422–1449.

Soter, S., 1971. The dust belts of Mars. *Cornell CRSR Report* **472**.

Stockwell, J. N., 1873. Memoir on the secular variations of the elements of the oribts of the eight principal planets. *Smithsonian Contributions to Knowledge* **18**, 1–199.

Sussman, G. J., Wisdom, J., 1988. Numerical evidence that the motion of Pluto is chaotic. *Science* **241**, 433–437.

Sussman, G. J., Wisdom, J., 1992. Chaotic evolution of the Solar System. *Science* **257**, 56–62.

Tittemore, W. C., Wisdom, J., 1988. Tidal evolution of the Uranian satellites. I - passage of Ariel and Umbriel through the 5:3 mean-motion commensurability. *Icarus* **74**, 172–230.

Tittemore, W. C., Wisdom, J., 1989. Tidal evolution of the Uranian satellites. II - an explanation of the anomalously high orbital inclination of Miranda. *Icarus* **78**, 63–89.

Tsiganis, K., Gomes, R., Morbidelli, A., Levison, H. F., 2005. Origin of the orbital architecture of the giant planets of the Solar System. *Nature* **435**, 459–461.

Ward, W. R., 1988. On disk-planet interactions and orbital eccentricities. *Icarus* **73**, 330–348.

Ward, W. R., Colombo, G., Franklin, F. A., 1976. Secular resonance, solar spin down, and the orbit of Mercury. *Icarus* **28**, 441–452.

Wilner, D. J., Holman, M. J., Kuchner, M. J., Ho, P. T. P., 2002. Structure in the dusty debris around Vega. *ApJ* **569**, L115–L119.

Wisdom, J., 1980. The resonance overlap criterion and the onset of stochastic behavior in the restricted three-body problem. *AJ* **85**, 1122–1133.

Wisdom, J., 1983. Chaotic behavior and the origin of the 3/1 Kirkwood gap. *Icarus* **56**, 51–74.

Wisdom, J., 1987. Urey Prize Lecture - Chaotic dynamics in the Solar System. *Icarus* **72**, 241–275.

Wisdom, J., Holman, M., 1991. Symplectic maps for the N-body problem. *AJ* **102**, 1528–1538.

Wolszczan, A., Frail, D. A., 1992. A planetary system around the millisecond pulsar PSR1257 + 12. *Nature* **355**, 145–147.

Wright, J. T., Marcy, G. W., Fischer, D. A., Butler, R. P., Vogt, S. S., Tinney, C. G., Jones, H. R. A., Carter, B. D., Johnson, J. A., McCarthy, C., Apps, K., 2007. Four new exoplanets and hints of additional substellar companions to exoplanet host stars. *ApJ* **657**, 533–545.

Wu, Y., Goldreich, P., 2002. Tidal evolution of the planetary system around HD 83443. *ApJ* **564**, 1024–1027.

Yoder, C. F., 1973. *On the Establishment and Evolution of Orbit-Orbit Resonances.* PhD Thesis.

Yoder, C. F., 1995. Astrometric and geodetic properties of Earth and the Solar System. In: Ahrens, T. (Ed.), *Global Earth Physics: A Handbook of Physical Constants.* American Geophysical Union, Washington, pp. 1–31.

Yoder, C. F., Peale, S. J., 1981. The tides of Io. *Icarus* **47**, 1–35.

Zakamska, N. L., Tremaine, S., 2004. Excitation and propagation of eccentricity disturbances in planetary systems. *AJ* **128**, 869–877.

Zhang, K., Hamilton, D. P., 2007. Orbital resonances in the inner Neptunian system. *Icarus* **188**, 386–399.